Wide-area geohazard risk assessment in snowy-cold regions by multiphase soil mechanics and multi-scale analysis

高緯度寒冷地域の広域地盤災害リスク評価手法に関する研究

By

Yulong ZHU

A thesis submitted in partial fulfillment of the requirements for the degree of Doctor of Philosophy in Engineering

under the guidance and supervision of

Professor Tatsuya ISHIKAWA

Examined by the Doctoral Committee

Professor Tatsuya ISHIKAWA
Professor Yoichi WATABE
Professor Yasuyuki SHIMIZU
Professor (Associate) Satoshi NISHIMURA

December 2020

English Engineering Education Program (e^3)

Laboratory of Analytical Geomechanics

Division of Field Engineering for the Environment

Graduate School of Engineering

Hokkaido University

Sapporo, Hokkaido, Japan

ABSTRACT

To more accurately predict the occurrence of slope failure and improve the early warning system, this study attempts to give new insights into the failure mechanism, simulation technology, prediction criteria, etc. For these purposes, the new methodology and numerical approach are developed on different scales, i.e., local-scale, catchment-scale, and regional-scale.

On the local-scale, this study proposes a local shear strength (LSS) method for determining the variable LSS with changes in matric suction (MS) for each soil material point within an unsaturated slope. By using the proposed LSS method, a FEM-MPM hybrid coupled model is proposed. Afterward, the effectiveness of the proposed LSS method-based FEM-MPM hybrid coupled model is validated based on a validation model. The results obtained from the LSS method-based FEM-MPM hybrid coupled model show good agreement with that obtained from the limit-equilibrium method (LEM) and shear strength reduction technique (SSRT). Finally, through the reproduction of the whole landslide process of a natural slope at Nissho Pass in Hokkaido, Japan in 2016, the LSS method-based FEM-MPM hybrid coupled model proposed in this study is proved to be effective for simulating landslide-related large-deformation problems subjected to rainfall infiltration in an unsaturated slope.

On the catchment-scale, this study attempts to simulate the runoff, infiltration, seepage, and instabilities of multi slopes on a small catchment-scale range simultaneously to consider the effect of runoff on the slope instability. For this purpose, this study firstly proposes a hybrid coupled model of surface flow, subsurface flow, and soil mechanics based on shallow water equations, Richards's equation, Green-Ampt infiltration capacity model, and the local factor of safety (LFS) approach. Next, in order to make the proposed hybrid coupled model effective in the practical analysis of runoff, a diffusion wave approximation of shallow water equations is validated by numerical simulations, and then it is used to replace shallow water equations in the proposed hybrid coupled model. Finally, the proposed hybrid coupled model is verified by Abdul and Gillham system and applied to a natural slope in Hokkaido, Japan. The catchment-scale range slope instabilities assessment approach proposed in this study provides an effective approach for simulating heavy rainfall-induced runoff and slope instabilities in the target region, and it has significant implications for precisely determining the dangerous spots (instead of areas) on a catchment-scale range and accurately releasing warning information to the dangerous spots.

On the regional-scale, this study attempts to propose a new determination method for setting an early warning criterion of rainfall and/or snowmelt induced slope failures in seasonally cold regions. For this purpose, this study firstly proposes a combination model for estimating snow density to incorporate hourly snowmelt water into the Japanese early warning system more accurately by using meteorological monitoring data and modeled snow density. Next, based on case studies and parametric analyses for slope stability assessment, new early warning

criteria are proposed for predicting three different patterns of slope failures under two typical types of precipitation (rainfall and snowmelt) conditions. Finally, a new determination method for setting the early warning criterion in seasonally cold regions is proposed by referring to the existing early warning criteria near the target area. This study proposes an effective method for determining the early warning criterion and predicting the occurrence of rainfall and/or snowmelt induced slope failures in seasonally cold regions in the future. Furthermore, numerical simulations are also performed to semi-quantitatively evaluate the impact of uncertainty in climate factors on slope stability, and to evaluate the impact of climate change on the occurrence of slope failure and its probability distribution based on historical statistics and parametric analysis of slope failures. The climate prediction and instability assessment of an actual highway embankment slope is done based on dynamical downscaling techniques and the slope stability assessment approach.

Chapter 1 introduces the background, objective, main technical path, and organization of this study. Chapter 2 reviews several popular numerical methods (FEM, FDM, DEM, DDA, and MPM) and their comparisons, and several slope stability assessment approaches (LEM, SSRT, and LFS) and their comparisons. Chapter 3 introduces an LSS method-based FEM-MPM hybrid coupled model to solve rainfall-induced landslide-related large-deformation problems in unsaturated soil slope on the local-scale. Chapter 4 introduces a hybrid coupled model of surface flow, subsurface flow, and soil mechanics to simulate the runoff, infiltration, seepage, and instabilities of multi slopes on the catchment-scale. Chapter 5 introduces a new determination method for setting an early warning criterion of rainfall and/or snowmelt induced slope failures on the regional-scale. Chapter 6 semi-quantitatively evaluates the impact of climate change on the occurrence of slope failure and its probability distribution based on historical statistics and parametric analysis of slope failures. Chapter 7 summarizes the conclusions and recommendations of the study.

< This dissertation is a modified and revised form of the following original journals and proceedings>

1. Zhu, Y.L., Subramanian, S.S., Ishikawa, T. Evaluating Applicability of Coupled Numerical Methods for Slope Runout Analysis. 58th Annual meeting of Hokkaido Branch Japanese Geotechnical Society. 309-318. Hokkaido, Japan, 2018.1.25-2018.1.26.

2. Zhu, Y.L., Ishikawa, T., Shimizu, Y. Surface Flow Analysis of Typhoon 10 Induced Slope Failure Based on Digital Elevation Modeling. Proceedings of the 9th Symposium on Sediment-Related Disasters. 121-126. Fukuoka, Japan, 2018.9.18-2018.9.19.

3. Zhu, Y.L., Ishikawa, T. Effects of Climate Change on Slope Failure in Snowy Cold Regions. Proceedings of the 61st Symposium of Japanese Geotechnical Society. No. 6-5. 1-6. Tokyo, Japan, 2018.12.14.

4. Zhu, Y.L., Ishikawa, T., Subramanian, S.S. Integrated modeling of fully coupled two-phase surface and subsurface flow. Proceedings of the 16th International Conference on Computer Methods and Advances in Geomechanics. Torino, Italy, 2020.7.1-2020.7.4. (Accepted)

5. Zhu, Y.L., Ishikawa, T., Subramanian, S.S., Luo, B. 2020. Simultaneous analysis of slope instabilities on a small catchment-scale using coupled surface and subsurface flows. Engineering Geology, 275, 105750.

6. Zhu, Y.L., Ishikawa, T., Subramanian, S.S. 2020. Simulation of runoff and infiltration using iterative cross-coupled surface and subsurface flows. Japanese Geotechnical Society Special Publication, 8 (3): 41-46.

7. Zhu Y.L., Ishikawa T., Subramanian S.S., Luo, B. 2020. Early warning system for rainfall and snowmelt induced slope failure in seasonally cold regions. Soils and foundations. (Under review)

ACKNOWLEDGEMENT

Firstly, I would like to express my sincere and deepest gratitude to my supervisor Prof. Tatsuya Ishikawa for his patient guidance, invaluable advice, and continuous support during my doctoral study and related research. Prof. Tatsuya Ishikawa had a profound impact on my academic attitude throughout my doctoral program with his immense specialized knowledge, excellent academic level, and stringent academic spirit. It is Prof. Tatsuya Ishikawa who introduces me to the field of unsaturated soil and encourages me to explore the unknown. His guidance helped me in all the time of my research and writing of this dissertation. Without Prof. Tatsuya Ishikawa's persistent guidance, this dissertation would not have been possible.

Sincere appreciation is due to all members of the doctoral committee, Prof. Yoichi Watabe, Prof. Yasuyuki Shimizu and Prof. (Assoc.) Satoshi Nishimura for their invaluable comments, constructive suggestions, and tremendous support not only on this dissertation but also on annual evaluations.

I would like to offer my sincere thanks to Prof. Yasuyuki Shimizu, Prof. (Assoc.) Tomohito J. Yamada, and Prof. (Assoc.) Koichi Isobe. Prof. Yasuyuki Shimizu taught me a lot about hydrology and gave me many detail guidance on the hydrological simulation. Prof. (Assoc.) Tomohito J. Yamada discussed with me many times about the prediction of meteorological factors caused by climate change and guided me to take these factors into my research. Prof. (Assoc.) Koichi Isobe gave me a lot of guidance in geographic and weather information processing.

I am sincerely grateful to Dr. Srikrishnan Siva Subramanian, Dr. Bin Luo, and Dr. Tsuyoshi Hoshino. Dr. Srikrishnan Siva Subramanian gave important inspiration, invaluable guidance, and continuous help to my research. Dr. Bin Luo and Dr. Tsuyoshi Hoshino have given me a lot of supports in theoretical methods, simulation methods, and data collection. I also gratefully acknowledge the students of the Laboratory of Analytical Geomechanics for their help during these three years.

Finally, my special thanks are extended to my beloved wife Zhang Yafen, my parents, family, and friends. Without their encouragement, support, and confidence in me all through these years, it would not be possible for me to arrive in Japan and complete my doctoral study.

TABLE OF CONTENTS

LIST OF FIGURES

LIST OF TABLES

1 INTRODUCTION

1.1 Background

In seasonally cold regions, the major factors that influence the soil slope stability are heavy rainfall, freeze-thaw action, and snowmelt water infiltration (Siva Subramanian, 2017). The increase in pore-water pressure caused by the rainwater/snowmelt water infiltration resulting in the decrease in matric suction of unsaturated soil is considered the main cause of the landslide/slope failure (Chowdhury and Flentje, 2002; Regmi et al., 2011). Recent studies on geohazards occurred over volcanic soil slopes by Ishikawa and Miura (2011), Ishikawa et al. (2015), and Ishikawa et al. (2016) described that there is a difference in the failure mechanism of slopes between cold regions and warm-temperate regions due to additional factors, i.e., freeze-thaw action causes residual displacement to parallel to the slope surface and shear strain at the subsurface layer. Accordingly, Ishikawa et al. (2015) divided slope failures in cold regions into two main classes: slope failures occur during the snow-melting season (March-April-May) and slope failures occur during heavy rainfall season (August-September).

During the snow-melting season, in recent decades, global warming and climate change lead to the rapid melting of snow cover in seasonally cold regions, like Hokkaido, Japan, and snowmelt water has become the major contributor to the disasters. According to the statistics of the occurrence of sediment-related disasters along the national highways in Hokkaido for 16 years from 1998 to 2013 (Yajima and Kurahashi, 2015), about 40 % of slope failures occurred during the snow-melting season. Among them, 41 % of slope failures were induced by snowmelt, 12 % were induced by snowmelt and rainfall, and the rest of 47 % were induced by rainfall, snow slide, etc. It is worth noting that in the heavy rainfall season, about 37 % of the slope failures were not predicted, while in the snow-melting season, the slope failures that could not be predicted occupy as high as 96 % (Kurahashi et al., 2017). For example, the slope failure occurred successively on May 4th, 2012, and April 7th, 2013 at Nakayama Pass along the National Highway Route 230 in Hokkaido, Japan as shown in Figure 1.1 and Figure 1.2. On May 4th, 2012, within the range of about 40 m in length and up to 110 m in transverse width, approximately 13,000 m^3 of soil moved downward to the slope toe and caused 20 days road closure. On April 7th, 2013, at 11:20 AM, another slope failure occurred with the size of 44 m in length and 19 m in height, and more than 11,000 m^3 of sediment collapsed. Rainfall and snowmelt water were found to be the major contributors to these disasters (Nakatsugawa et al., 2015; Hokkaido Regional Development Bureau, 2013).

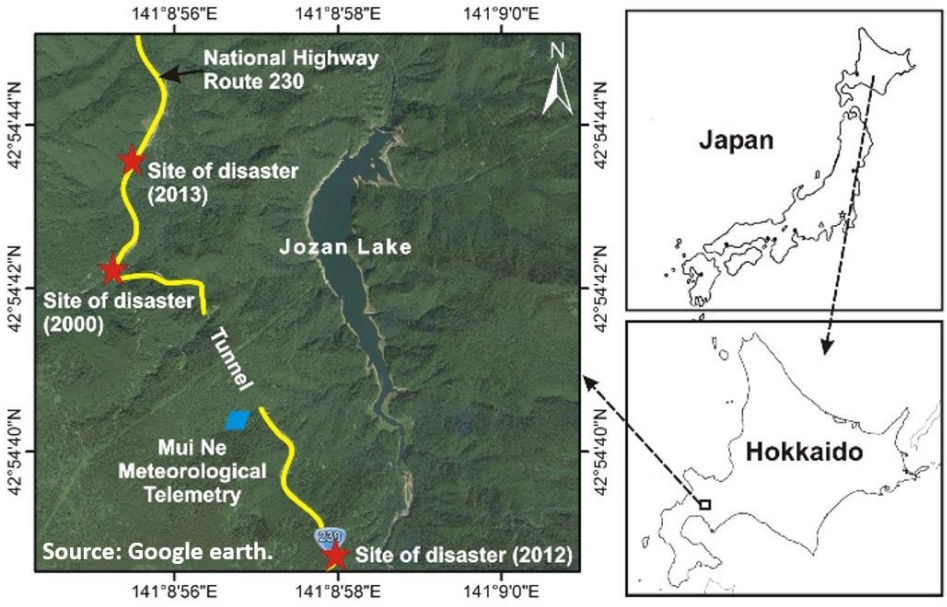

Figure 1.1 Location map of the disaster sites at Nakayama Pass.

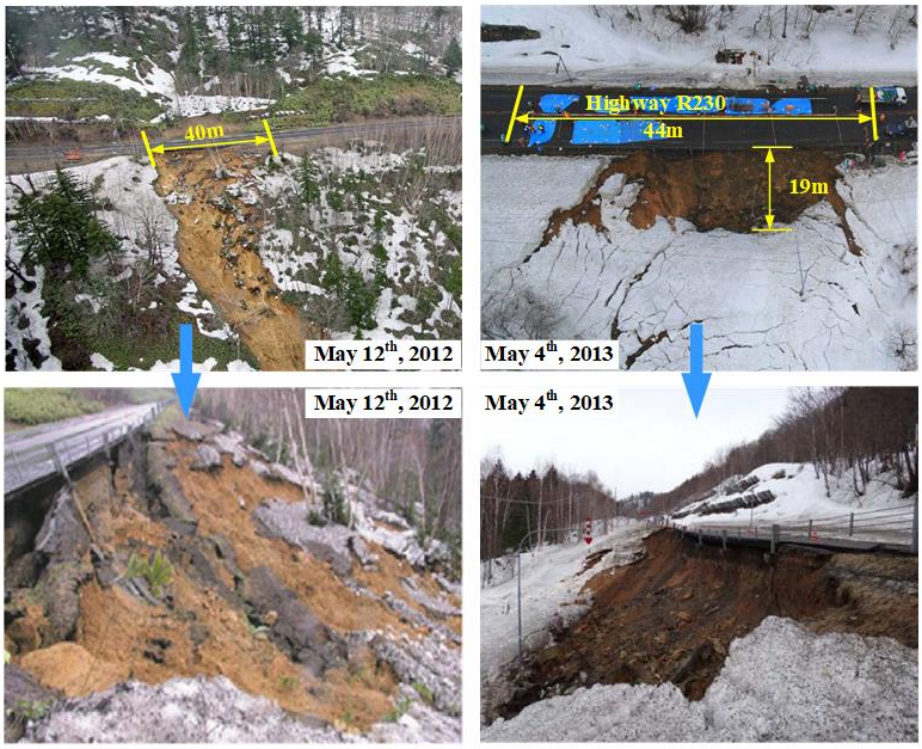

Figure 1.2 Slope failures at Nakayama Pass on Route 230.

On the other hand, during heavy rainfall season, the rainstorms and unexpected typhoons cause sediment-related disasters threatening the lives and public property in many parts of the world, especially in rainy mountainous terrains. During a rainstorm, the infiltration capacity of the slope is not enough to absorb all the rainwater into the soil, resulting in the rainwater that cannot infiltrate into the soil flows in the form of runoff on the slope surface (Cuomo and Della Sala, 2013; Kean et al., 2013; Wei et al., 2017; Van Asch et al., 2018).

Both rainwater infiltration and runoff could deteriorate the slope stability. The rainwater infiltration causes a decrease in the suction in the unsaturated zone and an increase in positive pore pressure due to groundwater in the saturated zone, which eventually induces the occurrence of landslide/slope failure (Chowdhury and Flentje, 2002; Rahardjo et al., 2005; Acharya et al., 2009; Zhang et al., 2014). On the other hand, the runoff, i.e. fast-flowing surface water may cause erosion of the slope surface or pond in the concave areas increasing the possibility of slope failure at some locations such as a road embankment which crosses a gully. For example, during the summer season (August-September), the Japanese archipelago is often struck by violent typhoons with extremely intense rainfalls, which cause a large number of disasters, e.g. floods, debris flows, and landslides (Wang and Sassa, 2003; Fujisawa et al., 2010). According to the statistics of Dahal et al. (2008), from 1951 to 2005, there were 163 typhoon events hit the Japanese archipelago. The slope failures caused by typhoon-induced torrential rain continue to increase in Japan. According to the statistics of the Ministry of Land, Infrastructure, Transport, and Tourism (MLIT), there are 200,000 dangerous valleys and slopes in Japan, and about 1,000 landslide disasters are reported annually (Osanai et al., 2010).

For example, typhoon No. 10 hit Hokkaido, Japan during August 29th-31st in 2016. During this period, near to Nissho Pass along the National Highway Route 274 in Hokkaido, Japan, several serious roadside slope failures, embankment collapses, and debris flows occurred as shown in Figure 1.3(a). Japan Meteorological Agency (JMA) records Typhoon No. 10 was the first typhoon that landed on the main island of Japan from the east coast (Furuichi et al., 2018). According to the rainfall records obtained from the Automated Meteorological Data Acquisition System (AMeDAS), the observed rainfall peaked at 55 mm at 01:00 on August 31st, 2016 and the maximum observed cumulative rainfall as shown by the red line in Figure 1.3(b) was 488 mm which far exceeded the average rainfall in that area and was the highest ever recorded. Moreover, it was more than doubled compared to the second-highest cumulative rainfall (220 mm) observed in this region on August 19th, 2006. Based on the prediction of the occurrence of sediment-related disasters by the Japanese early warning system, the road was closed from 11:15 on August 30th, and the Hokkaido government released heavy rainfall warning information, flood warning information, and disaster warning information at 17:00, 19:00, and 22:00 on August 30th, respectively.

However, little is known about the effects of runoff triggered by typhoons during heavy rainfall season and snowmelt water during the snow-melting season on slope failures and landslides. At least, the current Japanese early warning system does not take these factors into account. Therefore, it is imperative to develop the new methodology and numerical approach on different scales, i.e., local-scale, catchment-scale, and regional-scale, to give new insights into the failure mechanism and simulation technology, and more accurately predict the occurrence of slope failure and improve the early warning system.

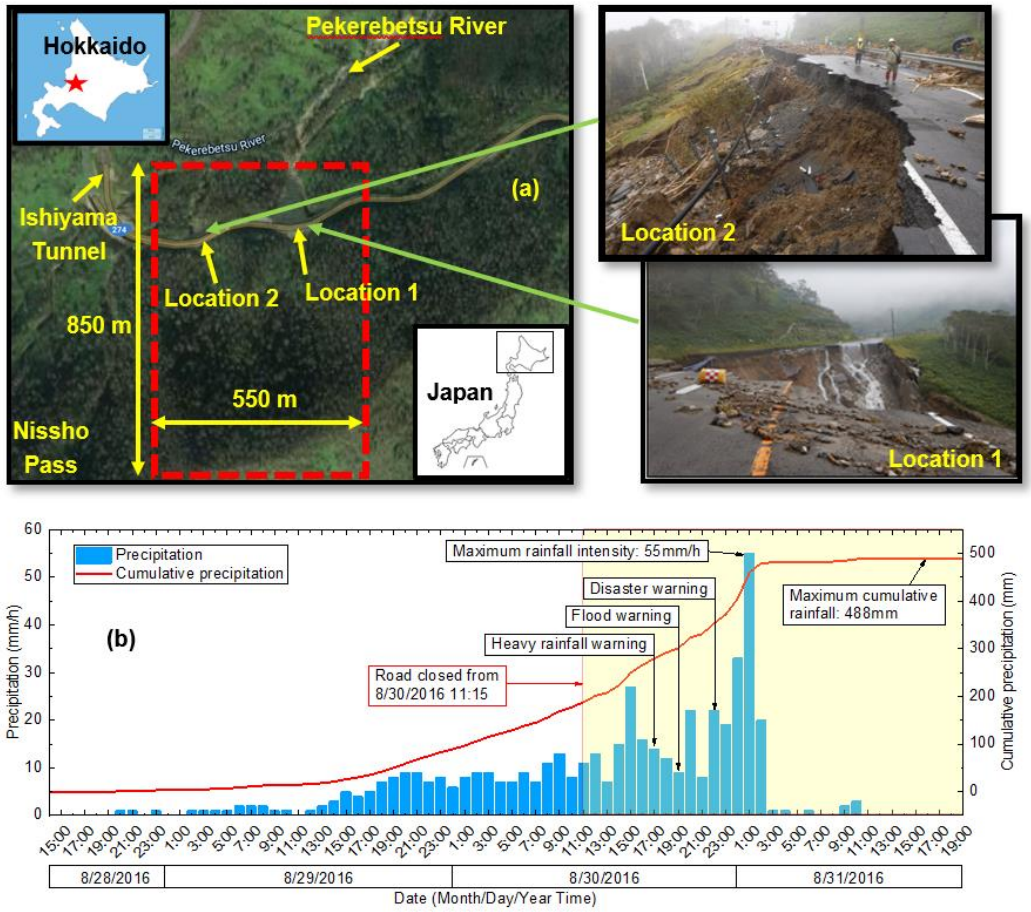

Figure 1.3 (a) Locations of slope failure induced by Typhoon No. 10 along National Highway Route 274; (b) Rainfall recorded during Typhoon No. 10 at Nissho Pass.

1.2 Objectives and Methodology

The objective of this study is to propose a wide-area geohazard risk assessment approach in snowy-cold regions by multiphase soil mechanics and multi-scale analysis for the local government to predict the occurrence of the slope failures a few hours before they occur. For this purpose, this study attempts to,

1. determine the variable shear strength corresponding to the variable matric suction for each soil material point within an unsaturated slope to represent the unsaturated region when using MPM.

2. propose a coupled hydromechanical framework to capture the seepage behavior simulated by FEM and the resulting slope failure behavior simulated by MPM to solve rainfall-induced landslide-related large-deformation problems in unsaturated soil slope.

3. develop a coupled model of surface flow and subsurface flow to simulate the relationship between rainfall, runoff, and infiltration under heavy rainfall conditions.

4. model the rainfall/runoff induced slopes instabilities on a small catchment-scale to determine the dangerous spots in the target area.

5. incorporate the hourly snowmelt water into the Japanese early warning system.

6. develop the existing Japanese early warning system for predicting rainfall and/or snowmelt induced slope failures during the snow-melting season.

7. evaluate the impact of climate change on the occurrence of slope failure and its probability distribution.

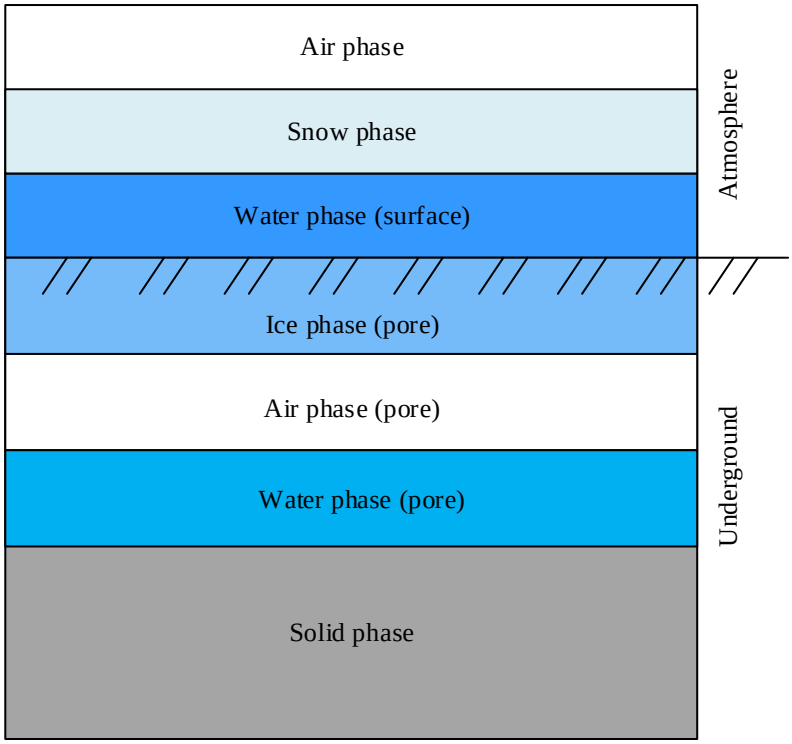

Figure 1.4 Wide-area geohazard risk assessment in snowy cold regions by multiphase soil mechanics.

For these purposes, this study attempts to give new insights into the failure mechanism, simulation technology, prediction criteria, etc. by the numerical simulations that consider multiphase soil mechanics (air, water, ice, solid, etc. as shown in Figure 1.4) on different scales (local-scale, catchment-scale, and regional-scale as shown in Figure 1.5). On the local-scale (<0.001 km^2), this study proposes an LSS method to define the variation of matric suction for each soil material point to represent the variable unsaturated region in a single slope. And then, a hybrid coupled hydromechanical framework is proposed to capture the seepage behavior simulated by FEM and the resulting slope failure behavior simulated by MPM. During this process, the water phase (surface), water phase (pore), and solid phase were simulated. On the catchment-scale (0.001~1 km^2), this study proposes a hybrid coupled model of surface flow, subsurface flow, and soil mechanics to simultaneously simulate runoff, infiltration, seepage, and instabilities of multi slopes on a catchment-scale range. Surface flow is governed by 2D shallow water equations. Subsurface flow is governed by 3D Richards's equation. Two well-known models,

namely the Horton model (Horton, 1933) and the Green-Ampt model (Green and Ampt, 1911), are commonly used to estimate soil infiltration capacity. The parameters in the Horton model have no clear physical basis and must be estimated from the experimental data, while the parameters in the Green-Ampt model have physical meaning and can be estimated from soil properties (Fernández-Pato et al., 2016). Therefore, the Green-Ampt model is used in this study for estimating the infiltration capacity of the ground surface, which could be used to determine the boundary conditions of subsurface flow analysis. The local factor of safety (LFS) approach is used to assess the instabilities of multi slopes. during this process, the air phase, water phase (surface), air phase (pore), water phase (pore), and solid phase were simulated. On the regional scale (>1 km^2), this study proposes a new determination method for setting an early warning criterion in seasonally cold regions for predicting rainfall and/or snowmelt induced slope failures within the subprefecture area or national wide-area and proposes an effective method to semi-quantitatively evaluate the impact of uncertainty in climate factors on slope stability and to evaluate the impact of climate change on the occurrence of slope failure and its probability distribution based on historical statistics and parametric analysis of slope failures. During this process, the snow phase, ice phase, water phase (pore), and solid phase were simulated.

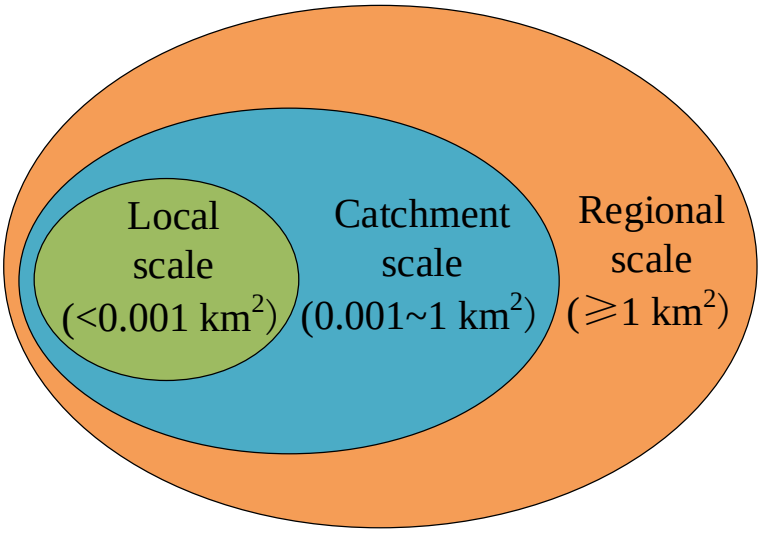

Figure 1.5 Wide-area geohazard risk assessment in snowy-cold regions by multi-scale analysis.

1.3 Organization of Thesis

This dissertation is divided into seven chapters.

Chapter 1 introduces the background and the case examples of soil slope failures analyzed in this study. The objective, purpose, and main technical path are briefly presented. The organization of this dissertation is also outlined.

Chapter 2 outlines several popular numerical methods (FEM, FDM, DEM, DDA, and MPM) for numerical simulations and their comparison, and several slope stability assessment approaches (LEM, SSRT, and LFS)

for simulating slope failure and their comparison. The current research status of the early warning system is also outlined.

Chapter 3 introduces an LSS method for determining the variable LSS with changes in MS for each soil material point within an unsaturated slope on the local-scale. And on this basis, a hybrid coupled hydromechanical framework is proposed to capture the seepage behavior simulated by FEM and the resulting slope failure behavior simulated by MPM to solve rainfall-induced landslide-related large-deformation problems in an unsaturated soil slope.

Chapter 4 introduces a hybrid coupled model of surface flow, subsurface flow, and soil mechanics on the catchment-scale based on shallow water equations, Richards's equation, Green-Ampt infiltration capacity model, and the local factor of safety (LFS) approach. The hybrid coupled model can be used to simulate the runoff, infiltration, seepage, and instabilities of multi slopes on a catchment-scale simultaneously to consider the effect of runoff on the slope instability.

Chapter 5 introduces a new determination method for setting an early warning criterion of rainfall and/or snowmelt induced slope failures in seasonally cold regions. In the new method, the hourly snowmelt water is incorporated into the Japanese early warning system more accurately by using meteorological monitoring data and modeled snow density. Besides, based on case studies and parametric analyses for slope stability assessment, new early warning criteria are proposed for predicting three different patterns of slope failures under two typical types of precipitation (rainfall and snowmelt) conditions.

Chapter 6 semi-quantitatively evaluates the impact of uncertainty in climate factors on slope stability based on numerical simulations, and the impact of climate change on the occurrence of slope failure and its probability distribution based on historical statistics and parametric analysis of slope failures. The parametric analysis of slope failures was performed by imputing three kinds of climate boundary conditions: meteorological monitoring data, meteorological analysis data, and meteorological simulation data. Among them, the meteorological monitoring data is obtained from the Automatic Meteorological Data Acquisition System, named AMeDAS. The meteorological analysis data is a reasonable predicted value of the future meteorology based on the regression analysis of the meteorological monitoring data of the past 120 years. The meteorological simulation data is obtained by downscaling the outputs of Global Circulation Models (GCMs). Finally, climate prediction and assessment of instability of an actual highway embankment slope were done based on dynamical downscaling techniques and the slope stability assessment approach.

Chapter 7 summarizes the findings and conclusions of the study. Recommendations for the analysis and prediction of soil slope failures in Hokkaido, Japan have also been outlined. A brief discussion for the design and mitigation measures of soil slope failure disasters in snowy cold regions is included.

2 LITERATURE REVIEW

2.1 Numerical Methods for Simulating Slope Failure

At present, a lot of researches have been done to assess unsaturated slope instability through seepage analysis and the factor of safety (FOS) calculation by using the finite element method (FEM) (Bui et al., 2008a; Lu et al., 2012; Cuomo and Della Sala, 2013; Siva Subramanian et al., 2017) or finite difference method (FDM) (Regmi et al., 2011; Farshidfar and Nayeri, 2015; Sciarra et al., 2017; Pasculli et al., 2018). Both FEM and FDM replace the original objects with a finite number of nodes and non-overlapping grids connected by nodes, i.e., a particular space discretization in the space dimensions. The principle of these methods is to solve the algebraic equation system composed of the values on the grid node. The difference is that the FDM uses the Taylor series expansion to replace the derivative of the governing equation with the difference quotient of the function values on the grid node, thereby establishing the algebraic equation system composed of the values on the grid node. While, the FEM selects some interpolation points in each finite element to obtain the values on each grid node, thereby establishing the algebraic equation system composed of the values on the grid node. Both FEM and FDM have been widely used in seepage analysis and mechanical analysis, but both of them also suffer from the problem of mesh distortion problems and cannot solve landslide-related large-deformation problems in unsaturated soil slope.

After landslide/slope failure occurs, the collapsed soil moves downward, namely landslides runout, threatening the lives and property of residents living downstream, especially those living near the foothills. Therefore, it is of great significance to study the landslides runout distance to reasonably recommend the installation of barrier structures. Earlier studies made many attempts to develop methods that can simulated landslide runout, e.g. discrete element method (DEM) (Cundall and Strack, 1979; Zhao and Shan, 2013; Zhao and Zhao, 2019), discontinuous deformation analysis (DDA) (Shi, 1989) and material point method (MPM) concurrently developed by several groups (e.g.; Wang et al. 2016; Fern, 2019; Liu et al., 2019). Among them, DEM and DDA are based on discrete blocks and spring units as the research objects. Though both of them can be used to simulate the cracking behavior and large deformation problems of continuous media or model the contact, collision, slipping, and movement of discrete stacked materials, these methods also suffer from low convergence, low accuracy, high experience requirements, and high computational costs. Additionally, another method, MPM is getting continued attention since it was first formulated by Sulsky et al. (1994). In MPM, the material bodies are discretized into a series of material points, which carry all physical information (mass, velocity, acceleration, etc.). The information stored in particles is mapped onto the background grid and the background grid is used to solve the equation of motion like that in FEM (Abe et al., 2013). The MPM combines the advantages of both Eulerian and Lagrangian schemes and avoids the problem of mesh distortion

problems in FEM (Sun et al., 2015), which makes MPM has higher computing efficiency compared with DEM and DDA.

The single-phase (solid phase) MPM has been maturely applied to the simulation of dry soil landslides. For example, Sun et al. (2015) validated the accuracy of the MPM in runout analysis based on a simple numerical example of a two-dimensional (2D) landslide experiment conducted by Bui et al. (2008b). Woo and Rodrigo (2018) presented a methodology that relies on block-structured rectilinear background grids with hanging nodes to improve computational efficiency. Zhang et al. (2019) simulated the dynamic compaction of rockfill by the MPM and developed a rigid-flexible contact algorithm to simulate the dynamic contact of the hammer with soil. Li et al. (2020) simulated the landslide debris movement and interaction between landslide debris and baffle structures using a 3D MPM model. Recently, MPM has also been applied to model rapid failure behavior in a soil-water mixture using two Lagrangian material point layers to represent the solid skeleton phase and pore water phase (Bandara and Soga, 2015; Soga et al., 2016, Liu et al., 2017). For example, Bandara and Soga (2015) presented the formulation and implementation of a numerical procedure based on MPM to solve fully coupled dynamic problems that undergo large deformations in saturated soils. However, the formulation they presented cannot directly model the behavior in unsaturated soils. Since matric suction is very important when modeling problems that involve unsaturated soil, they proposed a simple approach to roughly model the unsaturated soil behavior using the Bishop's effective stress concept (Bishop, 1959) that is considering the whole unsaturated region above the phreatic surface with a same constant matric suction. Obviously, this assumption is insufficient due to the variation of matric suction was not taken into account in the unsaturated zone. From the view of the variation of matric suction in unsaturated soil, the seepage analysis with changes in pore water pressure is one of the fundamental challenges when using MPM. It is worth noting that the traditional numerical method, FEM, has advantages than other methods, and has been commonly used in the general commercial software packages which are designed to analyze seepage. Therefore, to propose a FEM-MPM hybrid coupled computational framework will give full play to their respective advantages in the simulation of seepage and landslides runout.

2.2 Coupled Models of Surface Flow and Subsurface Flow

At present, many studies simulate the runoff in a large area for erosion and flooding (Gomi et al., 2008; Fernández-Pato et al., 2016; Rengers et al., 2016; Malow et al., 2017; Wu et al., 2018). Some earlier studies made attempts to develop models that can describe the behavior of surface and subsurface flow. Tian and Liu (2011) coupled two-dimensional (2D) Saint Venant equations and three-dimensional (3D) Richards's equation in an Integrated Surface Water-Ground water Model (ISWGM). Fernández-Pato et al. (2016) combined 2D shallow water equations with two infiltration models, the Horton model and the Green-Ampt model, for estimating the runoff and infiltration in a watershed. Heavy rainfall-induced runoff may cause large-scale erosion and has a significant impact on the instability of the slope (Gonzalo et al., 2017; Chan et al., 2018; Jing

et al., 2019; Chiu et al., 2019), especially in the mountainous areas with catchment terrain. However, very few studies have coupled surface flow, subsurface flow, and soil mechanics for simulating slope instabilities in a wide area. When performing runoff analyses of the ground surface or seepage analyses of the unsaturated soil, two stages of rainwater infiltration need to be considered from rainfall intensity and rainfall duration point of view (Tan et al., 2018). The first stage (rainfall infiltration stage) is that raindrops directly infiltrate into the soil after reaching the ground surface, and this process usually occurs during the light rainfall or in the early stage of heavy rainfall. The second stage (runoff infiltration stage) is that part of runoff from the upstream infiltrates into the soil, and the rest flows downstream with rainwater. This process usually occurs in the later stage of heavy rainfall. This is a complicated process and brings challenges to its simulation. Therefore, both on catchment-scale and local-scale, during the rainfall-induced slope instability analysis, the impact of runoff is always neglected to simplify calculations (Liu et al., 2017; Chiu et al., 2019). Two assumptions of the rainfall infiltration are generally used. One is that the rainfall infiltration equals to the rainfall intensity. Another is that the rainfall infiltration equals to the component of rainfall intensity perpendicular to the boundary, and the component of rainfall intensity parallel to the boundary (surface runoff) completely drains away instantly. Obviously, the above assumptions cannot fully reproduce the actual processes of rainfall/runoff infiltration, especially under heavy rainfall conditions (rainfall intensity is much larger than the infiltration capacity). Currently, there are no simplified methods or numerical models developed to simulate the slope instability by coupled surface and subsurface flow during heavy rainfall.

2.3 Slope Stability Assessment Approaches

From the view of slope stability analysis, the limit-equilibrium method (LEM) and shear strength reduction technique (SSRT) are commonly used in some general commercial software packages e.g. GeoStudio (GEO-SLOPE International, 2007) and FLAC^{3D} (Itasca, 2012). The LEM discretizes the mass of a potential failure slope into smaller vertical slices and assesses the ratio of shear strength to shear stress for all slices as the Factor of Safety (FOS) of an identified or assumed potential failure surface (Bishop, 1955; Morgenstern and Price, 1965). While the determination of where the failure initiates or the ultimate geometry and position of a landslide failure surface is one of the fundamental challenges when using LEM (Lu et al., 2012). Unlike conventional LEM, it is not necessary to specify the shape of the failure surface in advance when using the SSRT (Sciarra et al., 2017; Pasculli et al., 2018). The FOS is defined as the ratio of the real shear strength to the reduced shear strength of the soil. The failure surface is determined by reducing the strength parameters (cohesion and internal friction angle) of the soil until the slope becomes unstable (Farshidfar and Nayeri, 2015). However, it is worth noting that LEM and SSRT are effective for the stability analysis of a single slope but not feasible for the stability analysis of multi slopes on a catchment-scale. Lu et al. (2012) proposed an approach, i.e. local factor of safety (LFS) approach to quantify the FOS of a slope under rainwater infiltration and verified that the assessment of the LFS approach is consistent with the LEM. Furthermore, the LFS

approach has the potential to overcome several major limitations in the classical FOS methodologies, such as the initiation and evolution of instability with changes in pore water pressure, and the inherent underestimation of slope instability (Lu et al., 2012). The LFS approach also has the potential to assume the slope instabilities on a catchment-scale.

2.4 Early Warning Systems of Landslide

Implementation of a territorial early warning system is a cost-effective non-structural risk mitigation measure, and in most instances, the only suitable option (Glade and Nadim, 2014), as people will have sufficient time to relocate themselves by receiving early warning messages before the debris flows or the slope failures occur. Typically, through the prediction and monitoring of meteorological variables, accurate assessment of the probability of occurrence of landslides and timely release of the warning information to the target area for the evacuation of residents are the main goals of early warning systems. Over the years, many scholars have worked on landslide-triggering rainfall thresholds that apply to a certain area (e.g. Caine, 1980; Glade et al., 2000; Godt et al., 2006; Guzzetti et al., 2007; Yin et al., 2010). Grounded in many related studies, in the past few decades, several systems have been designed in both developed and developing countries (UNISDR 2006). For example, the Landslip Warning System set up in Hong Kong, China, the Real-time Monitoring System (RTMS) installed in Malaysia, and the national early warning system (SANF) designed for rainfall-induced landslides in Italy (Piciullo, 2016). In the U.S., a four-level early warning system is implemented in many federal and state agencies (Baum and Godt, 2010; Hong and Adler, 2007). Similar systems also have been developed in other countries (Aleotti, 2004; Frigerio et al., 2014; Intrieri et al., 2012; Lee et al., 2013).

In Japan, Kuramoto et al. (2001) proposed the RBFN (Radial Basis Function Network) method to set non-linear Critical Line (hereinafter, CL) for sediment-related disaster in each 5 km square grid covering all of Japan. Based on this, in 2005 the Japanese government launched a new nationwide early warning system (Osanai et al., 2010). The early warning system utilizes two rainfall indices, 60-min cumulative rainfall (rainfall intensity) and Soil Water Index (hereinafter referred to as SWI), as warning information for heavy rainfall-induced sediment-related disasters. However, the precipitation thresholds of Japanese early warning criteria are much higher than realistic ones in some areas, and the Japan Meteorological Agency (JMA) has been tentatively operating with lower thresholds of SWI up to 50 % to 80 % for its heavy rain warning/advisories (JMA, 2019). On the other hand, the existing precipitation threshold currently set in each 5 km square grid was determined only by using the occurrence of rainfall-induced debris flows and slope failures without considering the long-term snowmelt water infiltration. Due to these facts, the rainfall threshold is not applicable and not realistic for the prediction of snowmelt-induced soil slope failures during the snow-melting season (Siva Subramanian et al., 2018). Therefore, it is indispensable to propose a new early warning criterion for the prediction of rainfall and/or snowmelt induced slope failures in seasonally cold regions, like Hokkaido, Japan.

2.5 Effects of Climate Change on Slope Stability

In the coldest month of the year, the areas where the ground temperature is usually below 0 C are usually defined as cold regions (Andersland and Ladanyi 2003; Li et al., 2018), such as some high latitude regions, like Hokkaido, Japan. In the cold regions, the climate factors (e.g. precipitation, snow melting, and temperature) and their variations have a significant influence on the stability of slopes and cause the occurrence of slope failures or landslides (Dhakal and Sidle, 2004; Crozier, 2010; Coe and Godt, 2012). Ishikawa et al. (2016) described that there is a difference in the failure mechanism of slopes between cold regions and warm-temperate regions due to additional factors, i.e., freeze-thaw action causes residual displacement parallel to the slope surface and shear strain at the subsurface layer. Accordingly, Ishikawa et al. (2015) divided slope failures in cold regions into two main classes: slope failures occur during the snow-melting season (March-April-May) and slope failures occur during heavy rainfall season (August-September). Therefore, it is necessary to discuss the impact of climate change on slope stability during the snow-melting season (March-April-May) and heavy rainfall season (August-September) separately.

During the heavy rainfall season, the global warming is expected to increase the frequency and intensity of severe rainfall events (Chiang and Chang, 2011), and becomes a primary trigger of rapid-moving landslides that cause many fatalities (Stefano and Fausto, 2016). For example, according to the statistical data surveyed by Japan Meteorological Agency (JMA) for 1,000 locations in Japan, the annual average number of rainfall intensity greater than 50 mm/h increased from 195 (1987~1998) to 226 (1999~2010). On the other hand, during the snow-melting season, the climate effects i.e. temperature-controlled freeze-thaw action and snowmelt water infiltration mainly affect the moisture content of the frozen soil (Ishikawa et al., 2015). The mechanical properties of frozen soil are sensitive to temperature and water content (Ting et al., 1983; Yugui et al., 2016). Consequently, climate change also greatly affects the instability of the slopes in cold regions during the snow-melting season. Especially with the intensification of global warming in the past few decades, the threat of natural disasters in cold regions is ever-increasing. For example, investigated by the Ministry of Land, Infrastructure, Transport, and Tourism (MLIT), in April, the average number of geological disasters in Japan increased from about 50 (2008~2012) to near 100 (2013~2017), almost doubled. Therefore, it is reasonable to consider that impact of climate change on slope stability is intensifying, especially during the snow-melting season. However, little is known about the effects of climate changes on slope failures and landslides (Crozier, 2010; Dijkstra and Dixon, 2010; Gariano and Guzzetti, 2016).

From the view of climate change, many attempts were also made to investigate the effect of climate change on landslide occurrence by exploiting downscaled synthetic future climate scenarios obtained from the Global Circulation Models (GCMs) as an input of slope stability (Chiang and Chang, 2011; Shou and Yang, 2015; Ciabatta et al., 2016). Chiang and Chang (2011) presented an analysis of the impact of climate change on landslide activity in a mountainous watershed in Taiwan. They pointed out that the average annual maximum

rainfall will have a 15.2% increase in 2010-2099 compared with that in 1960-2008, and the average total unstable area will have a 12.8% increase. Ciabatta et al. (2016) obtained hourly rainfall and temperature time series in Central Italy by downscaling the outputs of five different GCMs. They employed the PRESSCA system (an operational early warning system developed by The Umbria Region Civil Protection Centre for landslide risk assessment based on the soil saturation conditions to identify rainfall thresholds) for the assessment of climate change impact on landslide hazard in Central Italy for three different periods (1990-2013 (baseline), 2040-2069 and 2070-2099). They found that for the Umbria territory a general increase in landslides occurrence was expected (up to more than 40%) in the future period, mainly during the winter season. It is reasonable to consider that climate change is playing an increasingly important role in inducing slope failures. However, how to assess the impact of climate change on slope stability remains a challenge.

3 LANDSLIDE SIMULATION BY USING LSS METHOD-BASED FEM-MPM HYBRID COUPLED MODEL ON THE LOCAL-SCALE

On the local-scale, the current numerical simulation methods cannot efficiently solve landslide-related large-deformation problems coupled with variable saturation. Therefore, in this chapter, a local shear strength (LSS) method is proposed for determining the variable LSS with changes in matric suction (MS) for each soil material point within an unsaturated slope. By using the proposed LSS method, a FEM-MPM hybrid coupled model (hybrid coupled model means that there are bidirectional coupling process and unidirectional coupling process in the coupled model (Jiang et al., 2014). In this study, the surface flow model and subsurface flow model is coupled in a bidirectional coupling process, and the subsurface flow model and MPM is coupled in a unidirectional coupling process) is proposed, i.e., the variable MS obtained from the seepage analysis performed by the finite element method (FEM) is transferred to the variable LSS of each soil material point in material point method (MPM) by using LSS method. Afterward, the effectiveness of the proposed LSS method-based FEM-MPM hybrid coupled model is validated based on a validation model. Finally, through the reproduction of the whole landslide process of a natural slope at Nissho Pass in Hokkaido, Japan in 2016, the LSS method-based FEM-MPM hybrid coupled model proposed in this chapter is proved to be effective for solving landslide-related large-deformation problems subjected to rainfall infiltration in an unsaturated slope.

3.1 Local Shear Strength (LSS) Method

The shear strength of saturated soil can be described using the M-C failure criterion and the variable effective stress:

$$\tau_f = c' + \sigma' \tan \phi' \tag{3.1}$$

where, τ_f is the shear strength (kPa); c' is the effective cohesion (kPa); ϕ' is the effective internal friction angle (˚); σ' is the effective normal stress on failure plane (kPa).

In reality, the soil above the phreatic surface is unsaturated. In this state, the soil will have higher shear strength than in a saturated state. Currently, two well-known methods are widely used to determine the shear strength of unsaturated soils under different saturation conditions, one of them is to describe the unsaturated soil behavior by using the Bishop's effective stress concept.

$$\sigma' = (\sigma - u_a)_f + \chi(u_a - u_w)_f \tag{3.2}$$

$$\chi = \frac{\theta - \theta_r}{\theta_s - \theta_r} = \frac{1}{\left[1+(aH_p)^n\right]^m} \ , \ m = 1 - \frac{1}{n} \tag{3.3}$$

where, u_a is pore air pressure (kPa), u_w is pore water pressure (kPa); χ is the effective stress parameter, which has a value of 1 for saturated soils and a value of 0 for dry soils. θ is volumetric water content (m^3/m^3); θ_r is

residual voluumatric water content (m^3/m^3); θ_s is saturated volumetric water content (m^3/m^3). α, m, and n are van Genuchten parameters, which can be determined from the Soil Water Characteristic Curve (SWCC). The shear strength of unsaturated soil is defined as:

$$\tau_f = c' + (\sigma - u_a)_f \tan \phi' + (u_a - u_w)_f \chi \tan \phi' \tag{3.4}$$

Another method proposed by Fredlund et al. (1979) assumes that the linear form of the shear strength for unsaturated soil can be formulated in terms of independent stress state variables as shown in Figure 3.1. The location of the Mohr circle plot in the third dimension is a function of the matric suction. The surface tangent to the Mohr circles at failure is referred to as the extended M-C failure envelope for unsaturated soils. The extended M-C failure envelope defines the shear strength of unsaturated soil. The intersection line between the extended M-C failure envelope and the frontal plane is the failure envelope for saturated conditions. The shear strength of unsaturated soil is defined as:

$$\tau_f = c' + (\sigma - u_a)_f \tan \phi' + (u_a - u_w)_f \tan \phi^b \tag{3.5}$$

where, ϕ^b is the angle of internal friction associated with the net normal stress state variable (˚).

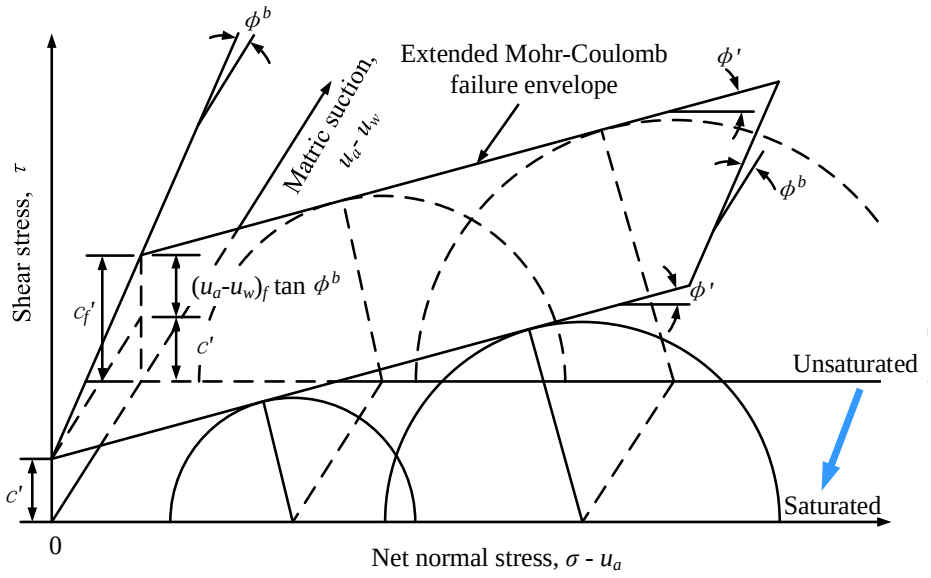

Figure 3.1 Three-dimensional extended M-C failure envelope for unsaturated soils (adapted from Fredlund et al. (1979)).

The shear strength equation (Eq. 3.4) proposed by Bishop (1959) and that (Eq. 3.5) proposed by Fredlund et al. (1979) appears to be similar in form. These two equations can be converted to each other by using the χ parameter.

$$\chi = \frac{\tan \phi^b}{\tan \phi'} \tag{3.6}$$

Unlike the two famous theories above, Lu et al. (2012) described an LFS method by extending the approach described by Iverson and Reid (1992) to the cohesive and variable saturated porous material. The illustration of the concept of a scalar field of the local factor of safety is shown in Figure 3.2.

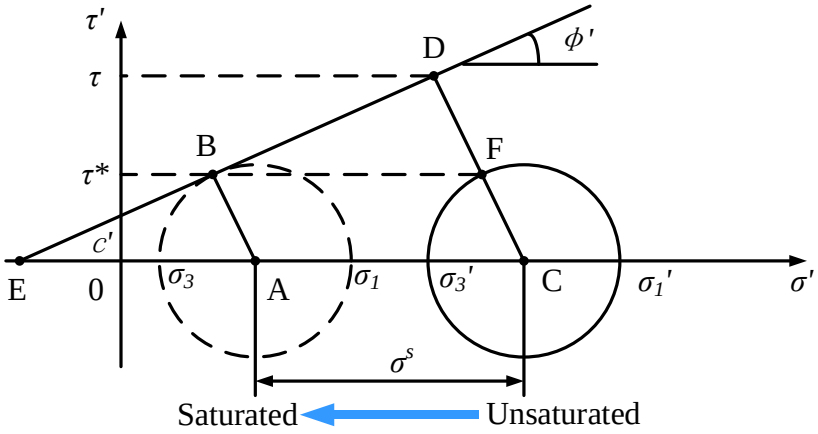

Figure 3.2 Illustration of the concept of a scalar field of the local factor of safety (adapted from Lu et al. (2012)).

In Figure 3.2, the solid circle represents the current state of stress at a point. It assumes that in the process of the saturation conditions of soil changes from unsaturated to saturated under rainfall infiltration, the decrease of matric suction is described by shifting the Mohr circle leftward leftwards until it touches the M-C failure envelope. The size of the Mohr circle remains nearly constant under changing pore water conditions, as the influence of the matric suction on the effective stress is evaluated with Bishop's effective stress.

$$\sigma_1' = \sigma_1 + \sigma^s \tag{3.7}$$

$$\sigma_3' = \sigma_3 + \sigma^s \tag{3.8}$$

$$\sigma^s = \chi(u_a - u_w)_f \tag{3.9}$$

where, σ_1' and σ_3' are the maximum and minimum principal stress for the unsaturated soil (kPa); σ_1 and σ_3 are the maximum and minimum principal stress for the saturated soil (kPa); σ^s is matric suction (kPa).

Therefore, the shear strength of unsaturated soil in the LFS method can be represented as:

$$\tau_f = c' + \left[(\sigma - u_a)_f + \chi(u_a - u_w)_f\right]\tan\phi' \tag{3.10}$$

It is recognized that the form of shear strength of unsaturated soil in the LFS method is the same as that proposed by Bishop (1959) and Fredlund et al. (1979). The difference between the LFS method and the other two methods is that the influence of matric suction on effective normal stress is considered by shifting the Mohr circle on the stress axis. However, when using the MPM to solve the mechanical behavior of saturated/unsaturated soils, the former methods are hard to be used to capture the mechanical behavior in saturated/unsaturated soil. The main reason is that the LFS method is based on the linear elastic model as

described in section 4.1. In the saturated state, the stress circle is allowed to exceed M-C failure envelope. However, in MPM, the soil mechanical model is elastoplastic. Therefore, once the stress circle exceeds M-C failure envelope, the calculation will not converge, which makes the LFS method unavailable for MPM to solve the mechanical behavior of saturated soils. Therefore, in this chapter, an LSS method is proposed and applied in the MPM as shown in Figure 3.3. Since the LFS method has a significant advantage in evaluating the distributed FOS, the LFS method is used in the analysis of slope stabilities on the catchment-scale as described in chapter 4. With the same form as the shear strength equation proposed by Bishop (1959), Fredlund et al. (1979), and Lu et al. (2012), the shear strength equation of unsaturated soil can also be written as:

$$\tau_f = \underbrace{\left[c' + (u_a - u_w)_f \chi \tan \phi'\right]}_{c'_f} + (\sigma - u_a)_f \tan \phi' \tag{3.11}$$

where, c_f' is the intercept of the extended M-C failure envelope with the shear stress axis at a specific matric suction $(u_a - u_w)_f$ (kPa).

Therefore, the variation of unsaturation of material points can be described by including matric suction in the cohesion intercept, and the new cohesion intercept, c_f', is called total cohesion intercept. However, it is worth noting that the inclusion of matric suction in the definition of the cohesion intercept does not necessarily suggest that matric suction is a cohesion component of shear strength (Fredlund et al., 2012). Eq. (3.11) suggests that an increase in the shear strength (the intercept of the M-C failure envelope increase) responding to an increase in matric suction is defined by shifting the M-C failure envelope leftward as illustrated in Figure 3.3. This provides a feasible way to define the variation of matric suction for each soil material point to represent the variable unsaturated region, as the information of cohesion is contained in each soil material point and it is also one of the material properties that must be assigned during the modeling process. The extended M-C failure envelope for each material point is defined as local shear strength (LSS) for each material point (dashed line in Figure 3.3). From Figure 3.3, it can be seen that the smooth transition between unsaturated and saturated soil conditions can also be observed. The shear strength for the unsaturated soil gradually lowers to shear strength for the saturated soil with respect to a decrease in matric suction. The cohesion intercept c_f' finally is equal to the effective cohesion c' when soil becomes saturated.

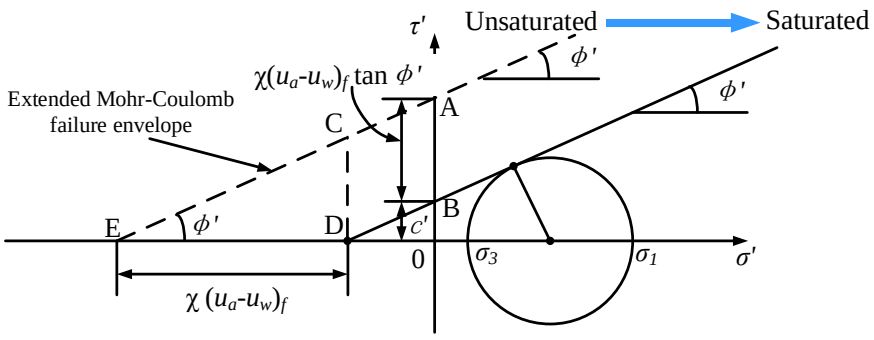

Figure 3.3 Local shear strength (LSS) for unsaturated soil material point.

3.2 Coupled Hydromechanical Framework and Governing Equations

In this section, we firstly propose a coupled hydromechanical framework of FEM and MPM to simulate runoff, seepage, and large deformation of soil. In the FEM-MPM hybrid coupled model, surface flow and subsurface flow are bidirectional coupled through infiltration and exfiltration by using COMSOL Multiphysics software (COMSOL Multiphysics, 2018). The subsurface flow model and soil mechanics model are unidirectional coupled in two ways: (1) the mass of each material point is replaced by the mass of soil and water mixture, and (2) the effect of variable matric suction on the shear strength of each material point is considered into cohesion by using LSS method. Then, the governing equations used in the hybrid coupled model are presented.

3.2.1 Coupled hydromechanical framework

During a rainstorm or torrential rain, when the rainfall intensity is weak, the infiltration rate is less than the infiltration capacity, and as a result, all rainwater infiltrates into the soil. With the continuation of rainfall, the infiltrated rainwater decreases the infiltration capacity of the ground surface. After the rainfall intensity exceeds the soil infiltration capacity, part of the rainwater infiltrates, and the rest flows in the form of runoff on the land surface, while runoff has a significant impact on erosion and landslides on steep slopes (Pan et al., 2016; Wu et al., 2018). On the other hand, in unsaturated soils, the variation of volumetric water content affects matric suction, which in turn affects shear strength. Moreover, it also affects the self-weight and stress distribution. Therefore, the effects of runoff on the soil moisture changes and the effects of soil moisture changes on shear strength and self-weight of unsaturated soil are considered. In the FEM-MPM hybrid coupled model, the surface flow and subsurface flow are simulated by using a FEM software, COMSOL Multiphysics (COMSOL Multiphysics, 2018). The large deformation of the landslide is simulated by using MPM3D (an MPM code that was programmed by the group of Prof. Zhang Xiong at Tsinghua University, http://comdyn.hy.tsinghua.edu.cn/english/mpm3d). The coupled hydromechanical framework is shown in Figure 3.4.

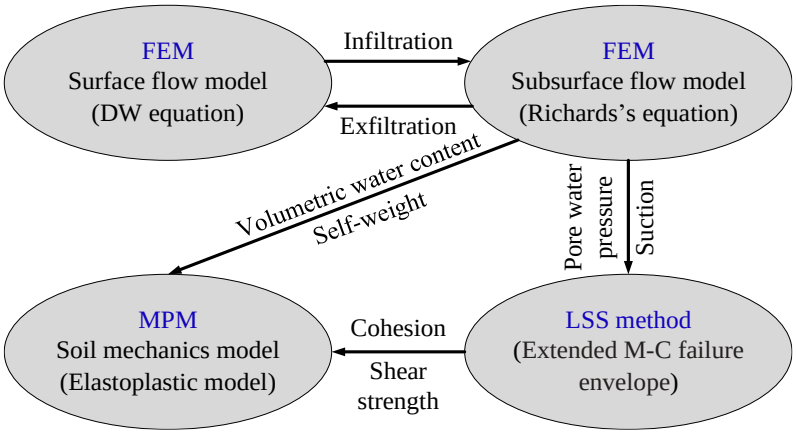

Figure 3.4 Coupled hydromechanical framework by using FEM and MPM.

In the coupled hydromechanical framework, the vertical pressure on the surface caused by the weight of the surface water and the friction caused by the rapid flow of the surface water is not taken into account.

3.2.2 Governing equations for surface flow

Surface flow is calculated by the diffusion wave (DW) approach which can be expressed as follows (Murillo et al., 2007).

$$\frac{\partial h}{\partial t} - \nabla\left(\frac{h^{5/3}}{n_m\sqrt{|S|}}\nabla(H)\right) = R - I \tag{3.12}$$

where, h is water depth (m); R is rainfall intensity (m/s); I is infiltration/exfiltration rate (m/s); H is water surface elevation (m); t is time (s); n_m is Manning's roughness coefficient (s/m$^{1/3}$); S is the gradient of water surface. As the water depth gradient is much smaller than the slope gradient, it can be assumed that S is equal to the slope gradient (Weill et al., 2009).

3.2.3 Governing equations for subsurface flow

The subsurface flow is governed by the following equation (Richards, 1931).

$$\nabla \cdot \left[k_s\, k_r \cdot \nabla\left(H_p + z\right)\right] + Q_w = \left[C_m + S_e S_c\right]\frac{\partial H_p}{\partial t} \tag{3.13}$$

where, C_m is specific moisture capacity (m^{-1}); S_c is specific storage coefficient (m^{-1}); S_e is the effective degree of saturation; H_p is pressure head (m); z is elevation (m); k_r is relative hydraulic conductivity; k_s is saturated hydraulic conductivity (m/s); Q_w is sink and source of water (s^{-1}).

van Genuchten (1980) proposed a Soil Water Characteristic Curve (SWCC) to describe the relationship in C_m, S_e, k_r, θ, and H_p in unsaturated soil. As shown in Eq. (3.14) to Eq. (3.17), these parameters could be specified by the saturated and residual volumetric water content θ_s and θ_r, as well as constants of a, n, m, and l.

$$\theta = \theta_r + S_e(\theta_s - \theta_r) \tag{3.14}$$

$$S_e = \frac{1}{\left[1+(aH_p)^n\right]^m} \quad , \quad m = 1 - \frac{1}{n} \tag{3.15}$$

$$C_m = \frac{am}{1-m}(\theta_s - \theta_r){S_e}^{1/m}(1 - {S_e}^{1/m})^m \tag{3.16}$$

$$k_r = {S_e}^l\left[1 - (1 - {S_e}^{1/m})^m\right]^2 \tag{3.17}$$

3.2.4 Governing equations in MPM

Each calculation step of MPM can be classified into three phases: the initial phase, the Lagrangian phase, and the convective phase (Sun et al., 2015). Three phases of one computational step with MPM are shown in Figure 3.5. In the initial phase, the information (e.g. locations, velocities, accelerations) of the material points are mapped on the background grid, and boundary conditions are applied to the background grid to get the initial values for the solution of global equations. In the Lagrangian phase, the global equations are solved within the

Lagrangian background grid and the material points move with the Lagrangian background grid. The information on the material points is updated. In the convective phase, the Lagrangian background grid is reset, while keeping the information of the material points constant.

The stress distribution is calculated with an elastoplastic model, which is governed by mass and momentum balance equations:

$$\frac{d\rho(\theta)}{dt} + \rho(\theta)\nabla \cdot \boldsymbol{v} = 0 \quad \text{(Conservation of mass)} \tag{3.18}$$

$$\rho(\theta)\boldsymbol{a} = \nabla \cdot \boldsymbol{\sigma} + \rho(\theta)\boldsymbol{b} \quad \text{(Conservation of momentum)} \tag{3.19}$$

where, $\boldsymbol{\sigma}$ is the stress tensor (kPa), $\boldsymbol{b}$ is the vector of body forces (m/s^2), $\rho(\theta)$ is the mass density (kg/m^3), $\boldsymbol{a}$ is the vector of acceleration (m/s^2), $\boldsymbol{v}$ is the vector of velocity (m/s).

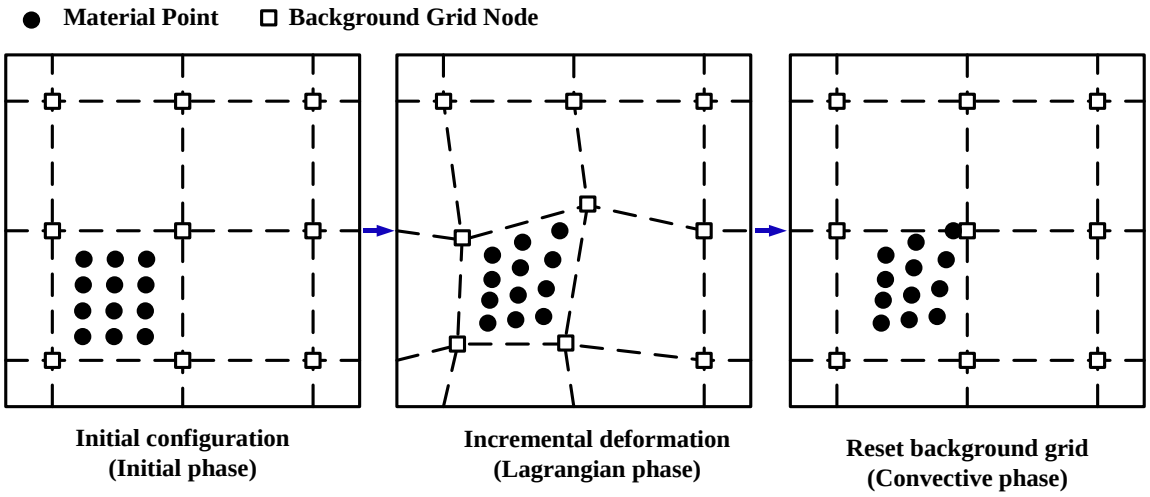

Figure 3.5 Three phases of one computational step with MPM (adapted from Sun et al. (2015))

3.3 Validation of the Proposed LSS Method and FEM-MPM Hybrid Coupled Model

To check the reliability of the LSS method and FEM-MPM hybrid coupled model proposed in this chapter for unsaturated soils, a validation model is simulated by the FEM-MPM hybrid coupled model comparing with the other two commonly used methods: LEM and SSRT. The LEM and SSRT can only give the slip surface (the applicability has been validated by many researches and actual cases), but they cannot simulate the runout distance. Therefore, the slip surface simulated by LEM and SSRT can be used to check the applicability of the slip surface simulated by the proposed FEM-MPM hybrid coupled model. In the validation model, the water supply (rainfall) is not considered. The two side walls and bottom are impermeable to water. The groundwater level (GWL) is set as 5 m below the ground surface. The model size and boundary conditions are shown in Figure 3.6 and the soil properties are given in Table 3.1. The simulation results of SSRT is obtained from COMSOL (COMSOL Multiphysics, 2018), and the simulation results of LEM is obtained from another commercial slope-stability software package GeoStudio (GEO-SLOPE International, 2007).

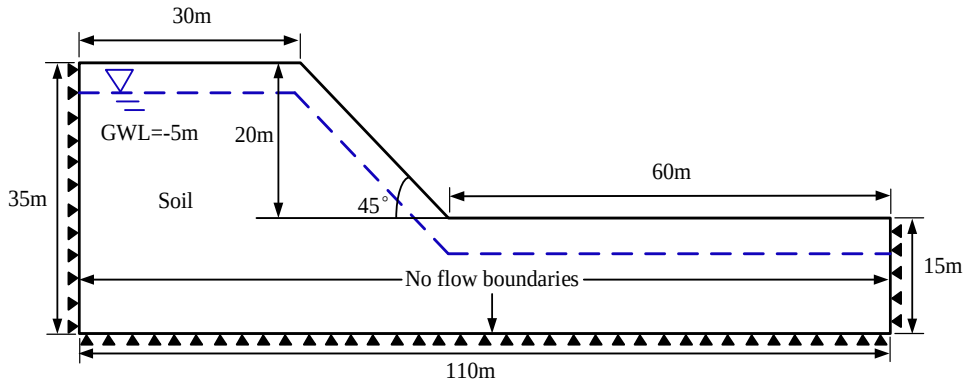

Figure 3.6 Numerical model used for validating the proposed LSS method and FEM-MPM hybrid coupled model.

Table 3.1 Soil properties used in the validation model.

Parameters	Value
Dry density, ρ_s (kg/m^3)	1695
Effective cohesion, c' (kPa)	0
Effective internal friction angle, ϕ' (°)	37
Young's modulus, E (MPa)	50
Poisson's ratio, v	0.3
Saturated hydraulic conductivity, k_s (m/s)	1.12×10^{-5}
Saturated volumetric water content, θ_s (m^3/m^3)	0.36
Residual volumetric water content, θ_r (m^3/m^3)	0.035
van Genuchten parameter, α (1/m)	0.538
van Genuchten parameter, m	0.468

The simulation results are shown in Figure 3.7. Figure 3.7(a) shows the distribution of the pressure head calculated by FEM. Figure 3.7(b) and Figure 3.7(c) show the slip surface calculated by LEM and SSRT with a factor of safety (FOS), respectively. Figure 3.7(d) shows the ultimate slope failure shape simulated by the proposed FEM-MPM hybrid coupled model. From Figure 3.7(d), it is recognized that the occurrence of slope failure is observed. At the same time, in Figure 3.7(b) and Figure 3.7(c), the FOS calculated by LEM (FOS=0.567) and that calculated by SSRT (FOS=0.5895) are less than 1.0, meaning that the slope is in an unstable state, which gives a good verification of the simulation results obtained from FEM-MPM hybrid coupled model. Furthermore, it can be seen that the slip surface simulated by the LEM and SSRT are quite

similar to the ultimate slope failure shape simulated by FEM-MPM hybrid coupled model. This also proves that the FEM-MPM hybrid coupled model proposed in this chapter is effective for simulated slope failure of unsaturated soil. The merit of LEM and SSRT is that they can give the FOS for assessing the danger level of the slope, while they cannot simulate the runout. The advance of MPM is that it can simulate runout while it cannot give FOS. However, the purpose of calculating FOS is to evaluate the stability of the slope. Since the FEM-MPM hybrid coupled model can be used to evaluate the instability of the slope, the calculation of FOS is not important and can be omitted as the concept of "probability of failure" has been considered an alternative or complement to the traditional FOS (Griffiths et al. 2010).

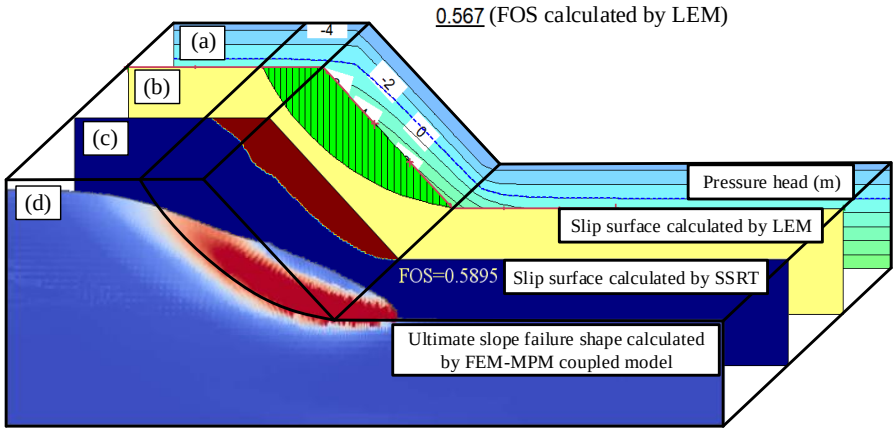

Figure 3.7 (a) Pressure head calculated by FEM; (b) Slip surface with FOS calculated by LEM; (c) Slip surface with FOS calculated by SSRT; (d) Ultimate slope failure shape calculated by FEM-MPM hybrid coupled model.

3.4 Landslides Simulation

3.4.1 Numerical model and rainfall conditions

According to the geological hazard investigation report after the typhoon No. 10 event, runoff played an important role in the embankment slope failures. Based on the digital elevation model (DEM) produced from airborne laser scanning (1 m resolution), a 3D model of the natural mountain area for surface and subsurface flows analysis is built as shown in Figure 3.8(a) (Zhu et al., 2020). Figure 3.8(b) shows the cross-section of the embankment at Location 1 and Figure 3.8(c) shows the material points at the same position used in MPM. The model is composed of three parts: weathered granite, soil, and embankment. The depth of the soil is assumed to be 10 m and embankment is built by expanding the 2D geometry. Soil properties are listed in Table 3.2. The parameters i.e. dry density (ρ_s), saturated hydraulic conductivity (k_s), saturated volumetric water content (θ_s), effective cohesion (c'), and effective internal friction angle (ϕ') have been obtained from laboratory element tests (Ortuño et al., 2017). The parameters for which no laboratory measurements are available i.e. residual volumetric water content (θ_r) and van Genuchten parameters (α and m), were estimated based on the grain size curve of soil (SoilVision, 2018). Although there were three other typhoons before

Typhoon No. 10, since they were at least one week apart from Typhoon No. 10, they had little effect on the groundwater level during Typhoon No. 10. Therefore, the initial groundwater level is set to -5.5 m according to the historical measured average value in the same period of previous years. Manning's coefficient value is 0.3 s/m$^{1/3}$ for the slope, which is the recommended value of the Japan Institute of Country-ology and Engineering (JICE) for mountain grassland. The simulation time is from 19:00 on August 28th, 2016 to 17:00 on August 31st, 2016 for a total of 70 hours with the timestep of 1 hour.

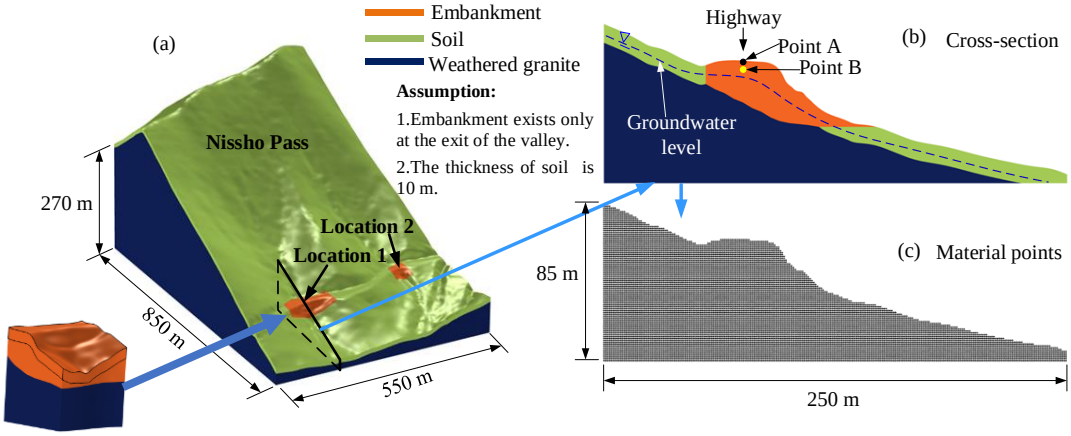

Figure 3.8 (a) Three-dimensional numerical model of a natural mountain area at Nissho Pass; (b) Cross-section of the embankment at Location 1; (c) Material points.

Table 3.2 Soil Properties used for the simulation at Nissho Pass.

Parameters	Embankment	Soil	Weathered granite
Dry density, ρ_s (kg/m^3)	1695	1020	2000
Effective cohesion, c' (kPa)	0	0	37
Effective internal friction angle, ϕ' (°)	37	35	21
Young's modulus, E (MPa)	50	50	500
Poisson's ratio, v	0.3	0.3	0.3
Saturated hydraulic conductivity, k_s (m/s)	1.12×10^{-5}	1.4×10^{-6}	3.47×10^{-9}
Saturated volumetric water content, θ_s (m^3/m^3)	0.36	0.63	0.48
Residual volumetric water content, θ_r (m^3/m^3)	0.035	0.19	0.008
van Genuchten parameter, α (1/m)	0.538	0.810	0.012
van Genuchten parameter, m	0.468	0.437	0.246

3.4.2 Simulation results

The bidirectional coupled surface and subsurface flow analysis are firstly performed using FEM. The simulation time (represented by T) is a total of 70 hours from 20:00 on August 28th, 2016 to 18:00 on August 31st, 2016. The calculation step is 1 hour. After each calculation step (1 hour) of the bidirectional coupled surface and subsurface flow analysis, the volumetric water content and pore water pressure are transferred to the MPM model and used for updating the information of mass self-weight and shear strength of the soil stored in each material point. After trial calculations, it is found that after 15 s, the slope failure shape does not change significantly even if the calculation time is greatly increased. Therefore, the simulation time (represented by t) of a landslide by using MPM is set to 15 s and the calculation step is 0.2 s.

Figure 3.9 shows the distribution of time-dependent surface water depth calculated by FEM. It is recognized that the behavior of the surface runoff is tracked by using the bidirectional coupled surface and subsurface flow model. The surface water flowing from the upstream catchment is gathered at the exit of the valley, resulting in the water depth at the exit of the valley is much higher than other parts of the highway. It means that the runoff from upstream might allow more water to infiltrate into the embankment and cause the possibility of slope failure at the exit of the valley to be much greater than other locations along the highway.

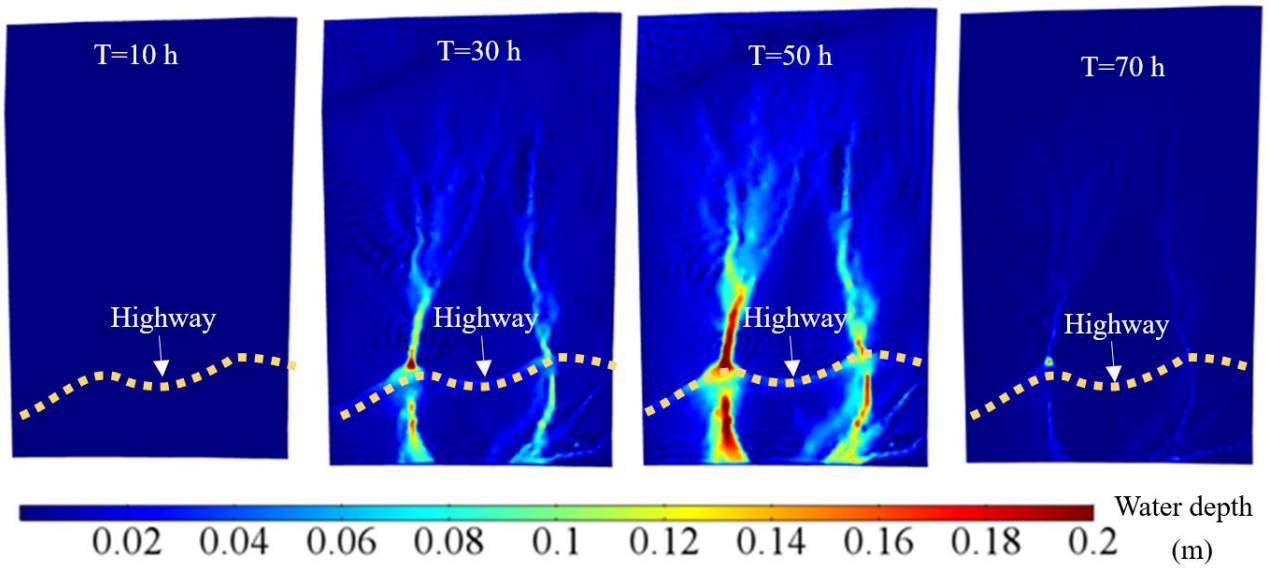

Figure 3.9 Distribution of time-dependent surface water depth (m).

Figure 3.10 shows the distribution of the time-dependent effective degree of saturation (Se). It can be seen that the unsaturated soil lies above the saturated zone. The infiltration of rainwater gradually saturates the soil on the surface layer, thus resulting in the size of the unsaturated zone to become smaller. Figure 3.11 shows the water depth (h) at the road center (Point A in Figure 3.8(b), located on the road surface), and pore water pressure (u_w) and total cohesion intercept (c_f') at an exploratory point (Point B in Figure 3.8(b), located at 1 m deep below the surface). From Figure 3.11, it is identified that the runoff is generated from 22 hours after the rainfall event happens. At the same time, the soil on the surface layer becomes saturated in Figure 3.10 due to

the presence of runoff and the saturated area gradually increases over time. After runoff is generated, u_w has a steep increase and c_f' sharp declines, meaning that the runoff from upstream allows more water to infiltrate into the embankment, thereby causing a more significant decrease in the matric suction and shear strength of the embankment. From Figure 3.11, it can be seen that in most of the time, the depth of water is about 0.05 m and the peak value is about 0.2 m. It indicates that the surface water is very shallow, and its weight is negligible. Therefore, the water pressure is only considered at the interface between runoff and ground surface and the weight of surface water is ignored. Figure 3.12 shows the distribution of effective plastic strain (*EPS*) and slope failure shape with large deformations at 15 s in landslide simulation. It is recognized that the slope is stable before 30 h due to a large size unsaturated zone lies above the saturated zone. The high matric suction causes the high shear strength of the embankment soil. With the infiltration of rainwater, the matric suction gradually decreases, resulting in a decrease in shear strength of the embankment soil. Finally, the occurrence of slope failure started at approximately 40 h (the highway was already closed) and reached its ultimate shape at 50 h (slope failure was complete), which is consistent with reality (the road was already closed). Therefore, this simulation has shown the capability of the LSS method and FEM-MPM hybrid coupled model proposed in this chapter to capture the slope failure in unsaturated soil when modeling landslide related large deformation problems. However, the interface change between runoff and soil ground during the landslide is not considered in this study.

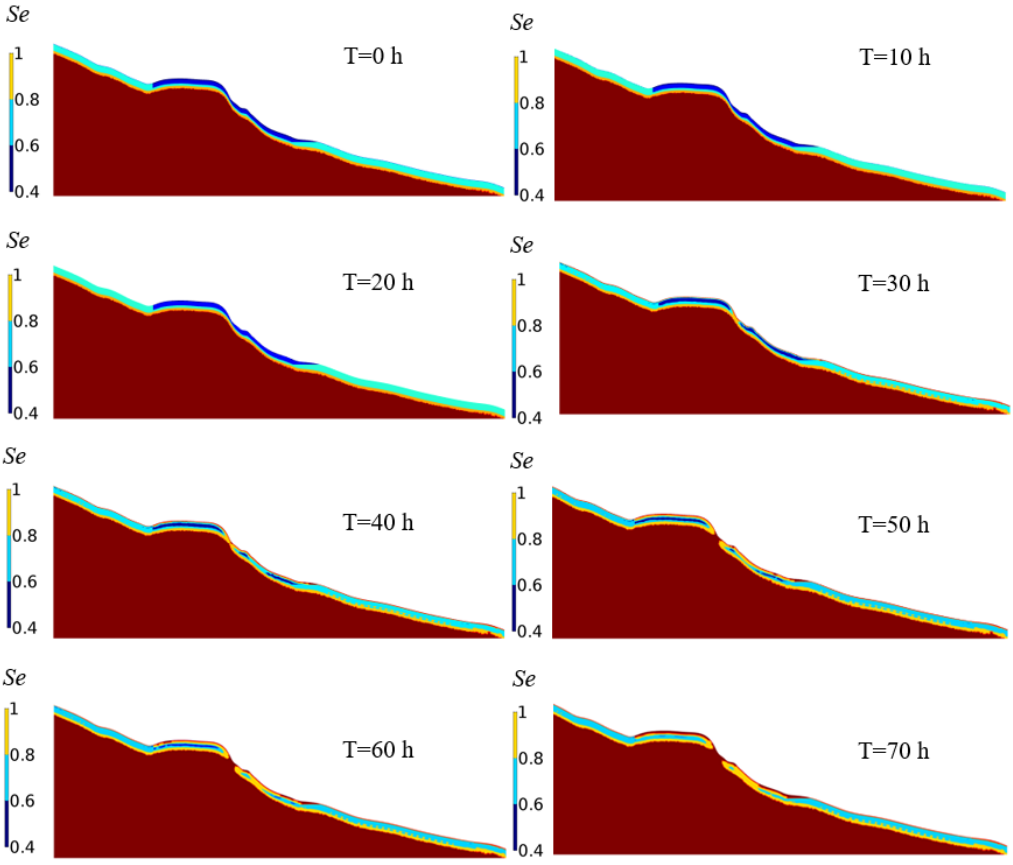

Figure 3.10 Distribution of time-dependent effective degree of saturation.

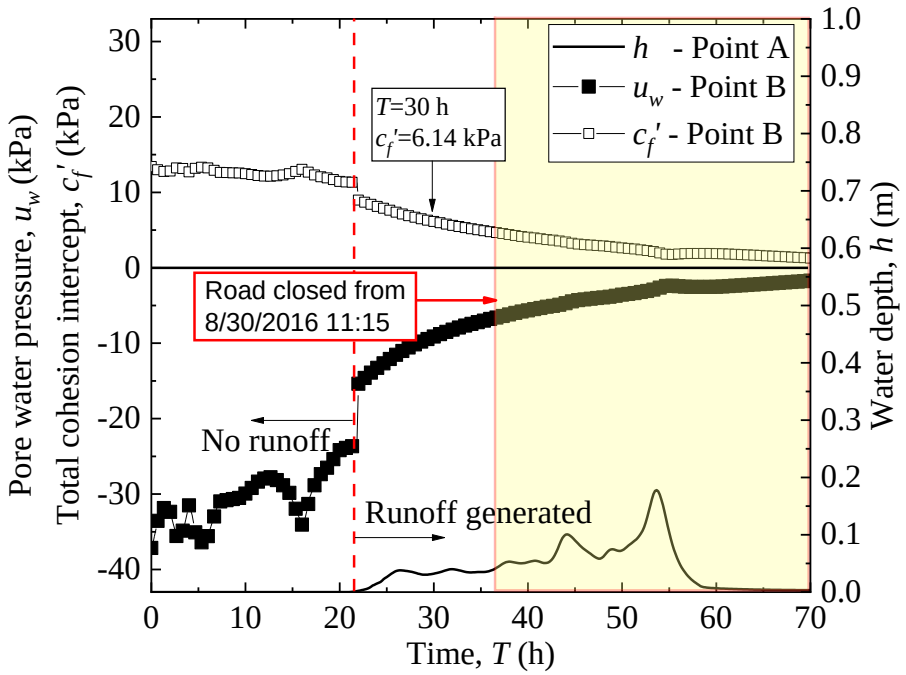

Figure 3.11 Time-dependent water depth (m), pore water pressure (kPa), and total cohesion intercept (kPa).

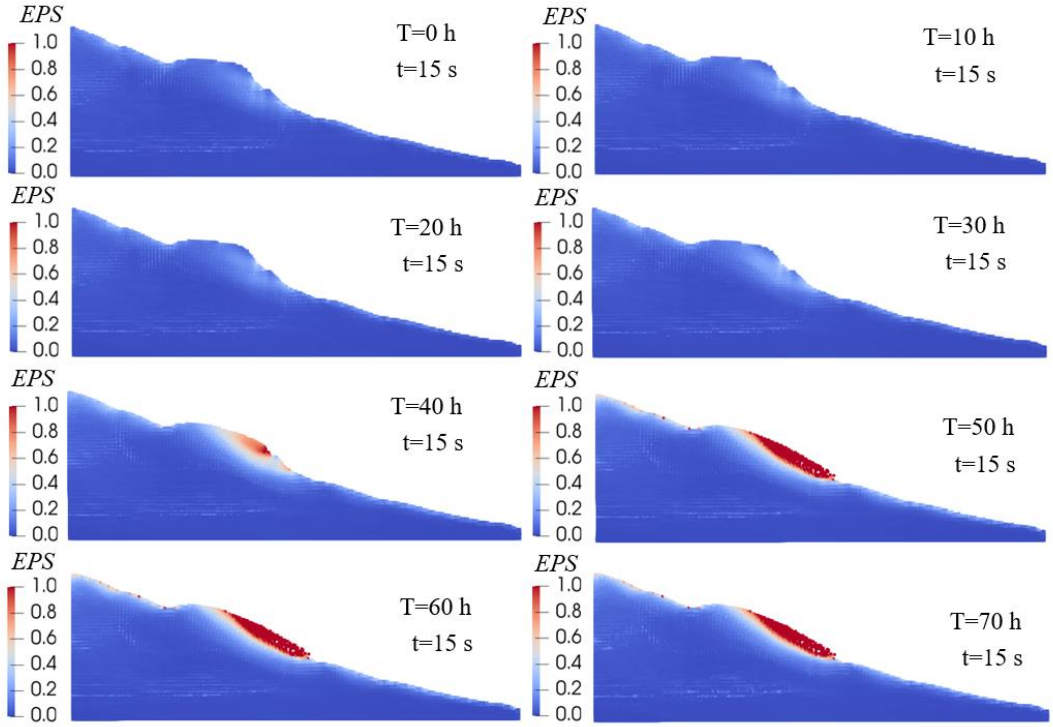

Figure 3.12 Distribution of effective plastic strain and Slope failure shape with very large deformations.

3.5 Summary of This Chapter

This chapter proposes a local shear strength (LSS) method for determining the variable LSS with changes in matric suction (MS) for each soil material point within a small catchment-scale unsaturated soil slope. The decrease in LSS corresponding to the decrease in MS is defined by shifting the Mohr-Coulomb (M-C) failure envelope rightward for each soil material point during rainfall infiltration. By using the proposed LSS method, a FEM-MPM hybrid coupled model is proposed, i.e., the variable MS obtained from the seepage analysis performed by the finite element method (FEM) is transferred to the variable LSS of each soil material point in material point method (MPM) by LSS method. Afterward, the effectiveness of the proposed LSS method-based FEM-MPM hybrid coupled model is validated based on a validation model. The slip surface obtained from the LSS method-based FEM-MPM hybrid coupled model shows good agreement with that obtained from the limit-equilibrium method (LEM) and shear strength reduction technique (SSRT). Finally, through the reproduction of the whole landslide process of a natural slope at Nissho Pass in Hokkaido, Japan in 2016, the LSS method-based FEM-MPM hybrid coupled model proposed in this chapter is proved to be effective for solving landslide runout subjected to rainfall infiltration within a small catchment-scale unsaturated soil slope.

The research findings in this chapter indicate that the LSS method and FEM-MPM hybrid coupled model proposed in this chapter provides a feasible way to simulated rainfall-induced landslide runout in unsaturated soil slopes. It is of great significance to evaluate the landslides movement distance and reasonably recommend the installation of barrier structures in the actual design and maintenance works. However, the internal moisture changes and the dynamic support provided by the runoff during the movement of the landslide are not considered in this study. These should be considered in the future assignments of this study.

4 ANALYSIS OF SLOPE INSTABILITY WITH COUPLED SURFACE AND SUBSURFACE FLOW ON THE CATCHMENT-SCALE

On the catchment-scale, during the rainfall-induced slope instability analysis, the impact of runoff is always neglected to simplify calculations. Besides, the current numerical methods cannot simultaneously simulate the instability of more than two slopes. Therefore, in this chapter, to consider the effect of runoff on the slope instability, a hybrid coupled model of surface flow, subsurface flow, and soil mechanics (the surface flow model and subsurface flow model is coupled in a bidirectional coupling process, and the subsurface flow model and soil mechanic model is coupled in a unidirectional coupling process) is proposed to simulate the runoff, infiltration, seepage, and instabilities of multi slopes on a small catchment-scale simultaneously based on shallow water equations, Richards's equation, Green-Ampt infiltration capacity model, and local factor of safety (LFS) approach. Next, to make the proposed hybrid coupled model effective in the practical analysis of runoff, a diffusion wave (DW) approximation of shallow water equations is validated by numerical simulations, and then it is used to replace shallow water equations in the proposed hybrid coupled model. Finally, the proposed hybrid coupled model is verified by Abdul and Gillham system and applied to a natural slope in Hokkaido, Japan. The numerical results highlight the influences of runoff from upstream on the embankment slope failure at the exit of the gully. Furthermore, the catchment-scale range multi slopes instabilities assessment approach proposed in this chapter provides an effective approach for simulating heavy rainfall-induced runoff and multi slopes instabilities in the target region, and it has significant implications for precisely determining the dangerous spots (instead of areas) on a catchment-scale and accurately releasing warning information to the dangerous spots in the target region.

4.1 Numerical Modeling Strategy

The surface and subsurface flow are complex environmental systems that often behave in a coupled manner. In this chapter, a hybrid coupled model of surface flow, subsurface flow, and soil mechanics is proposed by using COMSOL Multiphysics software (COMSOL Multiphysics, 2018). The surface flow model and subsurface flow model are bidirectional coupled through infiltration and exfiltration. The subsurface flow model and soil mechanics model are unidirectional coupled in two ways: (1) the body load function that depends on the volumetric water content is applied to a linear elastic soil mechanics model to manifest the effect of moisture variation on the self-weight and stress distribution, and (2) the effect of volumetric water content variation on the pore water pressure (suction) is considered for evaluating effective stress. Accordingly, the local factor of safety can be calculated by using effective stress as shown in Figure 4.1.

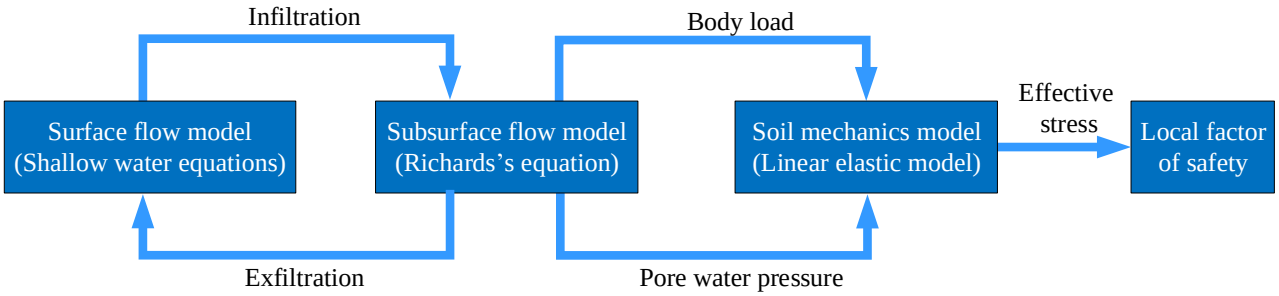

Figure 4.1 Structure of coupled hydrological and slope stability model.

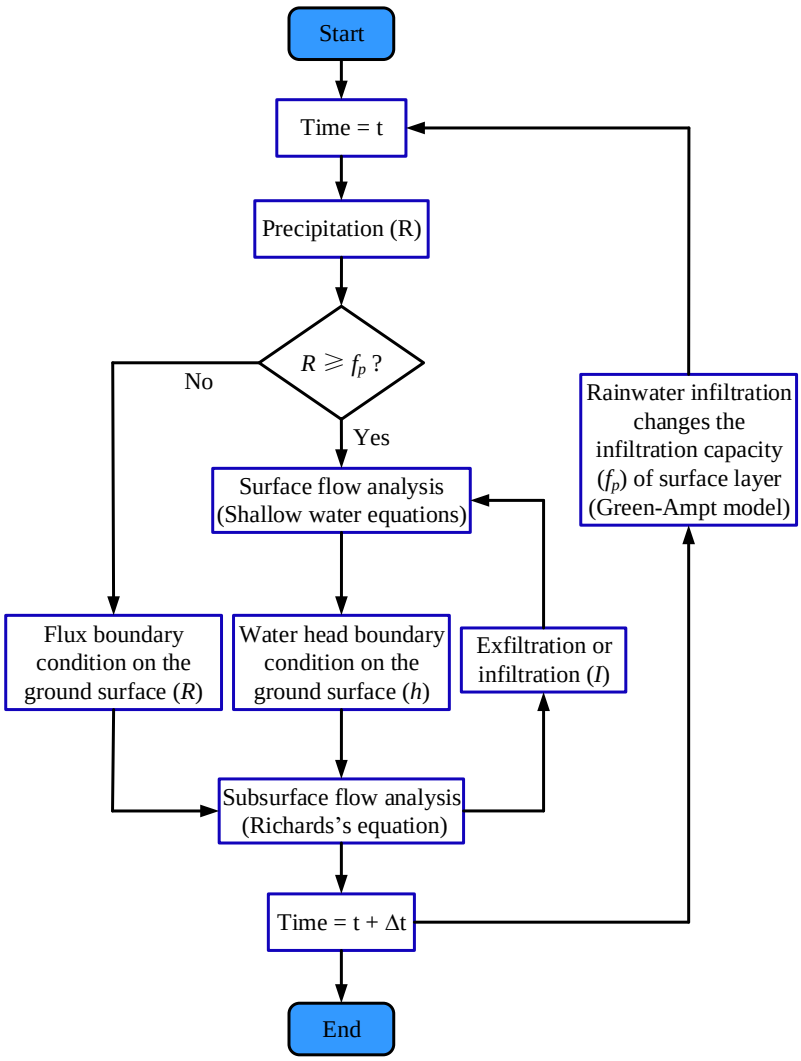

Figure 4.2 Flowchart of the time-marching scheme in iterative cross-coupled surface and subsurface flow model.

During torrential rain, rainwater infiltration is a two-stage process, i.e. rainfall infiltration (rainfall derived infiltration) in the early stage of the rainfall event, and runoff infiltration (runoff derived infiltration, in this case, the infiltration is controlled by the surface water depth rather than the rainfall intensity) in the later stage of the rainfall event. Therefore, the Green-Ampt model is used for estimating the infiltration capacity (f_p) of the ground surface to determine the boundary conditions of subsurface flow analysis. That is if rainfall intensity

(R) is smaller than the infiltration capacity (f_p), all rainwater will infiltrate into the ground. If the rainfall intensity exceeds the infiltration capacity (f_p), part of rainwater infiltrates into the ground, and the rest generates runoff on the ground surface. On the other hand, the exfiltration (positive value) and infiltration (negative value) calculated from the subsurface flow model is added to the surface flow model as a source and sink item. Then, the infiltrated rainwater causes the decrease of the infiltration capacity (f_p) of the ground surface, and the calculation of the next time step will be carried out. This section proposes an iterative cross-coupled surface and subsurface flow model to simulate this process. The flowchart of the time-marching scheme in iterative cross-coupled surface and subsurface flow model is shown in Figure 4.2.

4.2 Governing Equations

The governing equations in the proposed hybrid coupled model are represented in this part. The surface flow is governed by the 2D shallow water equations, and the subsurface flow is governed by the 3D Richards's equation. The soil infiltration capacity is estimated by the Green-Ampt model, and the slope instabilities on a small catchment-scale are assessed by the LFS approach.

4.2.1 Governing equations for surface flow

Surface flow is calculated by 2D shallow water equations which can be expressed as follows (Murillo et al., 2007).

Equation of continuity:

$$\frac{\partial h}{\partial t} + \frac{\partial (hu)}{\partial x} + \frac{\partial (hv)}{\partial y} = R - I \tag{4.1}$$

Equations of motion:

$$\frac{\partial (uh)}{\partial t} + \frac{\partial (hu^2)}{\partial x} + \frac{\partial (huv)}{\partial y} = -hg\frac{\partial H}{\partial x} - hgS_{fx} + D_x \tag{4.2}$$

$$\frac{\partial (vh)}{\partial t} + \frac{\partial (huv)}{\partial x} + \frac{\partial (hv^2)}{\partial y} = -hg\frac{\partial H}{\partial y} - hgS_{fy} + D_y \tag{4.3}$$

where, h is water depth (m); u, v is water velocity in the x and y direction (m/s); R is rainfall intensity (m/s); I is infiltration rate (m/s); g is the gravitational acceleration (m/s^2); H is water surface elevation (m); t is time (s); D_x, D_y is diffusion term in the x and y direction; S_{fx}, S_{fy} is the friction slope in the x and y direction respectively, usually written in term of the Manning's roughness coefficient n_m (s/m$^{1/3}$).

$$S_{fx} = n_m^2 u\sqrt{u^2 + v^2}/h^{4/3} \ , \ S_{fy} = n_m^2 v\sqrt{u^2 + v^2}/h^{4/3} \tag{4.4}$$

The first terms on the right-hand side of the equations of motion, Eq. (4.2) and Eq. (4.3), represent the driving force from the slope gradient and water depth gradient. The second terms represent the drag force due to friction (friction loss gradient). The third terms are diffusion terms, and they can be assumed by the following conditions.

$$D_x = \frac{\partial}{\partial x}\left[\nu_t \frac{\partial(uh)}{\partial x}\right] + \frac{\partial}{\partial y}\left[\nu_t \frac{\partial(uh)}{\partial y}\right] \ , \ D_y = \frac{\partial}{\partial x}\left[\nu_t \frac{\partial(vh)}{\partial x}\right] + \frac{\partial}{\partial y}\left[\nu_t \frac{\partial(vh)}{\partial y}\right] \quad (4.5)$$

In which, ν_t is an eddy viscosity coefficient (m^2/s), and it can be assumed as follows (Zeng et al., 2010).

$$\nu_t = \lambda h U^* \quad \text{and} \quad U^* = \sqrt{ghS} \quad (4.6)$$

where, U^* is the frictional velocity (m/s); λ is dimensionless eddy viscosity, and its standard value for an infinitely wide channel is 0.067 (Zeng et al., 2010); S is the gradient of water surface. As the water depth gradient is much smaller than the slope gradient, it can be assumed that S is equal to the slope gradient (Weill et al., 2009) as shown in Figure 4.3.

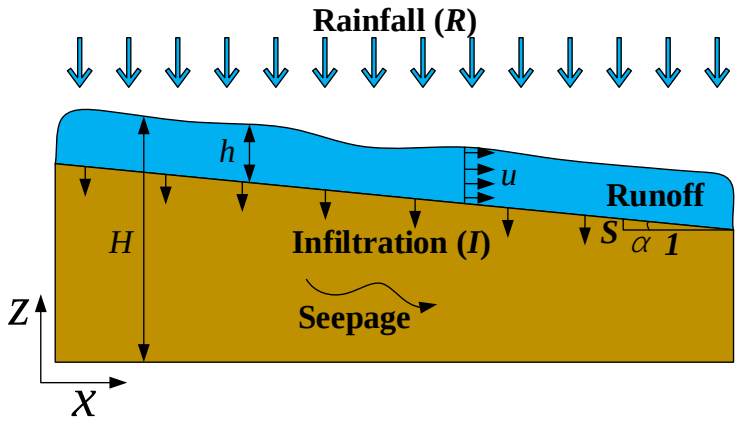

Figure 4.3 Conceptual schematic of the surface flow model.

In principle, by simultaneously solving the equations of continuity and motion, the behavior of the surface runoff can be tracked, and the water depth and velocity can be obtained at any interesting location. However, the timesteps need to be set very small, or simulations only can be performed under relatively flat terrain conditions, which leads to the computational efficiency of the shallow water equations is low for the practical runoff analysis in vast mountainous areas (Rengers et al., 2016). The main reason can be considered as that some insignificant terms in the equation of motion, Eq. (4.2) and Eq. (4.3), significantly increase the calculation time and decrease convergence. Therefore, to ignore the insignificant terms in the equations of motion, the contribution of each term was examined by performing numerical simulations using seven surface flow models with different slope angles (<1˚, 5˚, 10˚, 15˚, 30˚, 45˚, and 60˚). In the surface flow model, Manning's coefficient value is 0.3 $s/m^{1/3}$. A fixed water head boundary condition (h=0.001 m) is applied to the left side and zero gradient boundary condition ($\partial h/\partial x$=0) is applied on the right side. The time-dependent analysis is performed, and the simulation time is 10 s with the timestep of 1.0×10^{-4} s. Table 4.1 shows the simulation results, i.e. the contribution of each term in Eq. (4.2) as a fraction of 100 % of the total for surface water flow under different slope angles.

Table 4.1 Contribution of each term in the equations of motion for surface water flow.

Slope angle (°)	Inertia term $\frac{\partial(uh)}{\partial t}$ (%)	Advection term $\frac{\partial(hu^2)}{\partial x}$ (%)	Driving force term $-hg\frac{\partial H}{\partial x}$ (%)	Friction term $-hgS_{fx}$ (%)	Diffusion term D_x (%)
<1	<0.001	<0.001	50.038	49.961	<0.001
5	<0.001	0.005	49.584	50.410	<0.001
10	<0.001	0.011	49.595	50.393	<0.001
15	0.003	0.015	49.535	50.446	0.001
30	0.024	0.219	52.537	47.200	0.020
45	0.051	0.850	44.260	54.730	0.109
60	0.159	0.327	50.808	48.679	0.027

From the results, it is clear that the sum of the driving force term and friction term accounts for over 99% for all types, while the total contribution of the inertia term, advection term, and diffusion term is less than 1% together. Therefore, the following diffusion wave approximation can be typically used in practice.

$$S_{fx} + \frac{\partial H}{\partial x} = 0 \tag{4.7}$$

$$S_{fy} + \frac{\partial H}{\partial y} = 0 \tag{4.8}$$

After substituting Eq. (4.4) into Eq. (4.7) and Eq. (4.8), the expressions for the components of the velocity vector can be obtained as follows.

$$u = -\frac{h^{2/3}}{n_m\sqrt{|S|}}\nabla_x(H) \quad , \quad v = -\frac{h^{2/3}}{n_m\sqrt{|S|}}\nabla_y(H) \tag{4.9}$$

Finally, Eq. (4.1) can be written as follows, and then it is used to replace shallow water equations in the proposed hybrid coupled model.

$$\frac{\partial h}{\partial t} - \nabla\left(\frac{h^{5/3}}{n_m\sqrt{|S|}}\nabla(H)\right) = R - I \tag{4.10}$$

4.2.2 Governing equations for subsurface flow

The subsurface flow is governed by 3D Richards's equation (see section 3.2.3).

4.2.3 Soil infiltration capacity model

The Green-Ampt model (Green and Ampt, 1911) assumes that the soil infiltration capacity is governed by the soil properties and rainfall conditions. The soil infiltration capacity, f_p, can be approximated as follows.

$$f_p = k_s\left(1 + \frac{\Psi\Delta\theta}{F}\right) \tag{4.11}$$

where, f_p is infiltration capacity (m/s); Ψ is the average suction head at the wetting front (m), and $\Delta\theta$ is the difference between the saturated volumetric water content, θ_s, and the initial volumetric water content, θ_i, ($\Delta\theta=\theta_s-\theta_i$) ($m^3/m^3$). F is the cumulative infiltration (m).

$$F = \int_0^t I dt \tag{4.12}$$

In this study, it is considered that the Green-Ampt model is only used to estimate the infiltration capacity (f_p) during the rainfall infiltration stage and determine when the runoff generate. At the beginning of the simulation, we have a profile with initial moisture content. In this case, the rainfall intensity is usually weak and less than the initial infiltration capacity of the ground surface. All the rainwater will infiltrate into the soil. The initial infiltration capacity is determined by the initial moisture content, and its value is usually very large due to the ground surface is dry. Therefore, the rainfall intensity is used as the flux boundary conditions of the Eq. (3.13). With the infiltration of the rainwater, the Green-Ampt model is running and infiltration capacity will be redistributed each timestep according to Eq. (4.12). If the rainfall intensity exceeds the infiltration capacity of the ground surface. The water is ponding on the ground surface. The infiltration rate will be determined by the pressure head at the surface (zero or higher depending on the increasing runoff h) and the pressure head in the cell below. A part of the not infiltrated water and the exfiltrated water from the underground will then be applied to the runoff simulation as a source item in the next timesteps.

4.2.4 Soil mechanics model (LFS approach)

Lu et al. (2012) proposed the LFS approach to quantify the Factor of Safety of a point based on the current state of stress and the change in the suction (u_a-u_w) caused by rainwater infiltration as shown in Figure 3.2. The stress distribution is calculated by the momentum balance equation.

$$\nabla \cdot (\boldsymbol{\sigma}) + \rho(\theta)\mathbf{b} = 0 \tag{4.13}$$

where, $\boldsymbol{\sigma}$ is the stress tensor (kPa); $\boldsymbol{b}$ is the vector of body forces (m/s^2), $\rho(\theta)$ is the mass density (kg/m^3), which is a function of the volumetric water content, θ. The influence of the suction on the effective stress is evaluated with Bishop's effective stress.

$$\sigma' = (\sigma - u_a) + \chi(u_a - u_w)\ ,\ \chi = \frac{S_e - S_r}{1 - S_r} \tag{4.14}$$

where, σ' is effective stress (kPa); u_a is the pore air pressure (kPa); u_w is the pore water pressure (kPa), and χ is the matrix suction coefficient which varies from 0 to 1 depending on the degree of saturation. S_r is the

residual degree of saturation. Consequently, the local factor of safety (F_{LFS}) at each point within a hillslope is defined as the ratio of the shear strength of soil in the current state (τ) to the shear strength of soil in the saturated state (τ^*). Based on geometric relations as shown in Figure 3.2, F_{LFS} can be calculated by the principal stresses as follows.

$$F_{LFS} = \frac{\tau}{\tau^*} = \frac{CD}{AB} \tag{4.15}$$

$$AB = CF = \frac{\sigma_1' - \sigma_3'}{2} \ , \quad CD = CE \times \sin\phi' = \left(\frac{c'}{\tan\phi'} + \frac{\sigma_1' + \sigma_3'}{2}\right)\sin\phi' \tag{4.16}$$

$$F_{LFS} = \frac{\tau}{\tau^*} = \frac{2 \cdot \cos\phi'}{\sigma_1' - \sigma_3'}\left[c' + \frac{\sigma_1' + \sigma_3'}{2}\tan\phi'\right] \tag{4.17}$$

where, c' is the effective cohesion (kPa); ϕ' is the effective internal friction angle (˚); σ_1' and σ_3' are the maximum and minimum principal stress for the unsaturated soil (kPa).

4.3 Validation of the Iterative Cross-coupled Surface and Subsurface Flow Model

To verify the simulation results of the proposed coupled model, the experimental system is also stimulated by another commercial software, GETFLOWS (GEneral purpose Terrestrial fluid-FLOW Simulator), a finite-difference fluid-flow numerical simulator, to perform quantitative evaluation of the exchange of overland water and groundwater, subsurface seepage and surface water runoff on the hillside slope surface based on an integrated model of fully coupled two-phase surface and subsurface flow (GETFLOWS, 2014). Kitamura et al. (2016) and Malow et al. (2017) validated the applicability of GETFLOWS for simulating the surface flow and subsurface flow process by comparing the simulation results of GETFLOWS and measurements of river water levels in the area of eastern Fukushima Prefecture in Japan and the area of Kourtimalei in Djibouti, respectively. The difference between GETFLOWS and the proposed model in this chapter in terms of theory and governing equations is that GETFLOWS simulate surface and subsurface flows in a fully coupled way by using air and water two-phase flows, and the governing equation of mass conservation is expressed as follows (Mori et al., 2015).

$$\frac{\partial(\varphi S_q)}{\partial t} - \nabla \cdot \left[\frac{k_s \, k_{r,q}}{\rho_q g} \cdot \nabla\left(\Psi_q\right)\right] = q_q \ , \ q = (\text{water}, \text{air}) \tag{4.18}$$

where, subscript q indicates fluid phase, water (w) or air (a); φ is the porosity (m^3/m^3); S_q is fluid saturation of q phase, ($S_w + S_a = 1$); Ψ_q is the potential of q phase (Pa); ρ_q is the density of q phase (kg/m^3); g is gravity acceleration (m/s^2); $k_{r,q}$ is relative hydraulic conductivity of q phase; k_s is saturated hydraulic conductivity (m/s); q_q is the volumetric flux of sink and source of q phase ($m^3/m^3/s$). The nonlinear retention and permeability properties are defined according to van Genuchten (1980).

For both surface and subsurface fluid flows, the integrated model of fully coupled two-phase surface and subsurface flow can be expressed as follows:

$$-\nabla M_q - Q_q = \frac{\partial(\phi S_q)}{\partial t}\ ,\ q = (\text{water}, \text{air}) \tag{4.19}$$

where, M_q is the fluid mass flux of q phase (m/s); Q_q is the volumetric flux of the fluid production and extinction of q phase ($m^3/m^3/s$). The porosity of the surface layer is assumed to 1.0. The water depth is represented by the degree of saturation of the water phase (S_w) and the height of the grid (H_g) in the surface layer ($h=S_w \times H_g$). The terms for surface and subsurface flow can be expressed as follows:

Surface flow:

$$M_w = -\frac{h^{2/3}}{n_m\sqrt{|S|}}\nabla(h+z) \tag{4.20}$$

$$M_a = -\frac{k_s\, k_{r,a}}{\rho_a g}\cdot\nabla(\Psi_a) \tag{4.21}$$

Subsurface flow:

$$M_q = -\frac{k_s\, k_{r,q}}{\rho_q g}\cdot\nabla\left(\Psi_q\right) \tag{4.22}$$

4.3.1 Validation of surface flow model by the extensively used tilted impermeable V-catchment system

Di Giammarco et al. (1996) proposed a tilted impermeable V-catchment system to validate surface flow generated by rainfall events (Figure 4.4). The simplified approximation model of a surface flow is validated by the experimental system. To verify the simulation results of the proposed model in the more general terrain, the tilted V-catchment system is also implemented into another software i.e. GETFLOWS. The system is a V-shaped impermeable catchment with 20 m depth. Two 1000 m × 800 m slopes are connected in the middle to a 1000 m × 20 m channel. Manning's coefficient values are 0.015 $s/m^{1/3}$ for the slope and 0.15 $s/m^{1/3}$ for the channel. The slope of the two slopes is 0.05 perpendiculars to the channel and the slope of the channel is 0.02 parallel to the channel. A rainfall rate of 3×10^{-6} m/s is applied on the whole surface for 90 min with a total time of 180 min. Figure 4.5 shows the results of the GETFLOWS, COMSOL compared with the experiment data referred from Di Giammarco et al. (1996) and other simulation results referred from Tian and Liu (2011) and Kollet and Maxwell (2006). It suggests the results of the simplified approximation model of surface flow simulated by COMSOL agrees well with the experiment data and other simulation results meaning that the simplified approximation model of surface flow can be used to describe the behavior of the surface runoff.

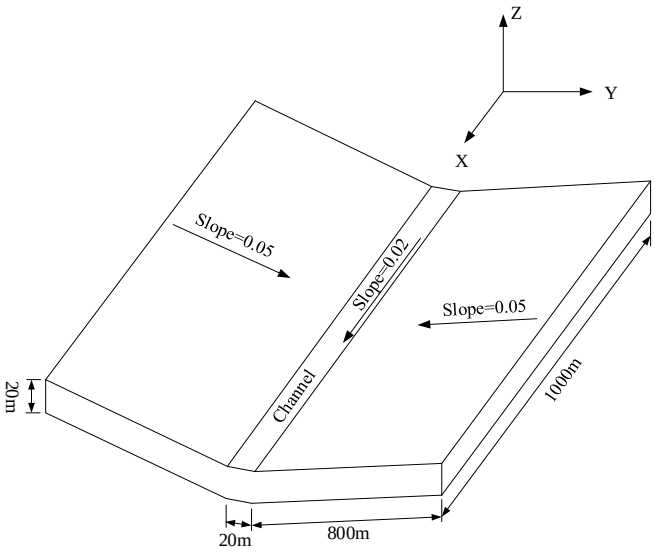

Figure 4.4 Three-dimensional view of the tilted V-catchment area.

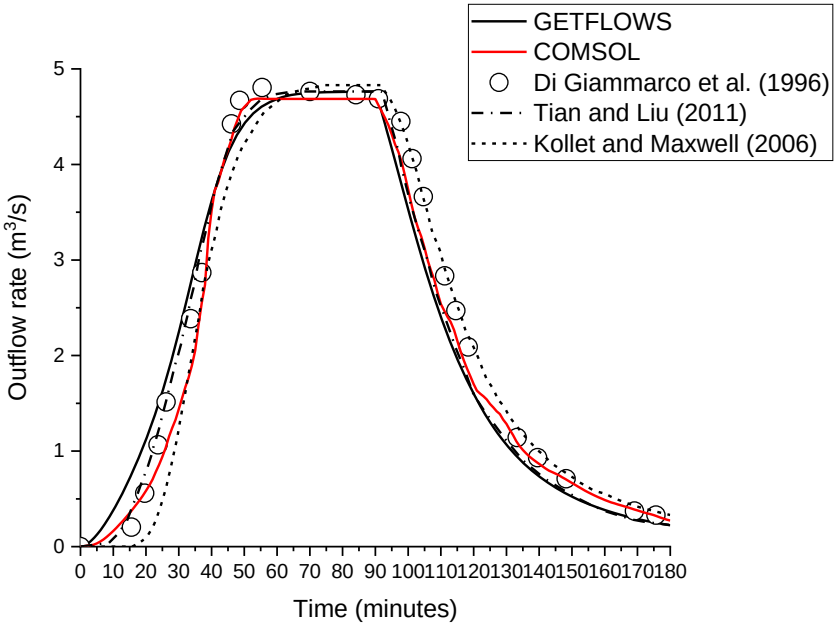

Figure 4.5 Comparison of results of the V-catchment case.

4.3.2 Validation of the iterative cross-coupled surface and subsurface flow model

In this part, the iterative cross-coupled surface and subsurface flow model proposed in Section 4.1 is verified by the experimental system presented by Abdul and Gillham (1984). The experimental system is composed of a 1.4 m × 1.2 m × 0.08 m Plexiglas box filled with medium-fine sand as illustrated in Figure 4.6(a). The free water is drained off at the toe of the slope, and the initial water table is located at the toe of the slope. The soil properties are shown in Figure 4.6(a). A rainfall rate of 43.2 mm/hr is applied on the whole surface domain in the first 20 minutes of a total time of 25 minutes. Figure 4.6(b) and Figure 4.6(c) plot the results calculated by COMSOL and GETFLOWS compared with the results calculated by Cast3M (a finite element code that was

used by Weill et al. (2009) for modeling surface/subsurface flow in a fully integrated way, which is similar to GETFLOWS), and measured data referred from Weill et al. (2009).

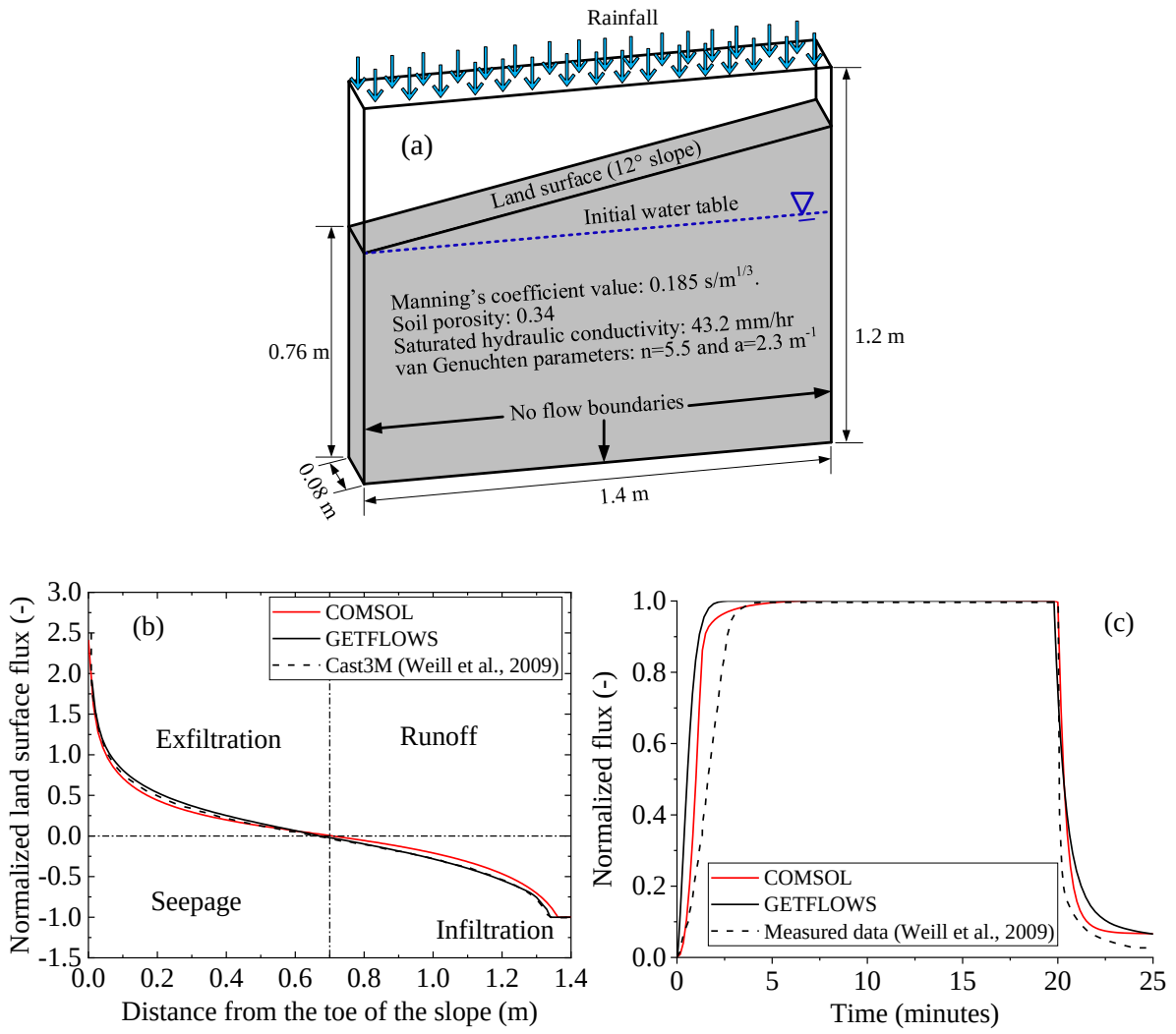

Figure 4.6 (a) Abdul and Gillham system; (b) Comparison of calculated results of normalized flux along the land surface at the 19 minutes after rain; (c) Comparison of calculated results and measured data of normalized flux of discharge at the toe of the slope.

Figure 4.6(b) shows the fluxes along the land surface, and all the fluxes are normalized by the rainfall flux imposed at the land surface (entering fluxes are negative by convention). The results imply that the models implemented in COMSOL and GETFLOWS can describe the three surface regimes (infiltration, runoff, and exfiltration) along the land surface: in a small area at the top of the slope, all rainwater infiltrates into the soil (normalized flux equals -1); in the upper half of the slope, part of the rainwater infiltrates, and the rest flows in the form of runoff on the land surface (normalized flux between -1 and 0); at the lower half of the slope, groundwater exfiltrates to the land surface and flows out with the runoff from the upper part (normalized flux positive). Figure 4.6(c) displays the normalized flux of discharge at the toe of the slope calculated by COMSOL and GETFLOWS compared with the data measured by Weill et al. (2009). It shows that the calculated results

agree well with the measured data, though the simulated time to reach the steady state of overland water and groundwater exchange is shorter than the experimental one. The presence of air could significantly slow down the infiltration process (Weill et al., 2009), and the inconsideration of this effect in the modeling approach could be responsible for that.

4.4 Case Study of Typhoon Induced Embankment Slope Failures

4.4.1 Simulation of surface and subsurface flow for a natural mountain area

The surface flow and subsurface flow analysis at Nissho Pass were performed by the proposed hybrid coupled model. Based on the digital elevation model (DEM) produced from airborne laser scanning (1 m resolution), a 3D model for a natural mountain area for multi slopes instabilities assessment with surface and subsurface flow analysis was built as shown in Figure 3.8(a). The model is composed of three parts: weathered granite, soil, and embankment. Soil properties are listed in Table 3.2. As there are no measurement data at the locations where the slope failures occurred, the simulated results in this chapter are theoretically verified by a physical runoff model (Tank model) proposed by Sugawara et al. (1974), which uses multi-layered tanks to simulate rainwater infiltration and surface runoff. The Tank model has been proved that it is effective for describing the outflow in the watershed (Hong et al., 2015). The calculation of runoff is based on the parameters suggested by Okada (2001) as listed in Figure 4.7. The water storage depth (mm) for each tank is calculated based on the equations below.

$$\frac{dH_1}{dt} = R - I_1 - q_{11} - q_{12} \tag{4.23}$$

$$\frac{dH_2}{dt} = I_1 - q_2 - I_2 \tag{4.24}$$

$$\frac{dH_3}{dt} = I_2 - q_3 - I_3 \tag{4.25}$$

The outflow rate from each outlet of the model and infiltration rate from the upper tank to the lower tank are calculated based on the equations below.

$$q_{11} = \begin{cases} \alpha_{11} \times (H_1 - L_{11}) & , \text{if } H_1 > L_{11} \\ 0 & , \text{if } H_1 \le L_{11} \end{cases} \tag{4.26}$$

$$q_{12} = \begin{cases} \alpha_{12} \times (H_1 - L_{12}) & , \text{if } H_1 > L_{12} \\ 0 & , \text{if } H_1 \le L_{12} \end{cases} \tag{4.27}$$

$$q_2 = \begin{cases} \alpha_2 \times (H_2 - L_2) & , \text{if } H_2 > L_2 \\ 0 & , \text{if } H_2 \le L_2 \end{cases} \tag{4.28}$$

$$q_3 = \begin{cases} \alpha_3 \times (H_3 - L_3) & , \text{if } H_3 > L_3 \\ 0 & , \text{if } H_3 \le L_3 \end{cases} \tag{4.29}$$

$$I_1 = \beta_1 \times H_1, \quad I_2 = \beta_2 \times H_2, \quad I_3 = \beta_3 \times H_3 \tag{4.30}$$

The total outflow rate of the basin is represented as follows.

$$Q = (q_{11} + q_{12} + q_2 + q_3) \times A \tag{4.31}$$

where, I_1, I_2, and I_3 are the infiltration rate from the upper tank to the lower tank (mm/h); q_{11}, q_{12}, q_2, and q_3 are the outflow rate of each outlet (mm/h) for each outlet of sidewall; L_{11}, L_{12}, L_2, and L_3 represent the height of each outlet (mm); H_1, H_2, and H_3 are the water storage depth in each layer (mm); α_{11}, α_{12}, α_2, and α_3 are the outflow coefficient for each outlet (1/h); β_1, β_2, and β_3 are the coefficients of permeability from the bottom hole of each tank (1/h); Q is total of outflow rate of the basin (m^3/s), and A is the area of the basin (km^2).

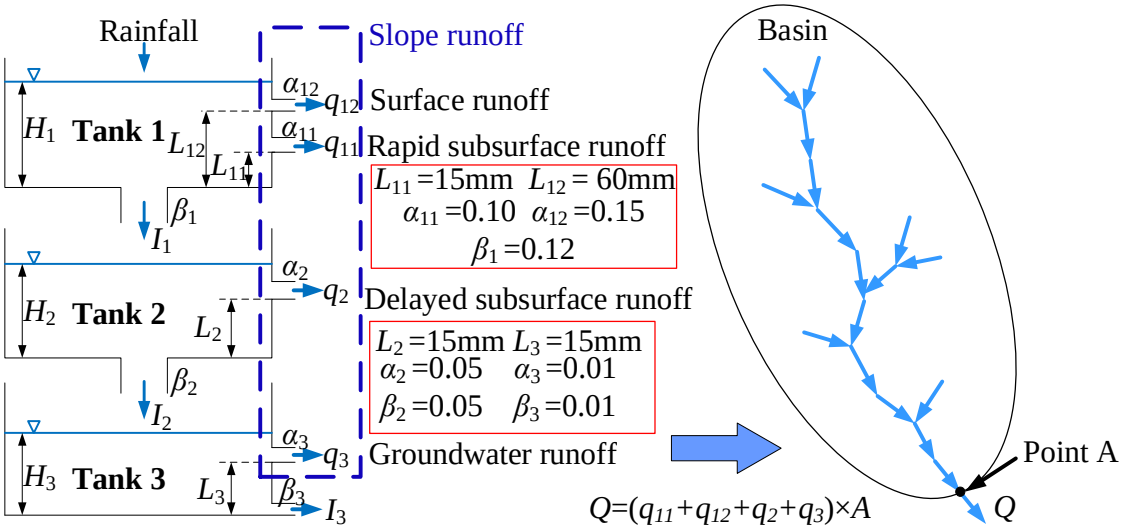

Figure 4.7 Schematic diagram of the three-layer Tank model.

Figure 4.8(a) displays the distribution of water depth and the vector of flow velocity calculated by COMSOL. From Figure 4.8(a), It can be seen that a large amount of water from the upstream is gathered at Location 1 and Location 2, which allows more water to infiltrate into the embankment. The outflow rates of the catchment area at Location 1 (Point A in in Figure 4.7, located at the exit of the gully to avoid the calculation errors caused by the water coming from Location 2 along the road, which can be identified from Figure 1.3(a) and Figure 4.8(a)) calculated by the Tank model, COMSOL, GETFLOWS, and iRIC (a 2D impermeable plane flow simulation software (iRIC, 2015)) are shown in Figure 4.8(b). From Figure 4.8(b), it is recognized that the generation of runoff calculated by the Tank model, COMSOL, and GETFLOWS starts from 22 hours after the rainfall event happens. However, due to the non-consideration of infiltration, the runoff simulated by iRIC is generated when the rainfall event happens, and the outflow rate calculated by iRIC is larger than that calculated by the other approaches at Location 1. On the other hand, the Tank model assumes that the slope runoff flows out of the catchment area according to a certain percentage of water storage depth in each tank. Accordingly, the Tank model does not consider the impact of slope angle, which causes the outflow rate calculated by the Tank model is smaller at the peak value, and larger at the end of the rainfall event than that calculated by COMSOL and GETFLOWS. Figure 4.8(c) plots the surface water depth located at the road center (where water comes from the upstream catchment and road) at Location 1 and Location 2. To discuss the two-stage process of rainwater infiltration, a representative point on the hillside slope (a point located in

the gully upstream of Location 1) is selected to display the relationship between the infiltration rate and rainfall intensity on the hillside slope as shown in Figure 4.8(d). The results shown in Figure 4.8(d) suggest that at the beginning of a rainfall event, the infiltration rate is equal to the rainfall intensity (all rainwater infiltrates into the soil). From Figure 4.8(c), it is recognized that the simulated runoff is generated from 22 hours after the rainfall event happens, which is consistent with the results shown in Figure 4.8(b). Nearly at the same time, rainfall intensity exceeds the infiltration capacity (f_p) of the ground surface in Figure 4.8(d). After rainfall intensity exceeds the infiltration capacity (f_p), i.e. the runoff is generated, the infiltration rate is no longer equal to rainfall intensity. At this time, the infiltration rate is governed by the surface water depth. Furthermore, the surface water depth (Figure 4.8(c)) and infiltration rate (Figure 4.8(d)) calculated by GETFLOWS agree well with the results calculated by COMSOL at both Location 1 and Location 2, meaning that the two software can be mutually verified and the coupled surface and subsurface flow model is more reliable than Tank model and surface flow model (iRIC).

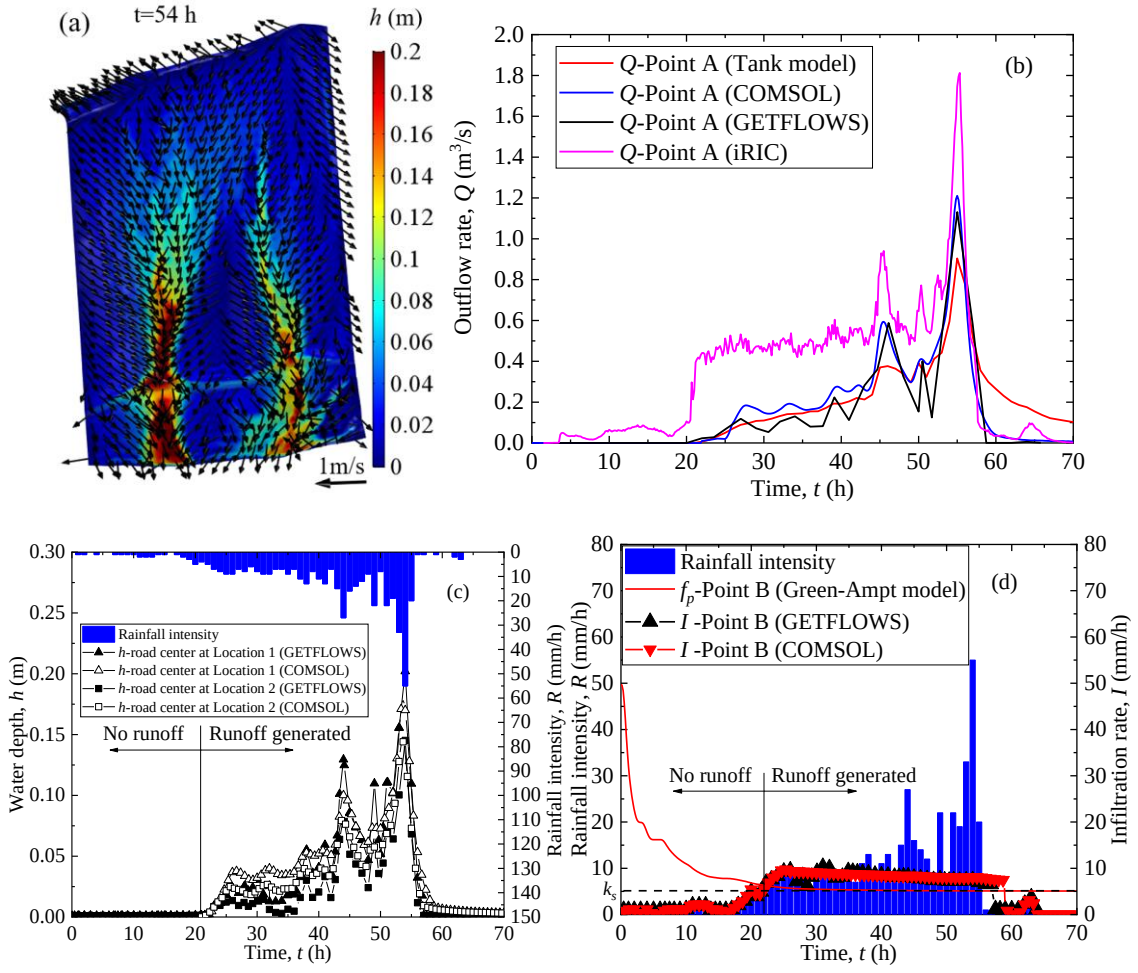

Figure 4.8 (a) Distribution of water depth and the vector of flow velocity calculated by COMSOL; (b) Comparison of outflow rate (Q) calculated by each approach; (c) Surface water depth (h) at Location 1 and Location 2; (d) Infiltration capacity (f_p) and infiltration rate (I).

4.4.2 Multi slopes instabilities assessment along the highway

To investigate the effect of runoff and subsurface flow on the slope stability during Typhoon No. 10, the instabilities of two slopes (the embankment slope located at Location 1 and Location 2) were analyzed simultaneously by using the 3D soil mechanics model adopting the LFS approach. If the instabilities of the two slopes can be captured simultaneously, it indicates that the 3D soil mechanics model adopting the LFS approach will also able to analyze the instabilities of multi slopes (more than two slopes) simultaneously in a wide area. By incorporating the body load (volumetric water content) and pore water pressure (u_w) calculated by the coupled surface and subsurface flow model into the soil mechanics model, two cases are studied, i.e. multi slopes instabilities analysis with considering runoff and without. Figure 4.9 shows the distribution of the local factor of safety (F_{LFS}) in the two cases. From Figure 4.9(b), it is recognized that with considering runoff, the slope failure occurred (F_{LFS} < 1.0) at Location 1 and Location 2 is successfully reproduced. Conversely, without considering runoff, slope failure only occurred in a very small area at Location 1 as shown in Figure 4.9(a). Figure 4.10 shows the distributed pore water pressure (u_w) and local factor of safety (F_{LFS}) at Location 1 and Location 2 under the two study cases (with considering runoff and without). From Figure 4.10, it can be seen that the presence of runoff leads to a more significant increase in pore water pressure. The negative pore water pressure increases to zero or even becomes positive pore water pressure in the surface layer of the soil, which causes the occurrence of the slope failure.

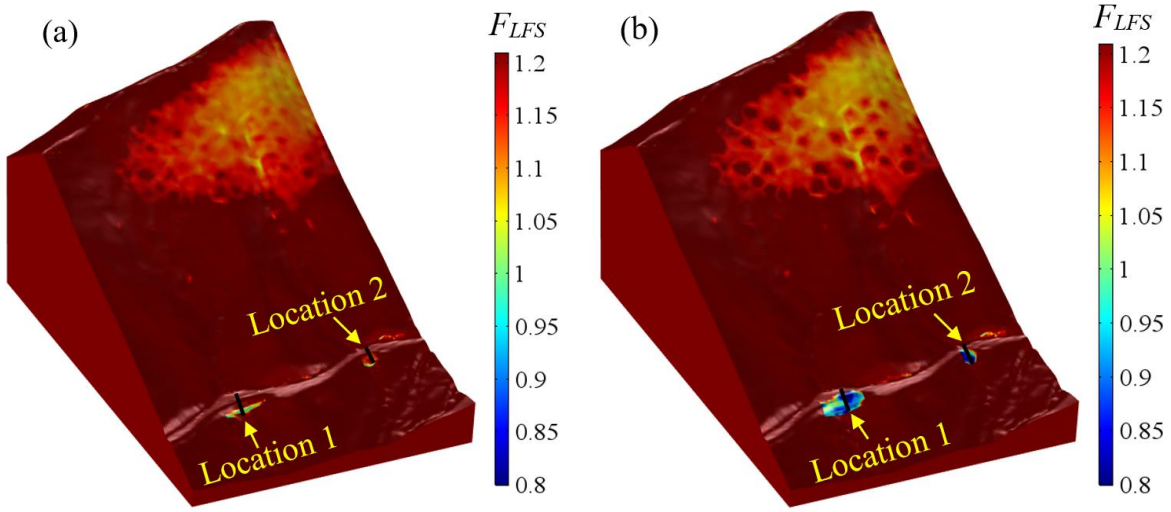

Figure 4.9 Catchment-scale range multi slopes stability maps during Typhoon No. 10 (a) without considering runoff; (b) with considering runoff.

From Figure 4.10(b), it can be seen that the simulated shape of the slope failure (red line in Figure 4.10(b)) is similar to while slightly shallower than the actual shape of the slope failure (blue line in Figure 4.10(b)) at Location 1 and Location 2. The main reason is that in the actual process of slope failure, the collapsed part moved downstream, and runoff water further eroded the newly exposed soil and caused further damage to the

embankment. Therefore, it implies that runoff has significant effects on the embankment slope failures especially at the exit of the gully. On the other hand, by using the LFS approach, multi slopes instabilities analysis can be performed on a catchment-scale range, which has significant advantages as compared with other methods to analyze the stability of a single slope. Moreover, as the stability map of multi slopes conduces to determine the dangerous spots in the target region, this has significant implications for precisely determining the dangerous spots (instead of areas) on a catchment-scale range and accurately releasing warning information to the dangerous spots. For example, in Japan, the disaster warning information is released to a 5 km × 5 km area according to the national early warning system. Based on the early warning system, the occurrence time of slope failures can be roughly estimated, while it is difficult to determine the specific number and location of slope failures. Therefore, expanding the size of the coupled model proposed in this chapter to 5 km × 5 km, and combining the numerical simulation results with the prediction results of the early warning system, warning information will be accurately released to the dangerous spots instead of areas.

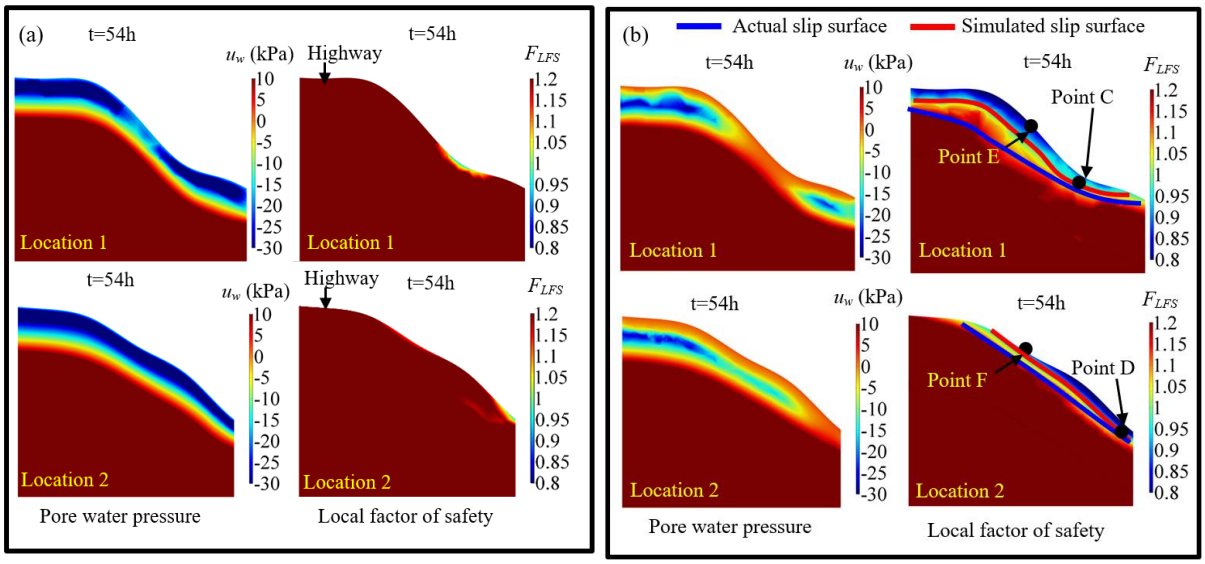

Figure 4.10 Distribution of pore water pressure (u_w) and local factor of safety (F_{LFS}) (a) without considering runoff; (b) with considering runoff.

To further analyze the effect of runoff on slope stability, Figure 4.11(a) to Figure 4.11(c) illustrate the time-dependent effective degree of saturation (S_e), u_w, and F_{LFS} at Location 1 and Location 2 (Point C and Point D in Figure 4.10(b), located near the ultimate slip surface as shown by the red lines in Figure 4.10(b)). It is recognized that the infiltrated rainwater causes the increase of the S_e as shown in Figure 4.11(a), which causes an increase in the u_w as shown in Figure 4.11(b), thereby causing the decrease in the suction of unsaturated soil, and eventually decreases the F_{LFS} as shown in Figure 4.11(c). It is worth noting that the increase of S_e and u_w, and the decrease of F_{LFS} are more significant when the runoff is considered. After runoff is generated, S_e and u_w have a steep increase and F_{LFS} sharp declines, meaning that the runoff from upstream allows more water to infiltrate into the embankment, thereby causing more significant decrease in the suction of the embankment

and the possibility of embankment slope failure at the exit of the gully to be much greater than other locations along the highway.

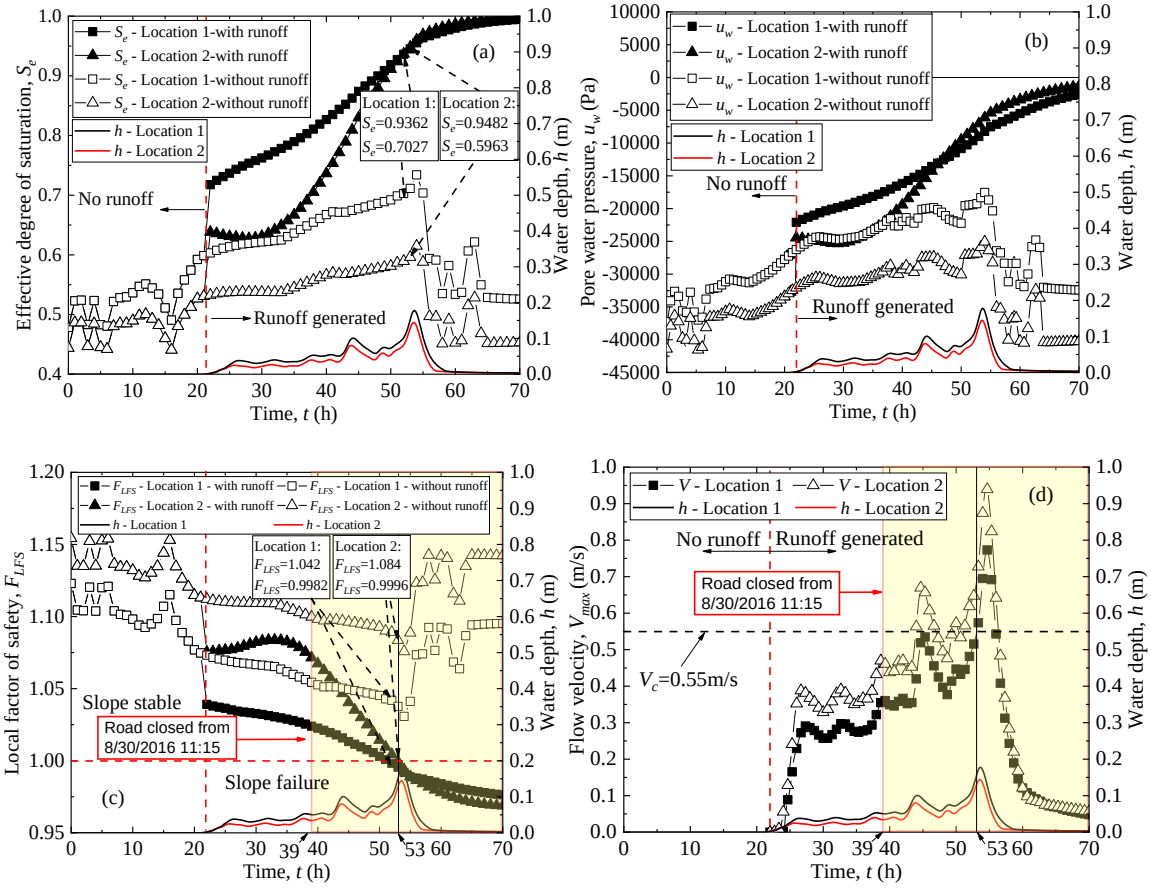

Figure 4.11 Time-dependent effective degree of saturation (S_e), pore water pressure (u_w), local factor of safety (F_{LFS}), and flow velocity (V) at Location 1 and Location 2. (a) S_e vs. time; (b) u_w vs. time; (c) F_{LFS} vs. time; (d) V vs. time.

On the other hand, the excessive high-velocity runoff could carry debris larger than sand and erode exposed surfaces, thereby increasing the permeability of the slope surface, which could also allow more water to infiltrate into the embankment and eventually triggers slope failure. Therefore, the runoff is a key factor causing the embankment slope failures, and its effects cannot be neglected. Erosion might occur on the slope surface when the flow velocity exceeds a critical value, called critical erosional velocity (Blais and McGinn, 2011). The critical erosional velocity is 0.55 m/s at Location 1 and Location 2, which is calculated by the critical erosion velocity estimation model (V_c=0.33$D_{50}^{0.47}$) proposed by Bogardi (1978). V_c is the critical erosion velocity measured in m/s. D_{50} represents the median diameter of the sediment material in mm, and its value is 3.0 mm for the embankment at Nissho Pass (Kawamura and Miura, 2018). To discuss the effects of the runoff on the erosion of the embankment slope surface, Figure 4.11(d) shows the flow velocity (V) on the embankment slope at Location 1 and Location 2 (Point E and Point F in Figure 4.10(b), located on the embankment slope surface). In Figure 4.11(d), it can be identified that the flow velocity exceeds the critical

erosion velocity, V_c (0.55 m/s), and even close to 1.0 m/s at peak both at Location 1 and Location 2. Therefore, it can be considered as the excessive high-velocity runoff and could cause severe erosion of the embankment slope. Moreover, from Figure 4.11(c) and Figure 4.11(d), it is recognized that the F_{LFS} becomes less than 1.0 and the flow velocity exceeds V_c at 00:00 on August 31st, 2016 after the road was closed from 11:15 on August 30th, 2016. It means that the simulation results are reliable. However, the runoff induced erosion of the embankment slope is not considered in the numerical simulation of this chapter. The discussion in the effects of runoff on the erosion of the embankment slope surface and the influences of the erosion on the slope instability is an addition in this study.

4.5 Summary of This Chapter

High-velocity runoff generated in hillslopes during heavy rainfall caused by typhoon increases the instability of the embankment slope at the exit of the gully. Such effects of high-velocity runoff are usually neglected in conventional rainfall-induced slope failure analysis. To consider the effects of runoff on the slope instability, this chapter attempts to simulate the runoff, infiltration, seepage, and slope instabilities on a small catchment-scale simultaneously. For this purpose, a hybrid coupled model of surface flow, subsurface flow, and soil mechanics was firstly proposed in this chapter based on shallow water equations, Richards's equation, Green-Ampt infiltration capacity model, and the local factor of safety (LFS) approach. Next, to make the proposed coupled model effective in the practical analysis of runoff, a diffusion wave approximation of shallow water equations is validated by numerical simulations, and then it is used to replace shallow water equations in the proposed coupled model. Finally, the proposed coupled model is verified by Abdul and Gillham system and applied to a natural slope in Hokkaido, Japan. The numerical results highlight the influences of runoff from upstream on the embankment slope failure at the exit of the gully. Furthermore, the small catchment-scale slope instabilities assessment approach proposed in this chapter provides an effective approach for simulating heavy rainfall-induced runoff and slope instabilities. The distribution map of the factor of safety (FOS) has significant implications for precisely determining the dangerous spots (instead of areas) on a small catchment-scale and accurately releasing the warning information to these dangerous spots.

The research findings in this chapter indicate that the catchment-scale multi-slope instabilities assessment approach proposed in this chapter provides an effective way for simulating heavy rainfall-induced runoff and multi-slope instabilities in the target region, and it has significant implications for precisely determining the dangerous spots (instead of areas) on a catchment-scale and accurately releasing warning information to the dangerous spots. However, due to the limitation of the LFS approach, the exact timing of the slope occurrence is difficult to determine. Therefore, further and more theoretical or numerical studies are recommended to improve the LFS approach and incorporate the runoff into the existing Japanese early warning system.

5 PREDICTION OF RAINFALL AND SNOWMELT INDUCED SLOPE FAILURE ON THE REGIONAL-SCALE

On the regional-scale, in 2005, the Japanese government launched a new nationwide early warning system for predicting debris flow and slope failure disasters within each 5 km square grid covering entire Japan based on rainfall intensity and Soil Water Index (SWI). However, the Japanese government has not set early warning criteria in many mountain areas. Besides, the existing early warning criteria are much higher than realistic ones in some areas, and snowmelt water has not been considered during the calculation of SWI. These cause many slope failures in seasonally cold regions, which were induced by rainfall and/or snowmelt, have not been predicted. Therefore, in this chapter, the hourly snowmelt water is firstly incorporated into the Japanese early warning system more accurately by using the meteorological monitoring data and the snow density estimated by a newly proposed combination model. Next, based on case studies and parametric analyses for slope stability assessment, new early warning criteria are proposed for predicting three different patterns of slope failures under two typical types of precipitation (rainfall and snowmelt) conditions. Finally, a new determination method for setting the early warning criterion in seasonally cold regions is proposed by referring to the existing early warning criteria near the target area, in accordance with the precipitation types and the local ground condition of the slope. Since the existing early warning criteria near the target area already have taken the influences of the variation in the local geology and geography into account, the new determination method for early warning criterion can be applied to the arbitrary area in seasonally cold regions without directly considering the local soil properties, in the actual design and maintenance works.

5.1 Soil Water Index for Seasonally Cold Regions

5.1.1 Soil Water Index (SWI) incorporating snowmelt water

After considering the snowmelt water with rainfall as water supply to the model, the water storage in each tank and SWI are represented as shown in Figure 5.1(a),

$$\frac{dH_1}{dt} = R + SM - I_1 - q_{11} - q_{12} \tag{5.1}$$

$$\frac{dH_2}{dt} = I_1 - q_2 - I_2 \tag{5.2}$$

$$\frac{dH_3}{dt} = I_2 - q_3 - I_3 \tag{5.3}$$

$$SWI = H_1 + H_2 + H_3 \tag{5.4}$$

where, *SM* is the amount of hourly snowmelt water (mm/h). To predict the occurrence of debris flows and slope failures, the Japanese government set a CL for the relationship between 60-minute cumulative rainfall and SWI in a 5 km square grid, i.e., when the Snake Line (hereafter, SL, indicating the relationship between

60-min rainfall and SWI) exceeds CL, debris flows and slope failures could occur as shown in Figure 5.1(b). However, the current Japanese early warning system does not take snowmelt water into account, resulting in the inaccurate calculation of SWI during the snow-melting season. Therefore, it is indispensable to consider the hourly snowmelt water into the calculation of SWI during the snow-melting season.

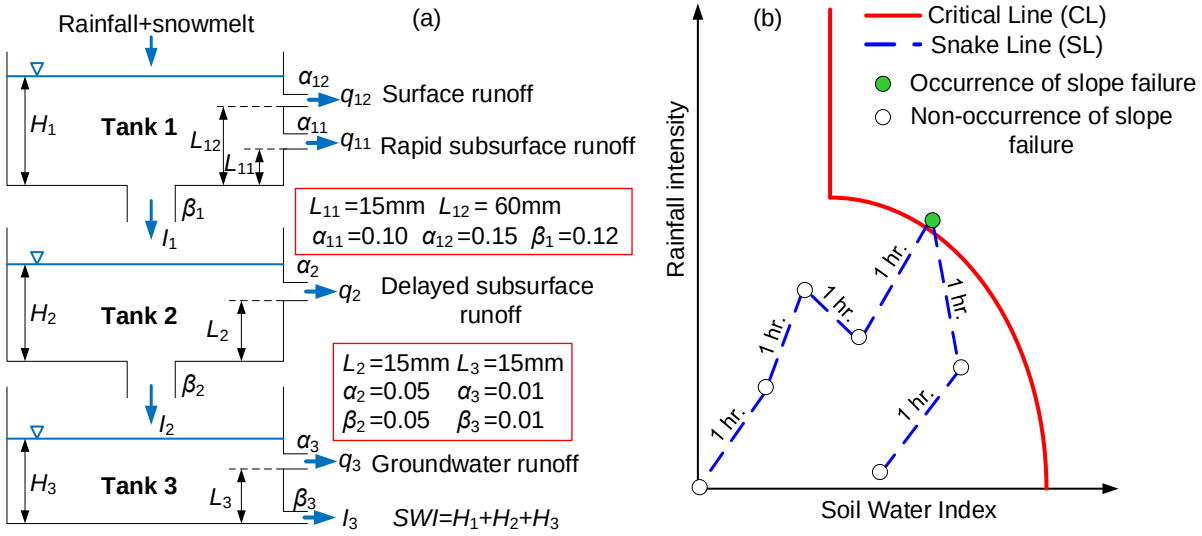

Figure 5.1 (a) Three-layer Tank model for calculating Soil Water Index (adapted from Okada, 2001); (b) Prediction of the occurrence of slope failure based on CL and SL.

5.1.2 Estimation of hourly snowmelt water

Two basic approaches are commonly used to estimate the amount of snowmelt water, one of which is based on the meteorological monitoring data, i.e., monitored snow depth and snowfall. Since the hourly amount of snowmelt water directly corresponds to the monitored snow depth and snowfall resulting in it has high accuracy, Siva Subramanian et al. (2018) estimated the hourly snowmelt water by using this approach. However, they did not consider the change in snow density during the estimation process. Therefore, for more precise predictions, this study takes into account the change of snow density in the estimation of hourly snowmelt water. The amount of hourly snowmelt water can be estimated according to the following relationship (Kazama et al., 2008).

$$SM = \Delta SWE - SF \tag{5.5}$$

where, SWE is snow water equivalent (mm), ΔSWE is the hourly change of snow water equivalent (mm/h), SF is snowfall (mm/hr.).

The below relationship allows for the conversion of snow depth to SWE by given snow density (ρ_n) (Mizukami and Perica, 2008; Sturm et al., 2010).

$$\mathrm{SWE} = h_s \frac{\rho_n}{\rho_w} \tag{5.6}$$

where, h_s is snow depth (m), ρ_n is snow density (kg/m^3), ρ_w is the density of liquid water (approximately 1000 kg/m^3 at 0 ˚C). If there is no available snow depth measurement data, the snow depth can be estimated by snow accumulation models. The models often use average air temperature to determine the fraction of precipitation falling as rain or snow (Anderson, 1976; Anderson, 2006). The threshold value of air temperature to differentiate rainfall and snowfall is 2 °C (Ikebuchi et al., 1986). Snowmelt is assumed to only occur when the average air temperature is greater than 0 °C with the existence of snowpack on the ground (Kazama et al., 2008). The snowfall is calculated based on the amount of precipitation and air temperature according to the following relationship (Anderson, 2006).

$$SF = P \times f_s \times SCF \tag{5.7}$$

where, P indicates precipitation (mm/hr.), f_s indicates snow fraction, and SCF (snow correction factor) is an average value over all of the accumulation periods. The value of SCF can be set as 1 (He et al., 2011). The snow fraction, f_s is 1 when the average hourly air temperature is less than or equal to 2 °C, while f_s is 0 when the average hourly air temperature is larger than 2 °C.

On the other hand, as the measurement of snow depth and estimation of snow density is very complicated, Kurahashi et al. (2017) hypothesize that air temperature is a major driving force in snowmelt processes and the snowmelt water is a function of air temperature.

$$SM = KT_a \tag{5.8}$$

where, K is the degree-hour factor (mm/˚C/hr.), T_a is the average air temperature (˚C). Grounded in the fact that snowmelt is directly estimated from the amount of accumulated depth of snow, the estimation of snowmelt water derived from meteorological monitoring data and modeled snow density (snow density is estimated from a snow density model that considers snow depth, snow aging, etc.) usually has higher accuracy than it estimated by degree-hour factor and air temperature. Therefore, this study incorporates hourly snowmelt water into the Japanese early warning system by using meteorological monitoring data and modeled snow density.

5.2 Estimation of Snow Density

5.2.1 Field monitoring data of snow density in northern Japan

The snow density is influenced by snowmelt water, snow depth, snow aging (older snow is denser than younger snow), and meteorological variables like air temperature, wind speed, and solar radiation, etc. (Sturm et al., 2010). For example, the densification of an underlying snow layer proceeds with time and depth due to compaction by mechanical loading of the overlying snow. As a result, snow density increases with time (Kojima, 1967; McCreight and Small, 2014). The typical seasonal snow density ranges from 30 to 600 kg/m^3 (Motoya et al., 2017). According to the field monitoring data (monitoring period: February 20th ~ March 10th in 2012, 2014, 2016 and 2017) of snow depth and SWE in Hokkaido, Japan referenced from Arakawa (2012),

Shirakawa et al. (2014), Shirakawa (2016) and Shirakawa (2017), the snow density at the beginning of March throughout Hokkaido is about 300 kg/m^3, as shown in Figure 5.2(a).

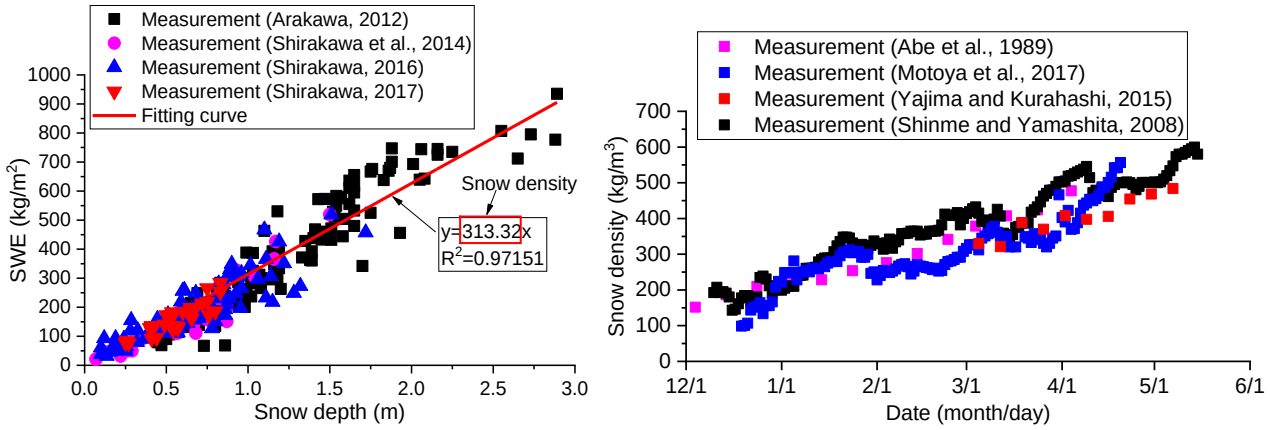

Figure 5.2 (a) Field monitoring data of snow depth and SWE in Hokkaido, Japan; (b) Field monitoring data of snow density in northern Japan.

Furthermore, Abe et al. (1989) measured the snow depth, SWE, and snow density in Shinjo City, Japan for 15 years (from 1973/74 to 1987/88 winter seasons). Motoya et al. (2017) measured the snow density around Akita prefecture, Japan from December 20th, 2011 to April 22nd, 2012. Shinme and Yamashita (2008) measured the snow density from December 10th, 2006 to May 10th, 2007, and Yajima and Kurahashi (2015) measured the snow density from March 5th, 2015 to May 14th, 2015 in the Jozankei area, Hokkaido, Japan, respectively. Figure 5.2(b) illustrates the results of the measured density of snow cover vs. time referred from Abe et al. (1989), Shinme and Yamashita (2008), Motoya et al. (2017), and Yajima and Kurahashi (2015) for the chosen area. From Figure 5.2(b), it is recognized that in northern Japan, the snow density is about 150 kg/m^3 in the first part of winter (December-January), and increases to 300 kg/m^3 in the middle (February-March), then reaches to about 600 kg/m^3 in the last part of winter (April-May).

5.2.2 Existing models

Existing models (named by the authors' initials and the year of publication) that estimate snow density are reviewed as follows. Sturm et al. (2010) developed a nonlinear approach to estimate a corresponding snow density by the observed snow depth (abbreviated as S10 model). In the model, snow density is a function of snow depth (h_s), day of year (DOY), and four general fitting parameters (k_1, k_2, ρ_0, and ρ_{max}) for each of five broad snow classes as given in Table 5.1.

$$\rho_{h,\mathrm{DOY}} = (\rho_{\max} - \rho_0)[1 - \exp(-k_1 \times h_s - k_2 \times \mathrm{DOY})] + \rho_0 \tag{5.9}$$

where, $\rho_{h,\mathrm{DOY}}$ indicates snow density (kg/m^3) related to snow depth and DOY (DOY is a number from -92 (1st October) to +181 (30th June) and DOY is 1 on 1st January), ρ_{max} is maximum snow density (kg/m^3), ρ_0 is initial

snow density (kg/m^3), k_1 (1/m) and k_2 are densification parameters for depth and DOY, respectively, and h_s indicates the snow depth (m).

Table 5.1 Model parameters by snow class (Sturm et al., 2010).

Snow class	ρ_{max} (kg/m^3)	ρ_0 (kg/m^3)	k_1 (1/m)	k_2
Tundra	363.0	242.5	0.0029	0.0049
Maritime	597.9	257.8	0.0010	0.0038
Prairie	594.0	233.2	0.0016	0.0031
Alpine	597.5	223.7	0.0012	0.0038
Taiga	217.0	217.0	0.0000	0.0000

Meloysund et al. (2007) reported that in an informative annex to ISO 4355 'Bases for design of structures – Determination of snow loads on roofs', the method derived from the former USSR is proposed that snow density can be represented by the following expression (abbreviated as USSR model),

$$\rho_n = (90 + 130\sqrt{h_s})(1.5 + 0.17 \times \sqrt[3]{T_a})(1 + 0.1\sqrt{v_w}) \tag{5.10}$$

In Japan, Endo (1986) fitted the following relationship between snow density and date based on the monitoring data of snow density from 1964 to 1979 in Sapporo, Hokkaido, Japan (abbreviated as E86 model).

$$\rho_n = 239 + 0.861 \times t_1 + 0.01 \times t_1^2 \tag{5.11}$$

Shinme and Yamashita (2008) proposed that the snow density is a linear equation of snow depth and time based on the monitoring data of snow depth and snow density from 2006 to 2007 in the Jozankei area, Hokkaido (abbreviated as SY08 model).

$$\rho_n = 15.77 \times h_s + 0.11 \times t_2 + 128.1 \tag{5.12}$$

where, v_w is the wind velocity (m/s), t_1 denotes DOY and t_2 is time in hours measured from the lying snow exist. Apart from this, many studies (e.g., Tomomura et al., 1982; Abe and Shimizu, 2004) have proposed a variety of different models for estimating snow density based on snow depth or snow aging. The existing models are summarized in Table 5.2.

Table 5.2 Summary of existing snow density estimation models.

Model name	Formula	Reference
S10 model	$\rho_{h,\mathrm{DOY}} = (\rho_{\max} - \rho_0)[1 - \exp(-k_1 \times h_s - k_2 \times \mathrm{DOY})] + \rho_0$	Sturm et al., 2010
USSR model	$\rho_n = (90 + 130\sqrt{h_s})(1.5 + 0.17 \times$	Meloysund et al., 2007

	$\sqrt[3]{T})(1+0.1\sqrt{v})$	
SY08 model	$\rho_n = 15.77 \times h_s + 0.11 \times t_2 + 128.1$	Shinme and Yamashita, 2008
E86 model	$\rho_n = 239 + 0.861 \times t_1 + 0.01 \times t_1^2$	Endo, 1986
T82 model	$\rho_n = 2 \times t_1 + 150$	Tomomura et al., 1982
AS04 model	$\rho_n = 109 \times \sqrt{h_s} + 177$	Abe and Shimizu, 2004

Note: t_1 denotes DOY and t_2 is time in hours measured from the lying snow exist.

For discussing the suitability and applicability of the above mentioned existing models in Hokkaido, Japan, the change of snow density in the Jozankei area, Hokkaido is calculated by the existing models from December 10th, 2006 to May 15th, 2007, and then compared with the measured values of snow density measured by Shinme and Yamashita (2008) as shown in Figure 5.3(a) and Figure 5.3(b).

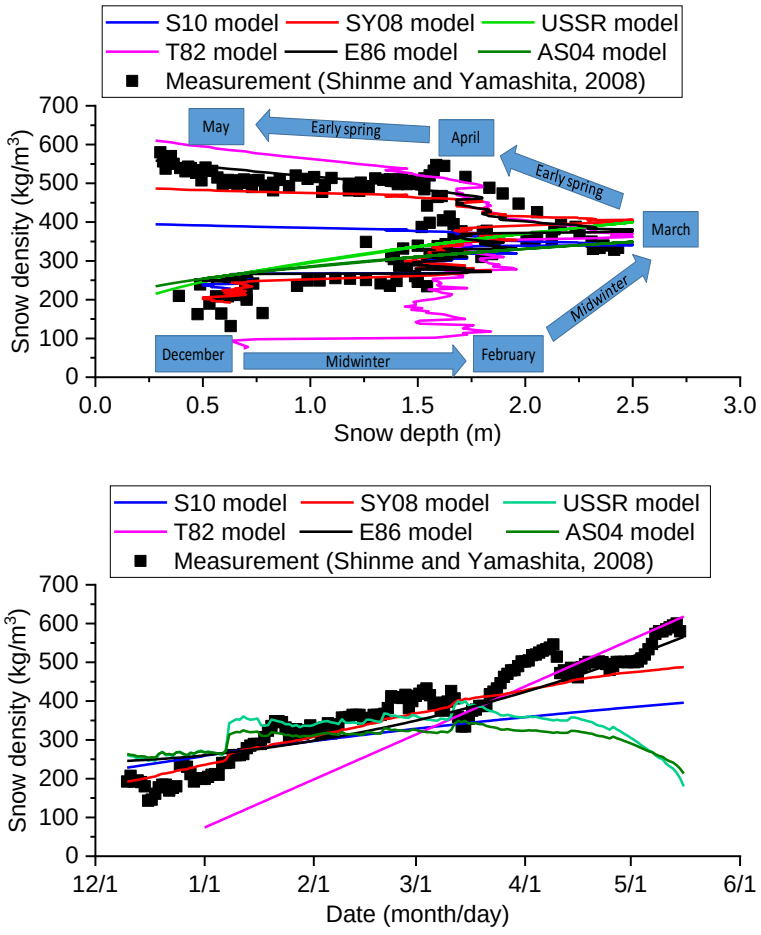

Figure 5.3 (a) Snow density vs. snow depth estimated by the existing models and field monitoring data (calculation and measurement period: 12/10/2006-05/15/2007); (b) Snow density vs. time estimated by the existing models and field monitoring data (calculation and measurement period: 12/10/2006-05/15/2007).

From Figure 5.3(a) and Figure 5.3(b), it is recognized that as the AS04 model and USSR model only use snow depth as the variable, they could only describe the change of snow density with snow depth between December and March, while the change of snow density with snow aging between March and May cannot be captured. Besides, as the T82 model and E86 model only use cumulative time after snow accumulating on the ground as the variable, they could only describe the change of snow density with snow aging between March and May, while the impact of snow depth on the snow density between December and March is not considered. On the other hand, although the S10 model and SY08 model can consider the influences of both snow depth and snow aging, it is recognized that the snow densities estimated by these two models are smaller than the measurement values between April and May. It suggests that all of these models cannot be singly used to accurately estimate the snow density between December and May in Hokkaido, Japan. Therefore, this study combines the SY08 model and E86 model to propose a combination model, named SY08-E86, that could estimate snow density more accurately in Hokkaido, Japan.

5.2.3 Combination model

Mizukami and Perica (2008) separated time series in two periods: midwinter (1st December-1st March) and early spring (1st March-30th April) by comparing interannual variations of densification rates in four distinct regions (i.e. coastal region, continental region, high elevation region, and the region between coastal and continental). They found that the increasing snow depth and snow aging are the key factors influencing the snow density during the midwinter period (1st December-1st March) because the densification of snowpack derived from the pressure due to the overburden snow is the primary mechanism for snow density increasing. On the other hand, during the early spring period (1st March-30th April), snow depth steadily declines to zero due to the decreasing frequency of snowfall and an increasing amount of snowmelt. However, snowmelt water causes faster destructive metamorphism and finally increases snow density. Referring to the above study, as the SY08 model has higher precision during the midwinter period and E86 have higher precision during the early spring period as shown in Figure 5.3(b), by combining the advantages of these two models, an SY08-E86 combination model is newly proposed for a precise calculation of snow density in Hokkaido, Japan.

(1) During the midwinter period (SY08 model):

$$\rho_n = 15.77 \times h_s + 0.11 \times t_2 + 128.1 \tag{5.12}$$

(2) During the early spring period (E86 model):

$$\rho_n = 239 + 0.861 \times t_1 + 0.01 \times t_1^2 \tag{5.11}$$

The snow density calculated by the newly proposed combination model is shown in Figure 5.4. It is recognized that the combination model has a more robust estimation of snow density. Therefore, this study proposes to use the newly proposed combination model for estimating the snow density.

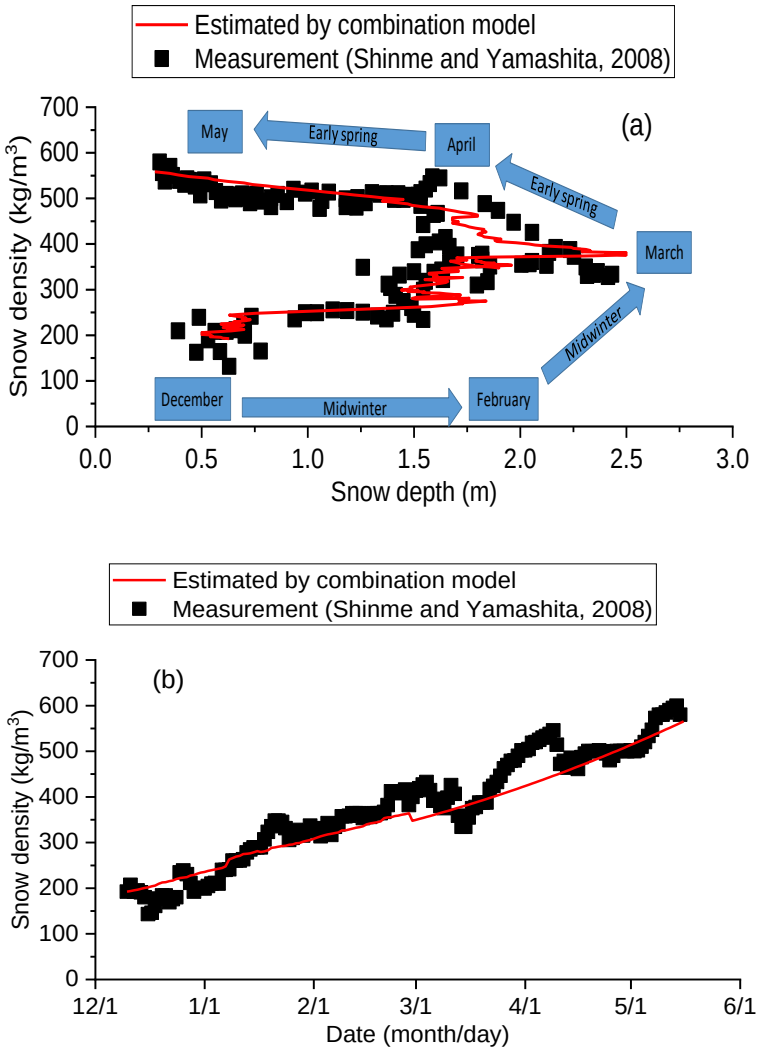

Figure 5.4 Snow density estimated by the combination model and field monitoring data (a) snow density vs. snow depth and (b) snow density vs. time.

5.3 Prediction Method for Rainfall and/or Snowmelt Induced Slope Failures with SWI

5.3.1 Applicability of SWI incorporating snowmelt water

This section examines the applicability of the Soil Water Index (SWI) incorporating snowmelt water, which is calculated using the snow density estimated by the newly proposed combination model. By using meteorological monitoring data and modeled snow density, the amount of hourly snowmelt water is calculated for Nakayama Pass during two long-term periods: from November 8th, 2011 to May 5th, 2012, and from November 8th, 2012 to April 8th, 2013. After integrating hourly snowmelt water into the calculation of SWI, the snake lines (SLs) from the day before the occurrence to the day after the occurrence of the Nakayama Pass slope failure are plotted in Figure 5.5 and Figure 5.6.

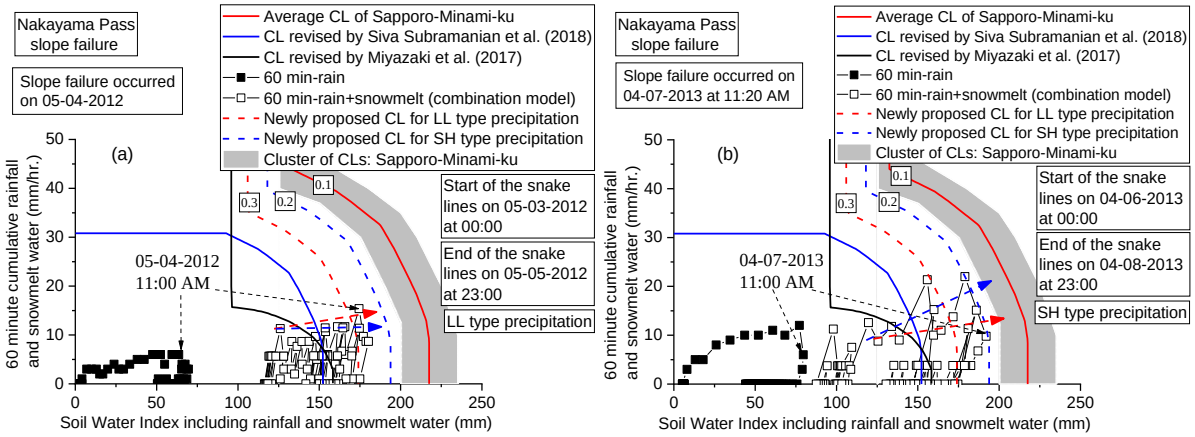

Figure 5.5 Soil Water Index calculated by the combination model in the calculation period: (a) 05/03/2012-05/05/2012 and (b) 04/06/2013-04/08/2013.

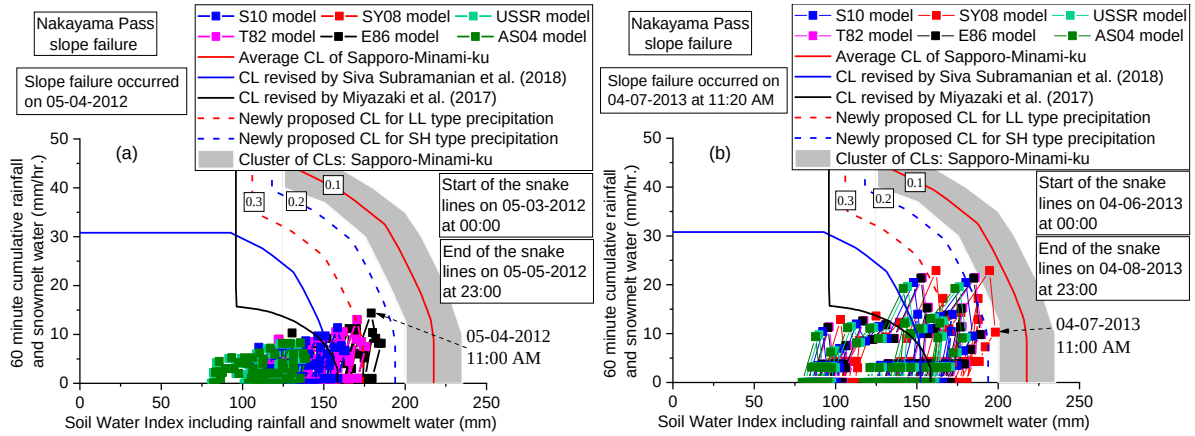

Figure 5.6 Soil Water Index calculated by the other existing models in the calculation period: (a) 05/03/2012-05/05/2012 and (b) 04/06/2013-04/08/2013.

Figure 5.5 shows the SLs without considering snowmelt water (the line with black points) and with the consideration of snowmelt water estimated by the combination model (the line with white points). From Figure 5.5, it is recognized that the starting points of the SLs with considering snowmelt water are much larger than that without the consideration of snowmelt water, meaning that snowmelt water significantly increased the SWI during the long-term period before the occurrence of the slope failure. Figure 5.6 shows the SLs with considering snowmelt water estimated by the existing models. Since there is a significant difference in the estimated snow density of each existing model during the snow-melting season (March-May) as shown in Figure 5.3, the SWI calculated by each existing model has a significant difference as shown in Figure 5.5. As discussed in the previous chapter, the combination model has higher precision in the estimation of snow density. Therefore, the SWI calculated by the combination model is more effective than the existing models. It is noted that the slope failures occurred at Nakayama Pass located in the grid without setting a CL as shown in Figure 5.7(a). Therefore, the applicability of a cluster of CLs, defined as a collection of all CLs (blue curves) set in a

5 km square grid (blue grid) in Sapporo-Minami-ku by the Hokkaido government for the target area is discussed. However, it is worth noting that even if SWI is calculated using hourly rainfall and snowmelt water, the maximum point of SL (near slope failure time) has not yet exceeded the lower boundary for the cluster of CLs in Sapporo-Minami-ku, when the slope failure occurred either on May 4th, 2012 or on April 7th, 2013 at Nakayama Pass.

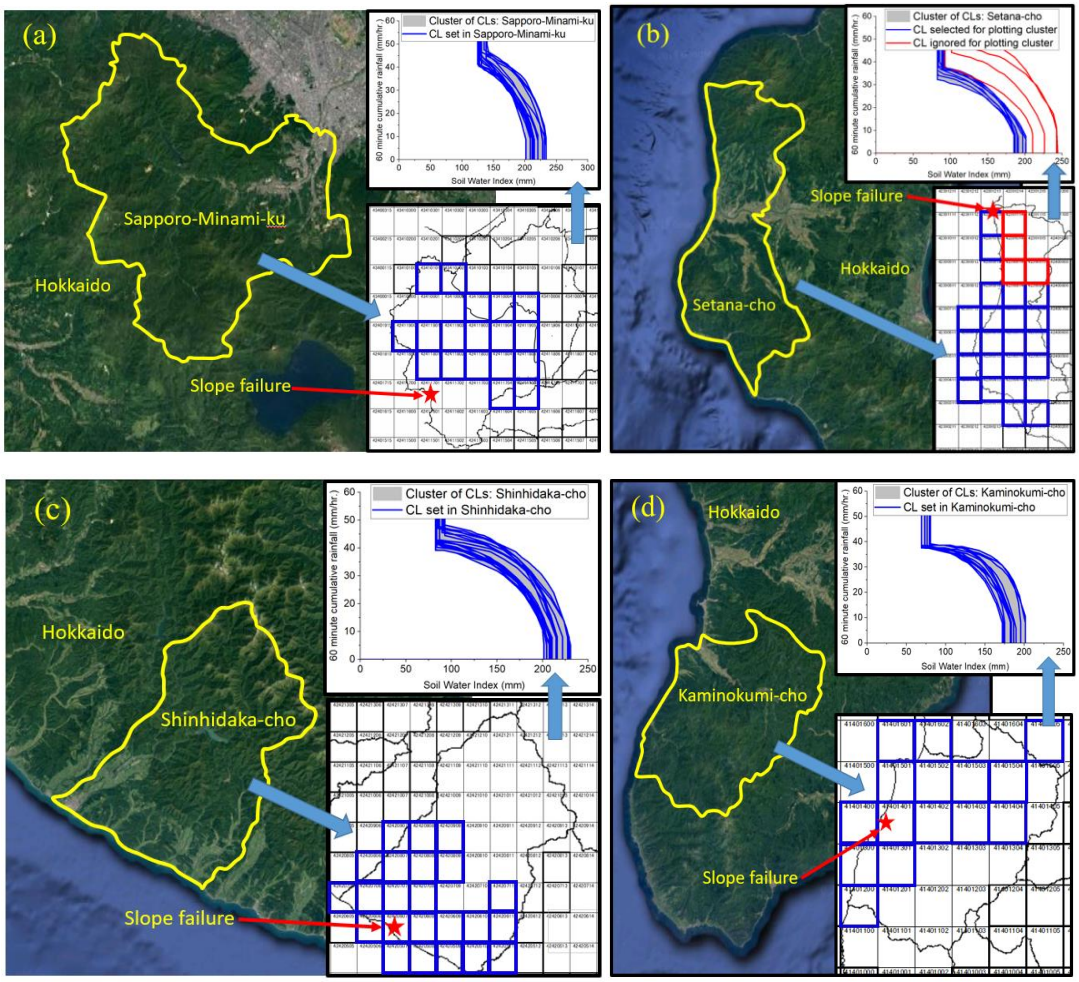

Figure 5.7 Cluster of CLs in the local region (a) Sapporo-Minami-ku; (b) Setana-cho; (c) Shinhidaka-cho and (d) Kaminokumi-cho.

Moreover, even if adopting other calculation methods, the estimated SL does not reach the lower boundary for the cluster of CLs, regardless of the estimation model of the snow density. It implies that the existing CLs (cluster of CLs) are not applicable and not realistic for the prediction of rainfall and/or snowmelt induced soil slope failures at Nakayama Pass. Due to these facts, Miyazaki et al. (2017) proposed a new CL (black line in Figure 5.5 and Figure 5.6) for predicting rainfall and/or snowmelt induced slope failures at Nakayama Pass. However, the earlier proposed CLs are found too conservative for predicting the rainfall and/or snowmelt induced slope failures. In consideration of the above, it is indispensable to propose a new CL for predicting rainfall and/or snowmelt induced slope failures at Nakayama Pass.

5.3.2 Early warning criterion proposed by the slope stability assessment approach

Freeze-thaw actions and rainfall and/or snowmelt water infiltration have a significant effect on the water content fluctuation of the soil slopes (Ishikawa et al., 2015). Accordingly, Siva Subramanian et al. (2017) proposed a slope stability assessment approach to simulate the long-term fluctuation of the water content and factor of safety for volcanic soil slope subjected to freeze-thaw actions and rainfall and/or snowmelt water infiltration.

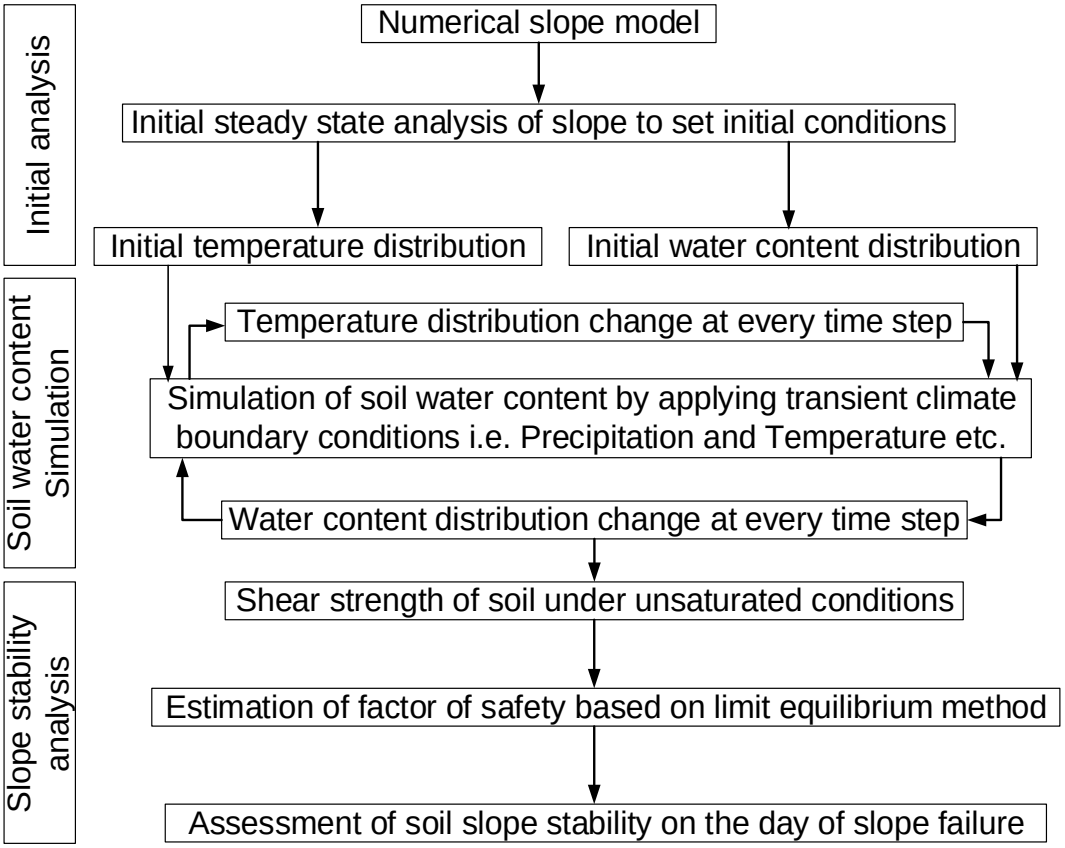

Figure 5.8 Slope stability assessment approach (adapted from Siva Subramanian et al., 2017).

The approach consists of three parts, i.e., initial analysis, soil water content simulation, and slope stability analysis as shown in Figure 5.8. The soil water content simulation includes two calculation conditions: long-term soil water content simulation (the days before slope failure) and short-term soil water content simulation (on the day of slope failure). To predict rainfall and/or snowmelt induced slope failures, Siva Subramanian et al. (2018) proposed a new CL (blue line in Figure 5.5 and Figure 5.6) for the entire Hokkaido based on this approach. However, as they just used the properties of volcanic soil that is widely distributed in Hokkaido instead of the local soil properties for the numerical simulations, and they also did not consider the difference in CL due to the different local geology and geography in different areas, the accuracy of the new CL proposed by Siva Subramanian et al. (2018) is not high at Nakayama Pass as shown in Figure 5.5 and Figure 5.6. Therefore, to propose a new early warning criterion for more accurately predicting rainfall and/or snowmelt

induced slope failures, this section attempts to improve the determination method for setting the CL based on the slope stability assessment approach proposed by Siva Subramanian et al. (2017). In this section, slope failures occurred along Nakayama Pass and Nissho Pass in Hokkaido, Japan are taken as typical examples for checking the appropriateness and validity of the improved determination method. A two-dimensional numerical model for non-isothermal coupled transient seepage analysis (see Figure 5.9) was built to simulate the long-term fluctuation of the water content and factor of safety of soil slope subjected to freeze-thaw actions and rainfall and/or snowmelt water infiltration. During the initial analysis and soil water content simulation, the climate boundary (air temperature, precipitation, humidity, and wind speed) was applied on the slope surface (ab, bc, and cd in Figure 5.9). The adiabatic boundary, displacement constraint boundary, and no flow boundary were set at the right side (de), the bottom side (ef) and lift side (af) of the model as shown in Figure 5.9.

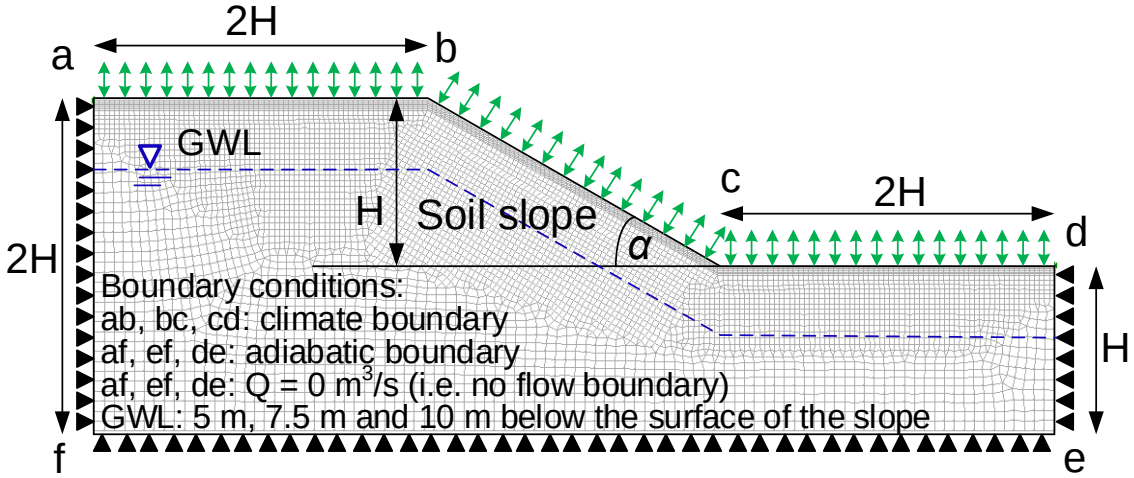

Figure 5.9 Two-dimensional numerical model with applied boundary conditions and FEM mesh.

The simulation period of initial analysis and long-term soil water content simulation is from November 8th, 2012 to April 6th, 2013 with a time step of 1 day, and the simulation period of short-term soil water content simulation and slope stability analysis are from 00:00 to 24:00 on April 7th, 2013 with a time step of 1 hour. For discussing the influence of soil properties on the new CL, the soil properties of Nakayama Pass and Nissho Pass were used as listed in Table 5.3. The parameters, i.e., dry density (ρ_s), porosity (φ), saturated hydraulic conductivity (k_s), effective cohesion (c'), and effective internal friction angle (ϕ') were obtained from laboratory element tests (Sato et al., 2017; Fukutsu and Kawamura, 2016). The parameters for which no laboratory measurements are available, i.e., thermal conductivity (λ), volumetric heat capacity (ζ), and residual volumetric water content (θ_r), were estimated based on the grain size curve of soil (SoilVision, 2018). The numerical simulations were performed with different initial Ground Water Levels (GWL, 5 m, 7.5 m and 10 m below the slope surface), different slope angles (30˚, 35˚, 40˚ and 45˚), and different slope heights (5 m, 10 m, 15 m and 20 m) to reflect various in situ conditions of natural embankment slopes.

Table 5.3 Soil properties used in the numerical simulations for Nakayama Pass and Nissho Pass.

Property name	Nakayama Pass	Nissho Pass
Dry density, ρ_s (kg/m^3)	1423	1695
Porosity, φ	0.47	0.36
Saturated hydraulic conductivity, k_s (m/s)	5.62×10^{-7}	1.12×10^{-5}
Residual volumetric water content, θ_r (m^3/m^3)	0.05	0.035
Saturated volumetric water content, θ_s (m^3/m^3)	0.47	0.36
Unfrozen thermal conductivity of saturated soil, λ_u (kJ/(Day·m·°C))	127	107.8
Frozen thermal conductivity of saturated soil, λ_f (kJ/(Day·m·°C))	132.2	171.7
Unfrozen volumetric heat capacity, ζ_u (kJ/(m^3·°C))	2237.7	3372
Frozen volumetric heat capacity, ζ_f (kJ/(m^3·°C))	1624.2	1193
Effective cohesion, c' (kPa)	0	0
Effective internal friction angle, ϕ' (°)	35	37

By the way, Saito et al. (2010) examined rainfall intensity and duration conditions of 1,174 shallow landslides that occurred during 2006-2008 and found that rainfall for shallow landslide initiation in Japan is objectively classifiable into two typical types: short-duration high-intensity (SH) type and long-duration low-intensity (LL) type precipitation. Chen et al. (2017) highlighted that the SH type precipitation is associated with a rapid increase in SWI, and the LL type precipitation is associated with a gradual rise of SWI. For example, in Figure 5.5, the precipitation type is determined by the relationship between the general overall trend of snake line (blue dash arrow) and threshold line (red dash arrow with a slope of 0.04 proposed by Saito et al. (2010)). From Figure 5.5, it can be seen that the SLs during the snow-melting season include SH type precipitation and LL type precipitation. The main difference between the LL type and the SH type precipitation is the slope of the SL. This is because LL type precipitation during the snow-melting season is caused by the slow snowmelt, whereas SH type precipitation is caused by the rapid snowmelt as seen in the meteorological monitoring data of these two years. Therefore, in this study, two types of rainfall conditions are assumed: SH type (30 mm/hr. for 6 hours) and LL type (10 mm/hr. for 24 hours). The snowmelt rate is assumed to be a sinusoidal function with a peak of 4 mm/hr. (slow snowmelt rate) and 15 mm/hr. (rapid snowmelt rate) at noon as listed in Table

5.4. Accordingly, fifteen combination conditions of precipitation (rainfall and snowmelt) were adopted as summarized in Table 5.5.

Table 5.4 Five types of rainfall conditions and three snowmelt rates used in the numerical simulations.

Name	Rainfall intensity (mm/hr.)	Duration	Type
LL	10	24 hours	Continuous
SH1	30	6 hours (00:00~06:00)	Continuous
SH2	30	6 hours (06:00~12:00)	Continuous
SH3	30	6 hours (12:00~18:00)	Continuous
SH4	30	6 hours (18:00~24:00)	Continuous
Name	Snowmelt rate (mm/hr.)	Duration	Type
SM1	0	24 hours	Continuous
SM2	0 ~ 4	24 hours	Sinusoidal (Max. at 12:00)
SM3	0 ~ 15	24 hours	Sinusoidal (Max. at 12:00)

Table 5.5 Combination of rainfall and snowmelt conditions.

Combination condition		Snowmelt rate		
		SM1	SM2	SM3
Rainfall	SH1	SH1+SM1	SH1+SM2	SH1+SM3
	SH2	SH2+SM1	SH2+SM2	SH2+SM3
	SH3	SH3+SM1	SH3+SM2	SH3+SM3
	SH4	SH4+SM1	SH4+SM2	SH4+SM3
	LL	LL+SM1	LL+SM2	LL+SM3

A total of 720 numerical models were simulated for both Nakayama Pass and Nissho Pass. Based on the results of the numerical simulations, the numbers of slope failures at each analytical condition are summarized in Figure 5.10. By analyzing the results, it is found that in the case of the same GWL and slope height, more

slope failures happened with the larger slope angle, and in the case of the same GWL and slope angle, the large slope height increases the potential instability of the soil slope. These are because the shear force is primarily related to slope angle and slope height. Additionally, with the rise of GWL, the reduced suction causes a drop in shear strength and, thus, the slope stability becomes unstable. For example, in the case of Nakayama Pass, for the gentle slope (30˚and 35˚), no slope failures occur when GWL is low due to high suction, while the slope stability is greatly affected by the slope height under high GWL conditions. For steep slopes (40˚ and 45˚), since the slope stability is originally very low, and slight changes in shear strength or shear stress may cause a slope failure, both GWL and slope height have strong impacts on the slope stability.

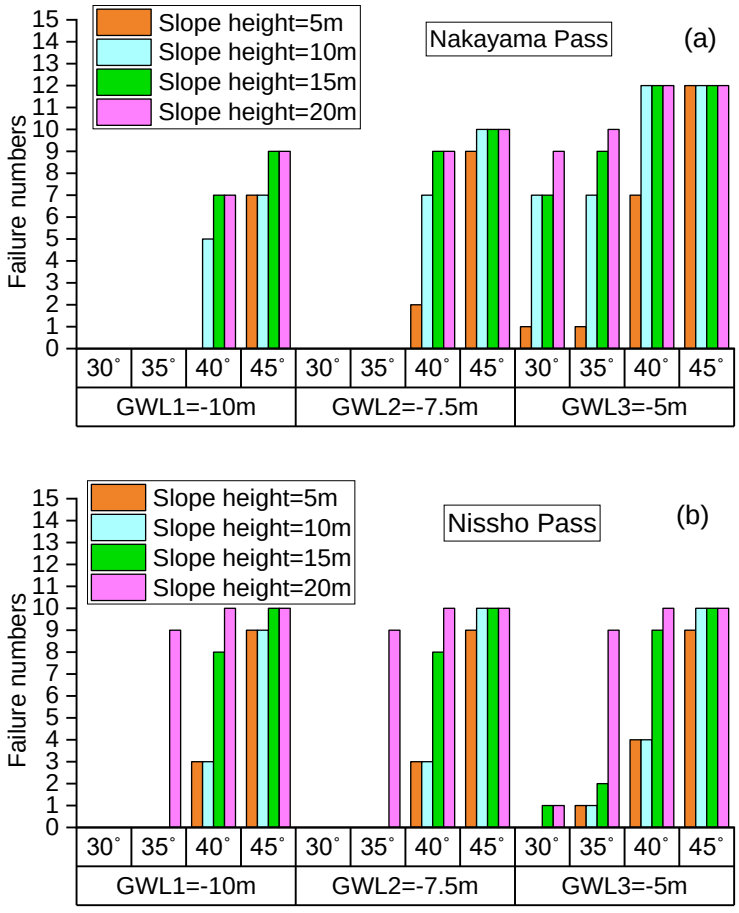

Figure 5.10 Results of failure numbers for (a) Nakayama Pass and (b) Nissho Pass.

Furthermore, the SLs corresponding to stable cases and slope failure cases for Nakayama Pass and Nissho Pass are plotted in Figure 5.11. It is noted that the average CL for the cluster of CLs is set as the RBFN 0.1 to determine the RBFN value of the new early warning criterion based on the RBFN method (Kuramoto et al., 2001). In Figure 5.11, the white points indicate the SLs for the numerical stable cases, while the black points indicate that for the numerical slope failure cases (the first points with the factor of safety less than 1.0). The margin between stable cases and failure cases can be regarded as the new CL. From Figure 5.11, it is recognized that there is a difference in the location of the margin caused by the difference in the strength parameters of a

soil slope in numerical models. Accordingly, when setting the new CL in different areas, the difference in local geology and geography should be considered.

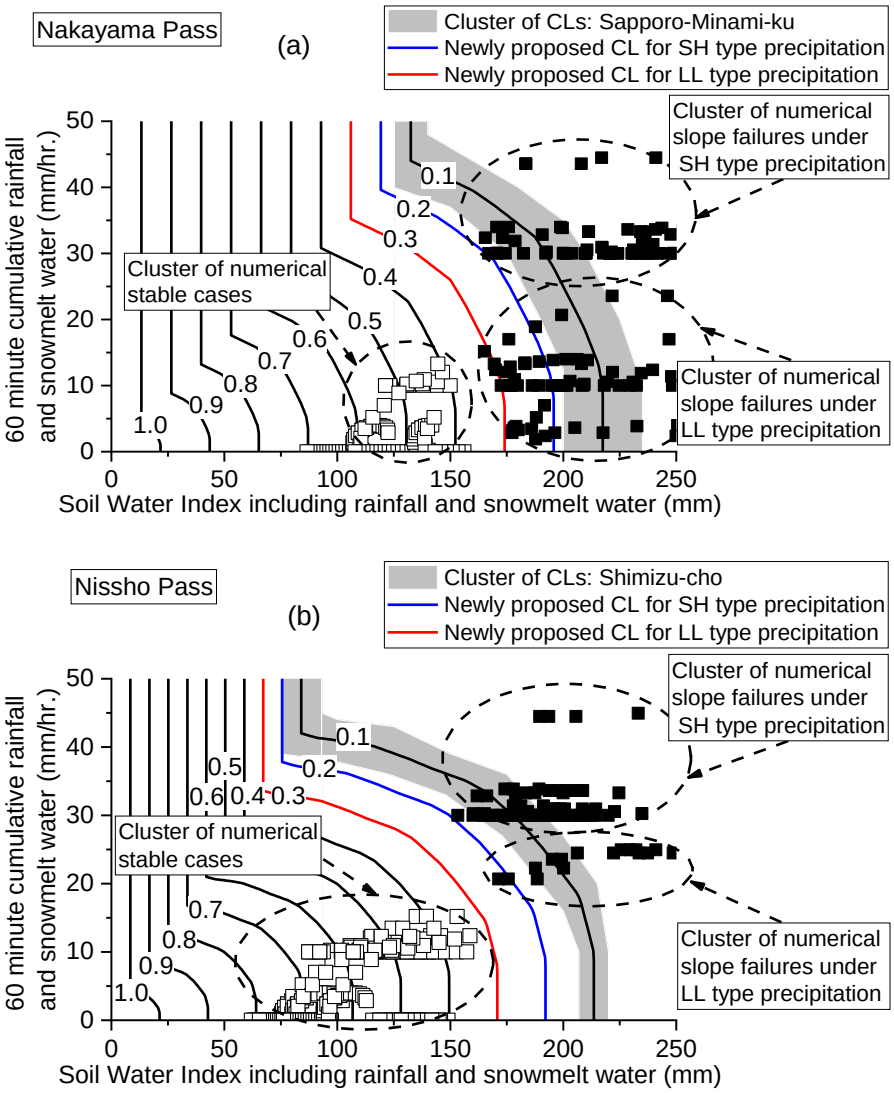

Figure 5.11 Possible revisions of new CLs based on numerical simulation results for (a) Nakayama Pass and (b) Nissho Pass.

On the other hand, in Figure 5.11, the RBFN values of the new CLs determined by the slope stability assessment approach are the same, even though the soil properties are different between Nakayama Pass and Nissho Pass. For example, the CLs for SH type and LL type precipitation are RBFN 0.2 and RBFN 0.3, respectively, for both areas. This is because the difference in the location of RBFN 0.1 curves obtained from the cluster of CLs has already considered the variation of the local geology and geography. Besides, the newly proposed CLs for SH type (blue dash line) and LL type (red dash line) precipitation at Nakayama Pass are depicted in Figure 5.5. It is recognized that the newly proposed CLs are applicable for precisely predicting SH type and LL type precipitation induced slope failures at Nakayama Pass and that the new CLs proposed in this chapter are more reasonable compared with the CLs proposed by the past researches (black line and blue line

in Figure 5.5). These results indicate that as existing early warning criteria near the target area already have taken the influences of the variation in the local geology and geography into account, the new CL determined by the slope stability assessment approach and the average CL for the cluster of CLs can be adopted as a more rational early warning criterion for the local area, in accordance with the precipitation types and the local ground condition of the slope, regardless of soil properties. The applicability of the new CLs proposed for Nakayama Pass is checked with the consideration of rainfall history, i.e., the SL is calculated from April 1st, 2002 as shown in Figure. 5.12. It can be seen that during a long period (about 10 years), the new CLs proposed for Nakayama Pass show a very good stability and reliability.

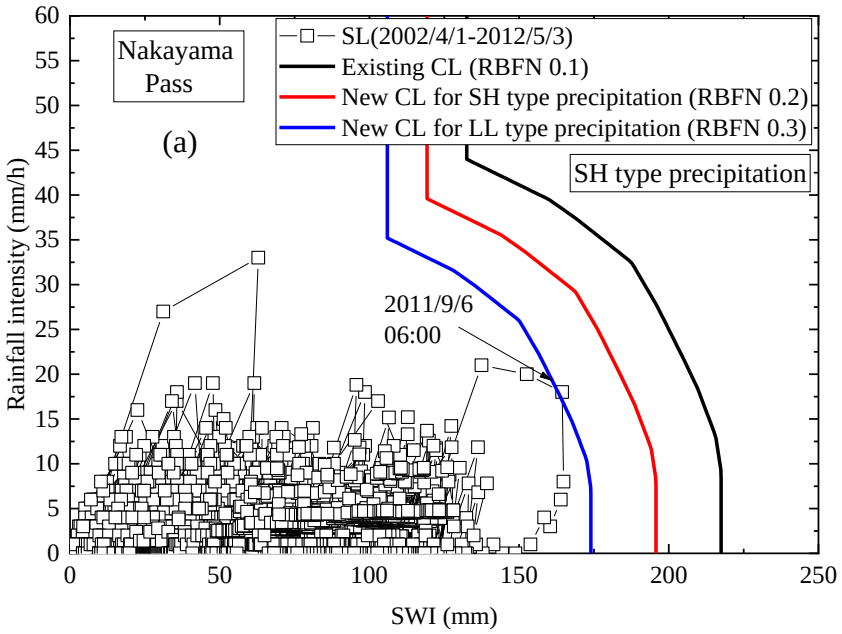

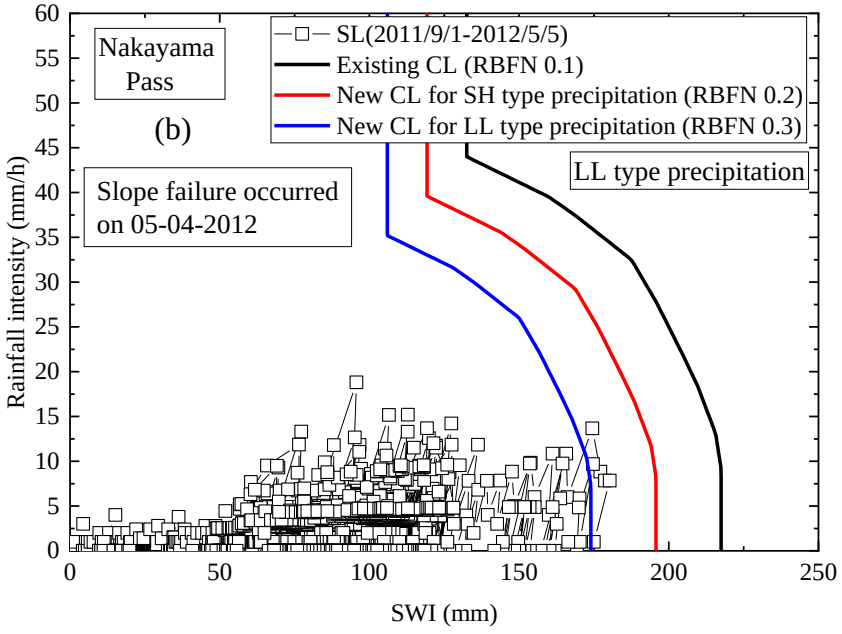

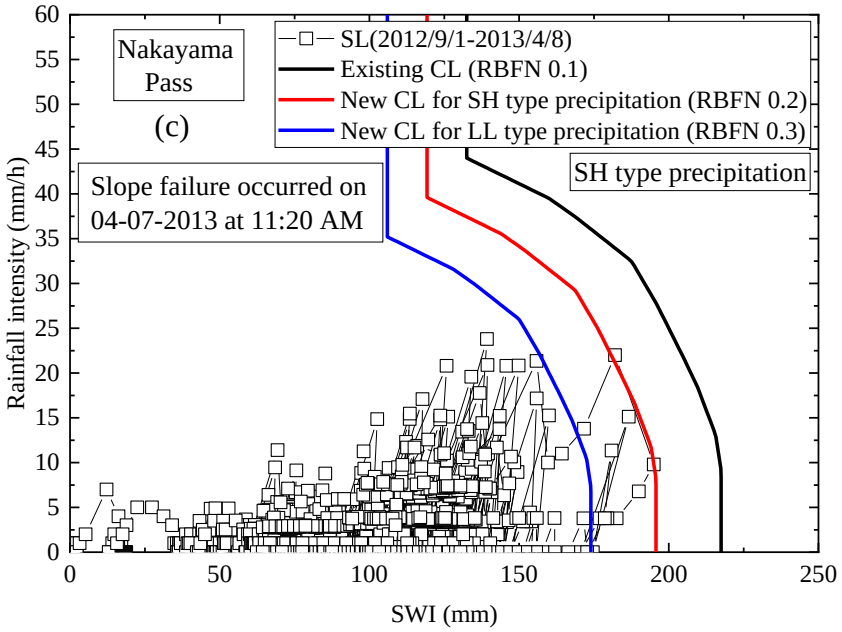

Figure 5.12 Applicability of the new CLs proposed for Nakayama Pass by rainfall history in the calculation period: (a) 04/01/2002-05/03/2012; (b) 09/01/2011-05/05/2012 and (c) 09/01/2012-04/08/2013.

5.3.3 Applicability of the proposed stability assessment approach for natural slopes in Hokkaido

The above-performed parametric studies are based on homogeneous embankment slopes with different slope angles and heights, while the proposed stability assessment approach should also be applicable to set the early warning criterion for the natural slopes. According to Kobayashi et al. (2014), three different patterns of slope failures along roadways in Hokkaido have been identified as shown in Figure 5.13. The three different patterns of slope failures have the following characteristics: Pattern A, the soil deposited on the top terrace of the rock slope collapses with a small volume. From the upper part of the slope, the debris mixed with the soil and sand flows to the roadway. Pattern B, the failure happens on the cut slope of thick soil sediment. It collapses from a relatively deep depth with a large scale to reach the roadway. Pattern C, topsoil distributes on a steep rock slope. The depth of collapse is shallow, and the scale is small. Among them, Pattern B is the same as the slope failure at Nakayama Pass.

In this section, a series of numerical simulations for the three slope failure patterns are performed using the soil properties for Nakayama Pass employed in the former section. The analytical method as well as the simulation period of initial analysis, soil water content simulation, and slope stability analysis are the same as used in section 5.3.2. To reflect the actual ground condition of slopes, the three different patterns of slope failures were separately simulated using four slope models, namely high-steep slope (20 m, 45˚), high-gentle slope (20 m, 30˚), short-steep slope (5 m, 45˚), and short-gentle slope (5 m, 30˚) as shown in Table 5.6.

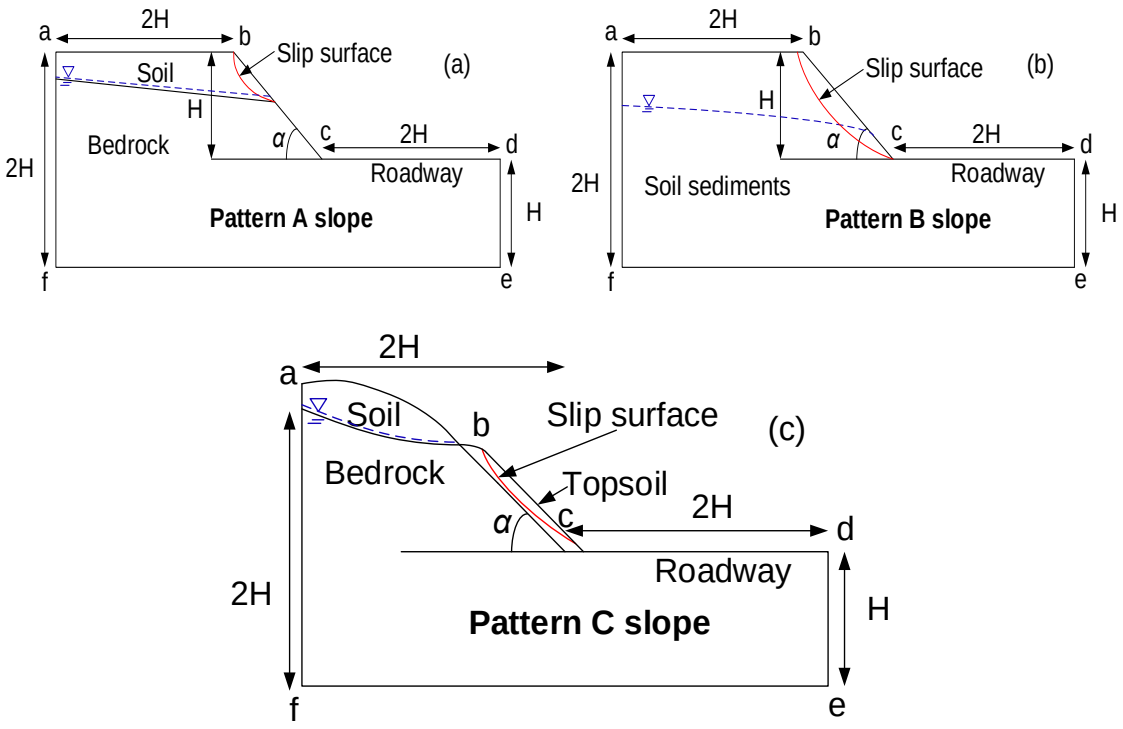

Figure 5.13 Schematic models and characteristics for the three different patterns of slope failures.

Table 5.6 Four slope models under the three different patterns of slope failures.

Slope model		Slope angle, α (°)	
		30	45
Slope height, H (m)	5	Short-gentle slope	Short-steep slope
	20	High-gentle slope	High-steep slope

Table 5.7 Bedrock properties used in the numerical simulations for natural slopes.

Property name	Value
Dry density, ρ_s (kg/m^3)	2000
Porosity, φ	0.2
Saturated hydraulic conductivity, k_s (m/s)	3.47×10^{-9}
Residual volumetric water content, θ_r (m^3/m^3)	0.008
Saturated volumetric water content, θ_s (m^3/m^3)	0.2
Unfrozen thermal conductivity of saturated soil, λ_u (kJ/(Day·m·°C))	117.6
Frozen thermal conductivity of saturated soil, λ_f (kJ/(Day·m·°C))	173

Unfrozen volumetric heat capacity, ζ_u (kJ/(m^3·°C))	2490
Frozen volumetric heat capacity, ζ_f (kJ/(m^3·°C))	1567
Effective cohesion, c' (kPa)	37
Effective internal friction angle, ϕ' (°)	21

The boundary conditions are the same as the model shown in Figure 5.9. For Pattern A slope and Pattern C slope, the GWL was set at the interface between bedrock and soil. For Pattern B slope, the GWL was set to -3 m below the slope surface. The bedrock properties used in the simulations are listed in Table 5.7 and the soil properties are the same as in Table 5.3. A total of 60 numerical simulations using four slope models (Table 5.6) under fifteen combination conditions of precipitation (Table 5.5) were performed for each pattern of slope failures. Figure 5.14 shows the new CLs for the three different patterns of slope failures determined by the numerical results. The occurrence of slope failure (black point) indicates the first point with the factor of safety less than 1.0 along with the SL for the numerical slope failure case.

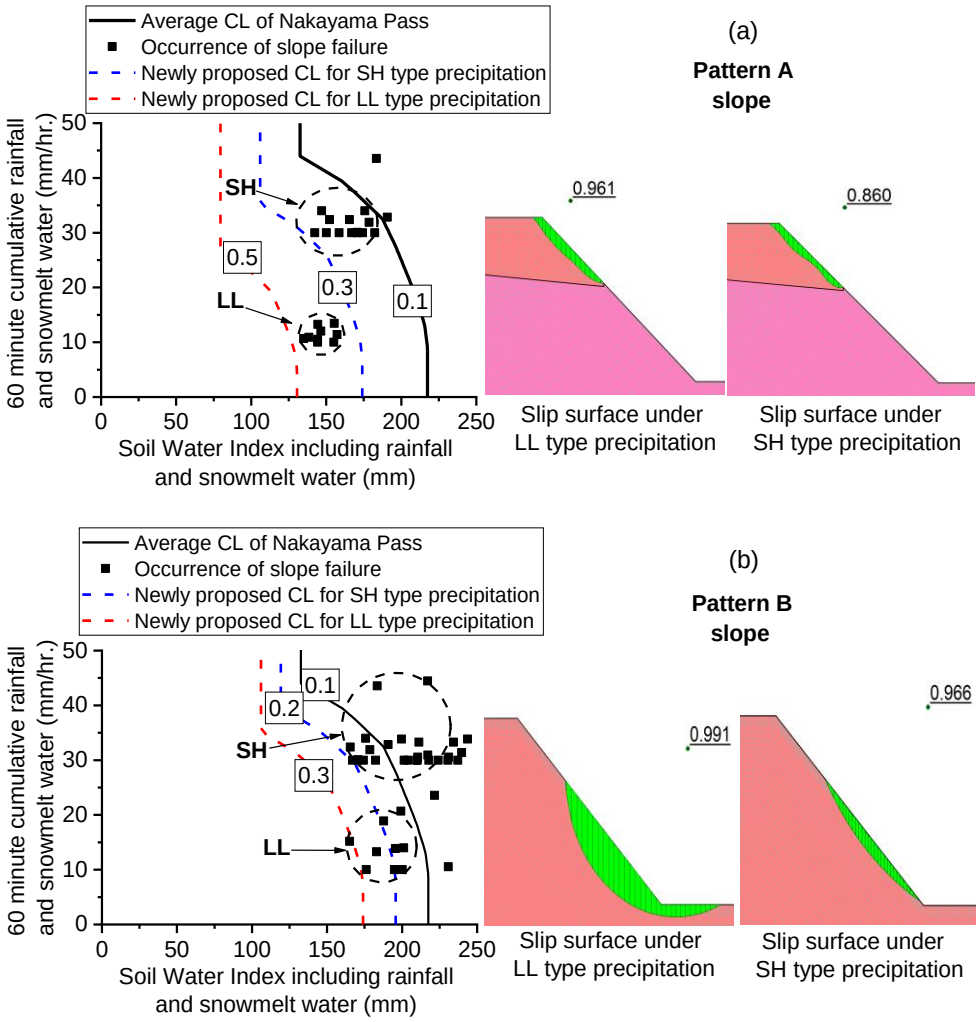

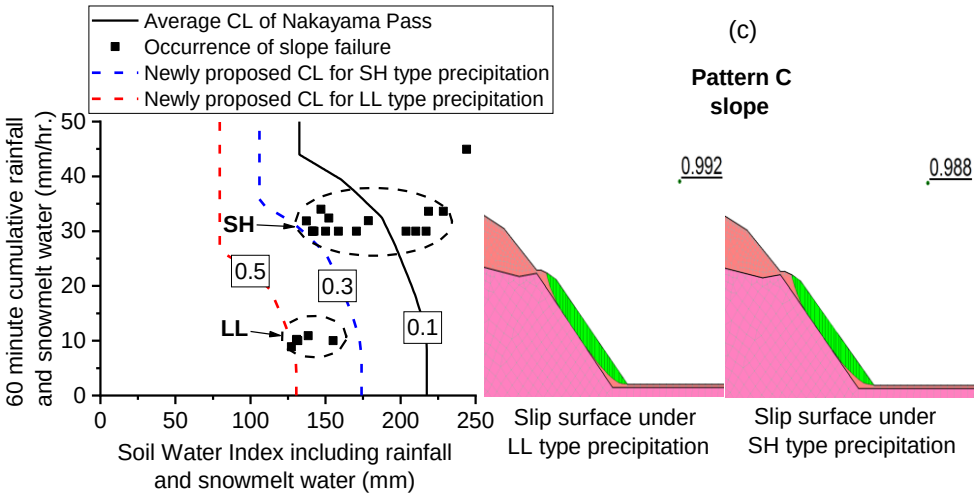

Figure 5.14 New CLs and simulated slip surfaces for the three different patterns of slope failures.

Besides, Figure 5.14 also shows the slip surfaces of short-steep slope models under LL type and SH type precipitation for each pattern of slope failures. From the shape of the slip surface shown in Figure 5.14, it can be identified that for Pattern A and Pattern C slopes, the slope failures are shallow, and the position of the slip surface is almost the same under SH and LL type precipitation. For Pattern B slope, SH type precipitation rapidly increases the saturation of the surface layer causing shallow slope failures. On the other hand, as there is no bedrock, the rainwater and/or snowmelt water in case of LL type precipitation can slowly infiltrate into deeper soil layers increasing the saturation of the deeper layer, which induces the occurrence of deep-seated slope failure. The simulation results suggest that it needs to set the CL individually for each combination of three different patterns of slope failures under two typical types of precipitation conditions as summarized in Table 5.8, i.e., for Pattern A and Pattern C slope failures, the existing early warning criteria under SH type and LL type precipitation can be revised to RBFN 0.3 and RBFN 0.5, respectively, while for Pattern B slope failures, the existing early warning criteria under SH type and LL type precipitation can be revised to RBFN 0.2 and RBFN 0.3, respectively, as new early warning criteria for early warning of rainfall and/or snowmelt induced slope failures in Hokkaido, Japan.

Table 5.8 Summary of the newly proposed early warning criteria.

Rainfall type	Pattern A slope	Pattern B slope	Pattern C slope
SH type	RBFN 0.3	RBFN 0.2	RBFN 0.3
LL type	RBFN 0.5	RBFN 0.3	RBFN 0.5

5.4 Proposal for a New Determination Method for Early Warning Criterion

5.4.1 New determination method for early warning criterion

In the previous sections, a new early warning criterion was proposed for each combination of three different patterns of slope failures under two typical types of precipitation conditions based on case studies and parametric analyses. Furthermore, it was found that by using the cluster of CLs in the local region as an index to explain the local geology and geography, the new early warning criterion (Table 5.8) could predict the occurrence of the rainfall and/or snowmelt induced slope failures, without directly considering the local soil properties. Therefore, the newly proposed determination method for early warning criterion can be shown in Figure 5.15.

Firstly, the hourly snowmelt water is incorporated into the Japanese early warning system by using meteorological monitoring data and modeled snow density. Then, from the calculated SL, the precipitation conditions are divided into two typical types: SH type and LL type. Next, the cluster of CLs is plotted by using all existing CLs in the local area, and the average CL for the cluster of CLs is set as the RBFN 0.1 to determine the RBFN values of the new early warning criteria based on the RBFN method (Kuramoto et al., 2001). Finally, new early warning criteria are proposed for predicting three different patterns of slope failures under the two typical types of precipitation conditions by considering the local ground condition determined from the disaster prevention inspection records and the cluster of CLs in the local area.

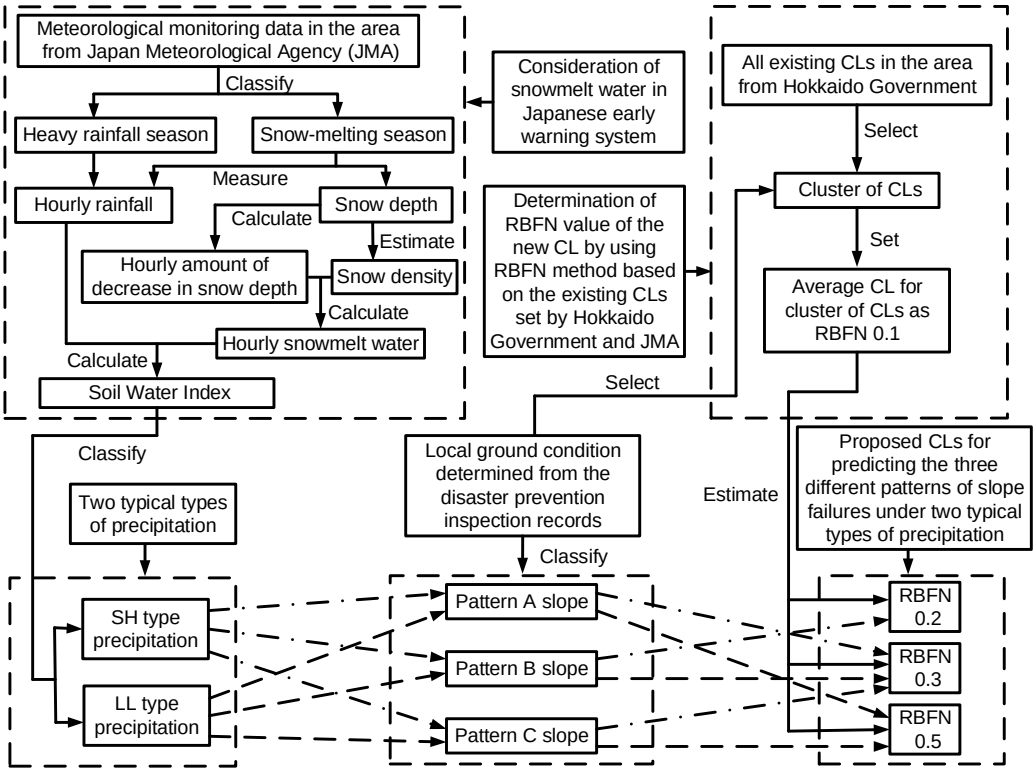

Figure 5.15 Operation of new determination method for early warning criterion.

5.4.2 Applicability and reliability of the new determination method for early warning criterion

Historical records and meteorological monitoring data at the time of the slope failures are available in the subprefectures in Hokkaido, Japan shown in Figure 5.16. Table 5.9 lists the information on the disasters that occurred in these subprefectures. The applicability and reliability of the new determination method for early warning criterion are discussed against the actual cases of rainfall and/or snowmelt induced slope failures in these subprefectures. At first, Setana-cho, Shinhidaka-cho, and Kaminokumi-cho are taken as examples for explaining the determination process of the cluster of CLs as shown in Figure 5.7. During the determination process of the cluster of CLs in Setana-cho, Shinhidaka-cho, and Kaminokumi-cho, for Shinhidaka-cho and Kaminokumi-cho, all CLs (blue line, the CL set in the blue grid) are collected to plot the cluster of CLs as shown in Figure 5.7(c) and Figure 5.7(d). However, for Setana-cho, most of the CLs (blue line) are concentrated in a small area of the cluster of CLs, while a few CLs (red line, the CL set in the red grid) significantly increase the variation of the cluster of CLs as shown in Figure 5.7(b). Therefore, the CLs with red color are excluded because they are not considered to be representative CL describing the soil properties and ground conditions of the local area.

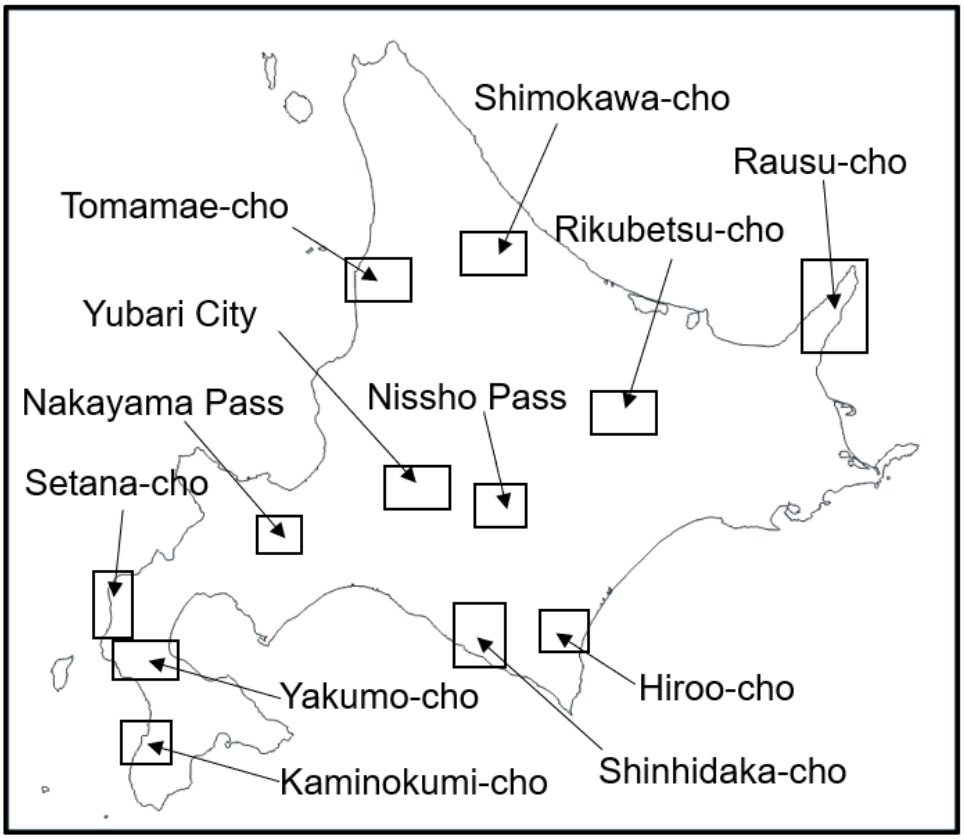

Figure 5.16 Location of subprefectures with historical records of rainfall and/or snowmelt induced slope failures.

Table 5.9 List of rainfall and/or snowmelt induced sediment disaster events in Hokkaido, Japan (after Iwakura et al. 2010; Kurahashi et al. 2018).

No.	Disaster area	Date	Characteristic of the disaster	Slope pattern	Cause
1	Shimokawa-cho	04-18-1999 17:00	Soil collapse deposited on the top of rock slope	Pattern A	Rainfall and snowmelt
2	Shinhidaka-cho	05-15-2000 01:00	Soil collapse deposited on the top of rock slope	Pattern A	Rainfall and snowmelt
3	Yakumo-cho	02-22-2004 19:00	Soil collapse deposited on the top of rock slope	Pattern A	Rainfall and snowmelt
4	Kaminokumi-cho	08-03-2008 17:28	Cut slope failure	Pattern B	Rainfall
5	Setana-cho	07-29-2010	Topsoil collapse distributed on the roadside slope	Pattern C	Rainfall
6	Setana-cho	07-16-2011	Soil collapse deposited on the top of rock slope	Pattern A	Rainfall
7	Tomamae-cho	04-26-2012	Topsoil collapse distributed on the roadside slope	Pattern C	Rainfall and snowmelt
8	Yubari City	04-27-2012	Embankment slope failure	Pattern B	Rainfall and snowmelt
9	Rausu-cho	04-24-2015 18:00	Topsoil collapse distributed on the roadside slope	Pattern C	Rainfall and snowmelt
10	Rikubetsu-cho	Early April-2016	Topsoil collapse distributed on the roadside slope	Pattern C	Snowmelt
11	Hiroo-cho	03-09-2018	Topsoil collapse distributed on the roadside slope	Pattern C	Rainfall and snowmelt

Figure 5.17 shows the SLs when the slope failures occurred in Setana-cho, Shinhidaka-cho, and Kaminokumi-cho during the heavy rainfall season (or non-snow-melting season). It is recognized that the maximum point of SL (near slope failure time) has not yet exceeded the lower boundary for the cluster of CLs, meaning that the existing Japanese early warning criteria are much higher than realistic ones in these areas. Subsequently, the new CL is proposed (red line in Figure 5.17) based on the new determination method for early warning criterion for the slope failures at Setana-cho, Shinhidaka-cho, and Kaminokumi-cho (See Table 5.8 and Table 5.9). It is recognized that the newly proposed CLs successfully predict the occurrence of slope failures in these areas during heavy rainfall season, meaning that the newly proposed determination method can be applied to the prediction of the slope failures during heavy rainfall season in an arbitrary area in Hokkaido. The main reason is that the distribution of soil saturation is mainly affected by the precipitation conditions as discussed in section 5.3. Therefore, when using SWI for predicting the occurrence of slope failures in mountain areas as shown in Figure 5.17, it can be considered that the slope failure mechanism only depends on the slope of the SL (rainfall intensity), and the occurrence time of the slope failure is mainly affected by the difference in the starting point (initial conditions of water content due to the former rainfall) and slope of the SL.

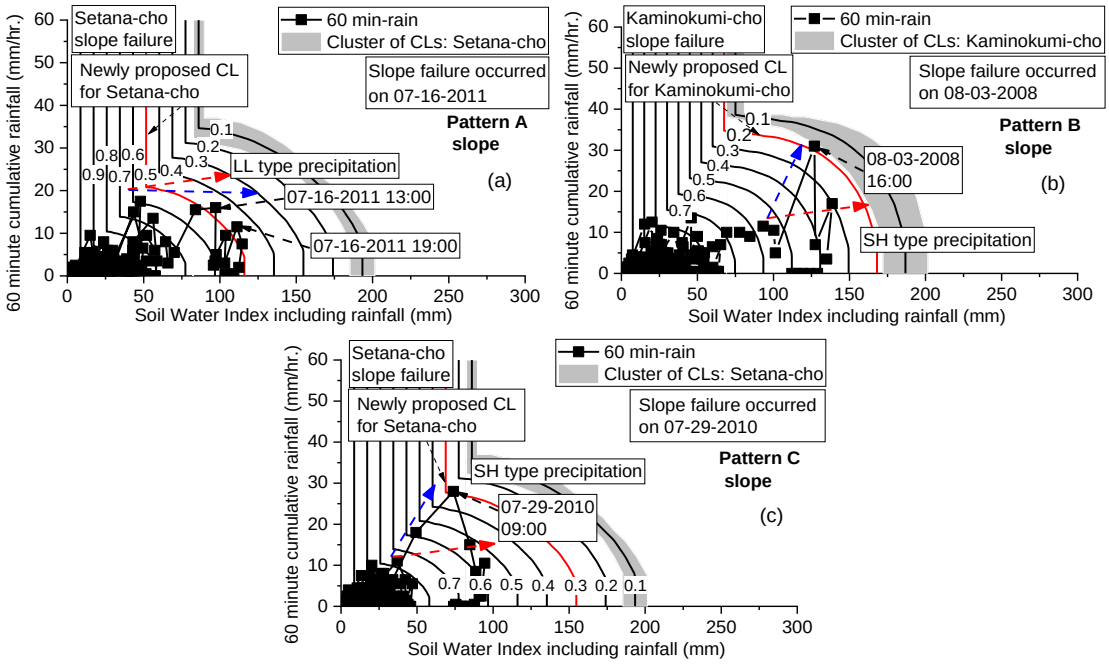

Figure 5.17 Newly proposed CL for subprefectures in Hokkaido during heavy rainfall season.

However, it is worth noting that there is a difference in the CL location between the cluster of CLs and the newly proposed CL. The main reason is that the target areas in this study are mainly mountain areas, while as shown in Figure 5.7, the Hokkaido government does not set the CLs in many mountain areas, so it differs from the setup areas for the existing CLs. Since the mountain area is a steep water catchment terrain and it has weak disaster prevention measures as compared with the town area, the newly proposed CL is smaller than the cluster

of CLs. This indicates that although the cluster of CLs is effective in the town area, it is not applicable in the mountain area. Furthermore, the newly proposed CLs determined by the new determination method for early warning criterion against the slope failures that occurred in the subprefectures in Hokkaido during the snow-melting season is shown in Figure 5.18. According to Figure 5.18, before the disasters happened, a large amount of snowmelt water increased SWI, i.e., the moisture content of the soil ground. Therefore, it is impossible to use the snake line that does not consider snowmelt water (the line with black points) to predict the occurrence of slope failure during the snow-melting season. However, even if the snowmelt water is considered, the peak value of the snake line (the line with white points) has not yet exceeded the lower boundary for the cluster of CLs, which is inconsistent with the occurrence of the disaster. Accordingly, the new CLs for predicting rainfall and/or snowmelt induced slope failures are proposed in these subprefectures based on the newly proposed determination method for early warning criterion shown in Figure 5.15. It is recognized that the new CLs (red lines in Figure 5.18) can successfully predict the occurrence times for rainfall and/or snowmelt induced slope failures under each combination of the three different patterns of slope failures under the two typical types of precipitation conditions in all these areas.

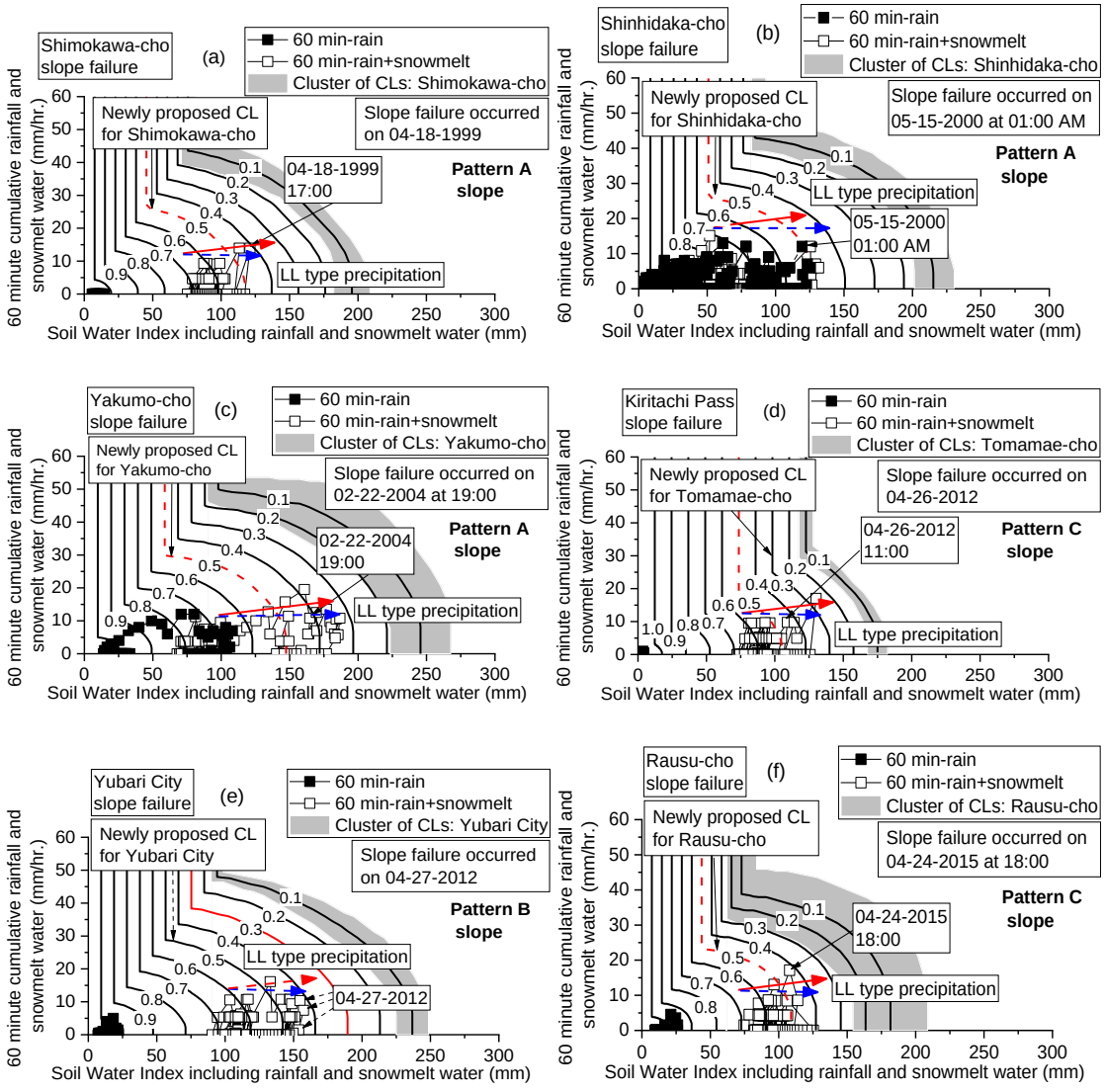

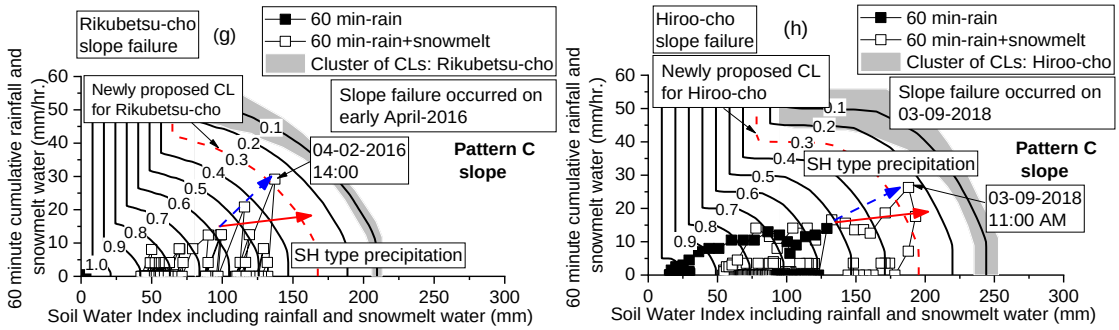

Figure 5.18 Newly proposed CL for subprefectures in Hokkaido during the snow-melting season.

Through the comparison of Figure 5.17 and Figure 5.18, it seems reasonable to conclude that the newly proposed determination method is effective in rationally setting the early warning criterion not only for rainfall-induced slope failures without freeze-thaw actions but also for rainfall and/or snowmelt induced slope failures with freeze-thaw actions in an arbitrary area in Hokkaido, Japan. The reason is that the frozen soil layer disappears at the end of March in Hokkaido, Japan (Zhu et al., 2018), while most of the slope failures occur in April and May as shown in Figure 5.18. If some time passes after the frozen soil layer disappears, the effects of freeze-thaw actions can hardly be seen. Therefore, the influence of freeze-thaw actions on setting the early warning criterion is ignorable, which agrees well with the finding by Siva Subramanian et al. (2017) that the freeze-thaw action has a very small impact on soil water content and factor of safety. On the other hand, Rahardjo et al. (2007) found that the soil properties and rainfall intensity are the primary factors controlling the instability of slopes, while the initial GWL and slope geometry only play a secondary role. In this study, the above four factors are considered in the new determination method for early warning criterion, i.e., the rainfall intensity and/or snowmelt rate, initial GWL, soil properties, and slope geometry are represented by the slope of the SL, starting point of the SL, local existing early warning criteria and slope pattern, respectively, which makes the newly proposed determination method effective in rationally setting the early warning criterion both during the snow-melting season and during heavy rainfall season. The advantage of the newly proposed determination method is that since the existing early warning criteria near the target area already have taken the influences of the variation in the local geology and geography into account, the new determination method for early warning criterion can be applied to the arbitrary area in seasonally cold regions without directly considering the local soil properties, in the actual design and maintenance works.

5.5 Summary of This Chapter

In 2005, the Japanese government launched a new nationwide early warning system for predicting debris flow and slope failure disasters based on rainfall intensity and Soil Water Index (SWI). However, the Japanese government has not set early warning criteria in many mountain areas. Besides, the existing early warning criteria are much higher than realistic ones in some areas, and snowmelt water has not been considered during

the calculation of SWI. These cause many slope failures in seasonally cold regions, which were induced by rainfall and/or snowmelt, have not been predicted. Therefore, this chapter attempts to propose a new determination method for setting an early warning criterion of rainfall and/or snowmelt induced slope failures in seasonally cold regions. For this purpose, this chapter firstly proposes a combination model for estimating snow density to incorporate hourly snowmelt water into the Japanese early warning system more accurately by using meteorological monitoring data and modeled snow density. Next, based on case studies and parametric analyses for slope stability assessment, new early warning criteria are proposed for predicting three different patterns of slope failures under two typical types of precipitation (rainfall and snowmelt) conditions. Finally, a new determination method for setting the early warning criterion in seasonally cold regions is proposed by referring to the existing early warning criteria near the target area, in accordance with the precipitation types and the local ground condition of the slope. Since the existing early warning criteria near the target area already have taken the influences of the variation in the local geology and geography into account, the new determination method for early warning criterion can be applied to the arbitrary area in seasonally cold regions without directly considering the local soil properties, in the actual design and maintenance works.

The research findings in this chapter propose an effective method for determining the early warning criterion of rainfall and/or snowmelt induced slope failures in seasonally cold regions. It can be used in both a wide range assessment of slope stability and an implementation of the structural measures for three different patterns of slope failures during heavy rainfall and snow-melting seasons, at the actual design and maintenance works. However, as the global climate change due to global warming, the amount of snowmelt will be more difficult to estimate during the snowmelt period in the future. Factors such as the rise in groundwater level caused by glacial melting and the thawing of permafrost in seasonally cold regions pose challenges for the prediction of slope failures in these areas. Therefore, indirectly reflecting these factors by fitting the relevant parameters to the in-situ soil moisture measurement data will be the tentative scheme of the next study.

6 PROBABILITY ASSESSMENT OF SLOPE INSTABILITY WITH FREEZE-THAW ACTIONS UNDER CLIMATE CHANGE IN COLD REGIONS

The slope stability is influenced by the uncertainty in climate factors, whereas uncertainty is not quantified in the traditional deterministic analysis (Yang and Yeh, 2019). Accordingly, the objective of this chapter was (1) to semi-quantitatively evaluate the impact of uncertainty in climate factors on slope stability based on numerical simulations, and (2) to evaluate the impact of climate change on the occurrence of slope failure and its probability distribution based on historical statistics and parametric analysis of slope failures. The parametric analysis of slope failures was performed by imputing three kinds of climate boundary conditions: meteorological monitoring data, meteorological analysis data, and meteorological simulation data. Among them, the meteorological monitoring data is obtained from the Automatic Meteorological Data Acquisition System, named AMeDAS. The meteorological analysis data is a reasonable predicted value of the future meteorology based on the regression analysis of the meteorological monitoring data of the past 120 years. The meteorological simulation data is obtained by downscaling the outputs of four different Global Circulation Models (GCMs). Finally, climate prediction and assessment of instability of an actual highway embankment slope were done based on dynamical downscaling techniques and the slope stability assessment approach.

6.1 Meteorological Monitoring Data and Future Climate Prediction

To analyze the influence of climate change on an area with different scale (e.g. world, Japan and Sapporo (a city in Hokkaido, Japan)), according to the meteorological monitoring data of the world, Japan, and Sapporo referred from JMA, this chapter analyzes the trend of annually average air temperature deviation (Figure 6.1(a)), annually cumulative precipitation deviation (Figure 6.1(b)), magnification of precipitation (Figure 6.1(c)), and the number of days with air temperature below zero (Figure 6.1(d)) in the past 120 years (1900-2020). The benchmark of deviation is the average value of 30 years (1981-2010). Figure 6.1(a) shows that the world annually average air temperature increases approximately by 0.8 ^{o}C per 100 years, while the values of Japan and Sapporo are 1.27 ^{o}C per 100 years and 2.46 ^{o}C per 100 years, respectively. It means that global warming has a significant impact on Japan, especially on Sapporo. Figure 6.1(b) plots the annually cumulative precipitation deviation. Six intervals of 20 years are divided over the past 120 years to analyze the change of the annually cumulative precipitation deviation. It can be seen that the number of positive values on the three scales are 12, 14, and 15, respectively, in the past 20 years (2000-2020), which are all the maximum values since 1920. It means that the number of years with high rainfall is increasing. Figure 6.1(c) and Figure 6.1(d) show the magnification of precipitation and the number of days with air temperature below zero in Sapporo, respectively. The results of fitting curves display that the magnification of precipitation increases by 0.094 per

100 years, and the number of days with air temperature below zero decreases 16.8 days per 100 years in Sapporo. It means that the precipitation is increasing, and Winter is getting shorter in Sapporo.

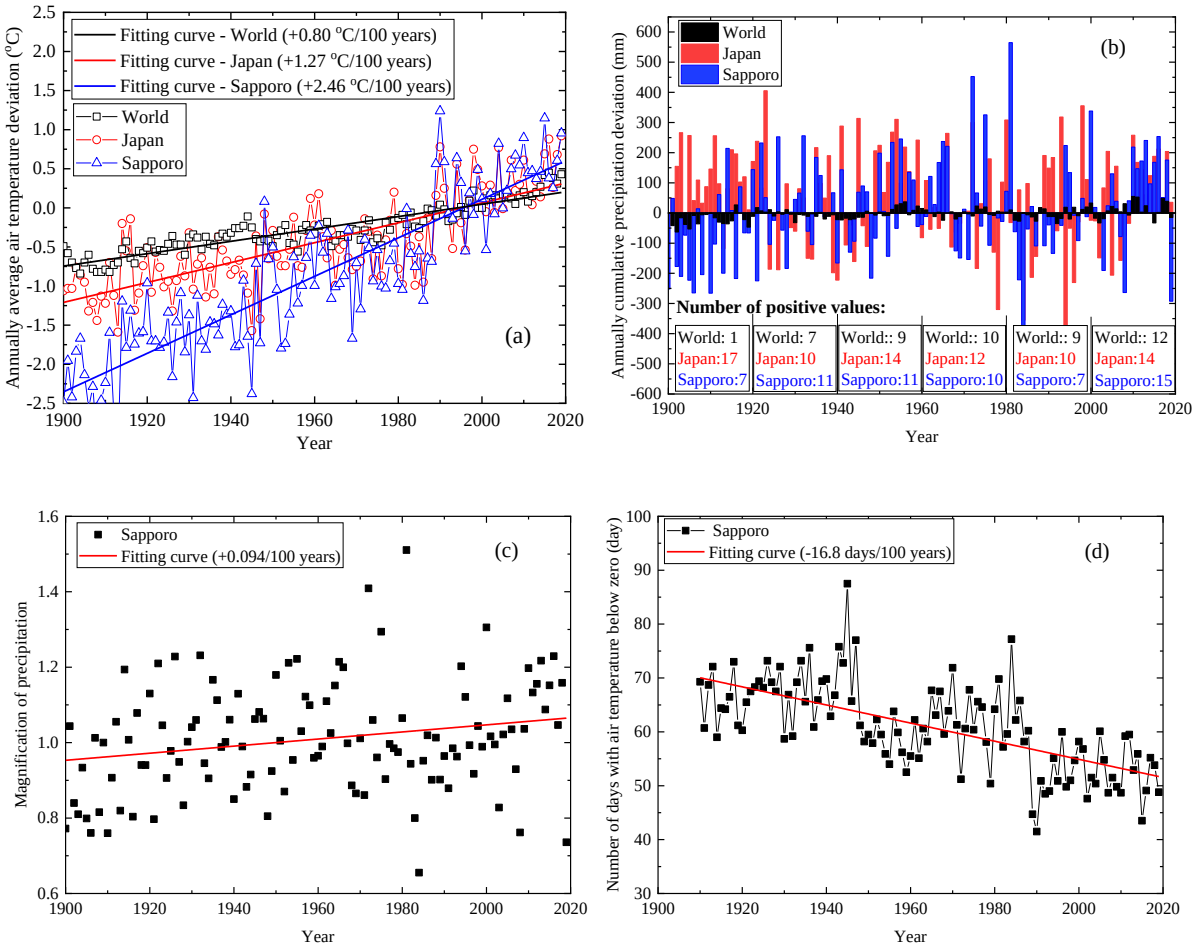

Figure 6.1 Meteorological monitoring data of the world, Japan, and Sapporo referred from JMA.

To investigate whether climate change has different effects on air temperature in different seasons, the air temperature of the world, Japan, and Sapporo change in four seasons (March-April-May (MAM); June-July-August (JJA); September-October-November (SON); December-January-February (DJF) are analyzed separately as shown in Figure 6.2. It is recognized that in all seasons, the impact of climate change on the temperature of Sapporo is greater than that of Japan, which is greater than that of the world. If the focus in Sapporo, climate change has the most obvious effect on the air temperature in the Winter season (DJF, increases by 2.89 °C per 100 years), followed by Spring season (MAM, increases by 2.63 °C per 100 years), and then Autumn season (SON, increases by 2.30 °C per 100 years), and finally Summer season (JJA, increases by 2.03 °C per 100 years).

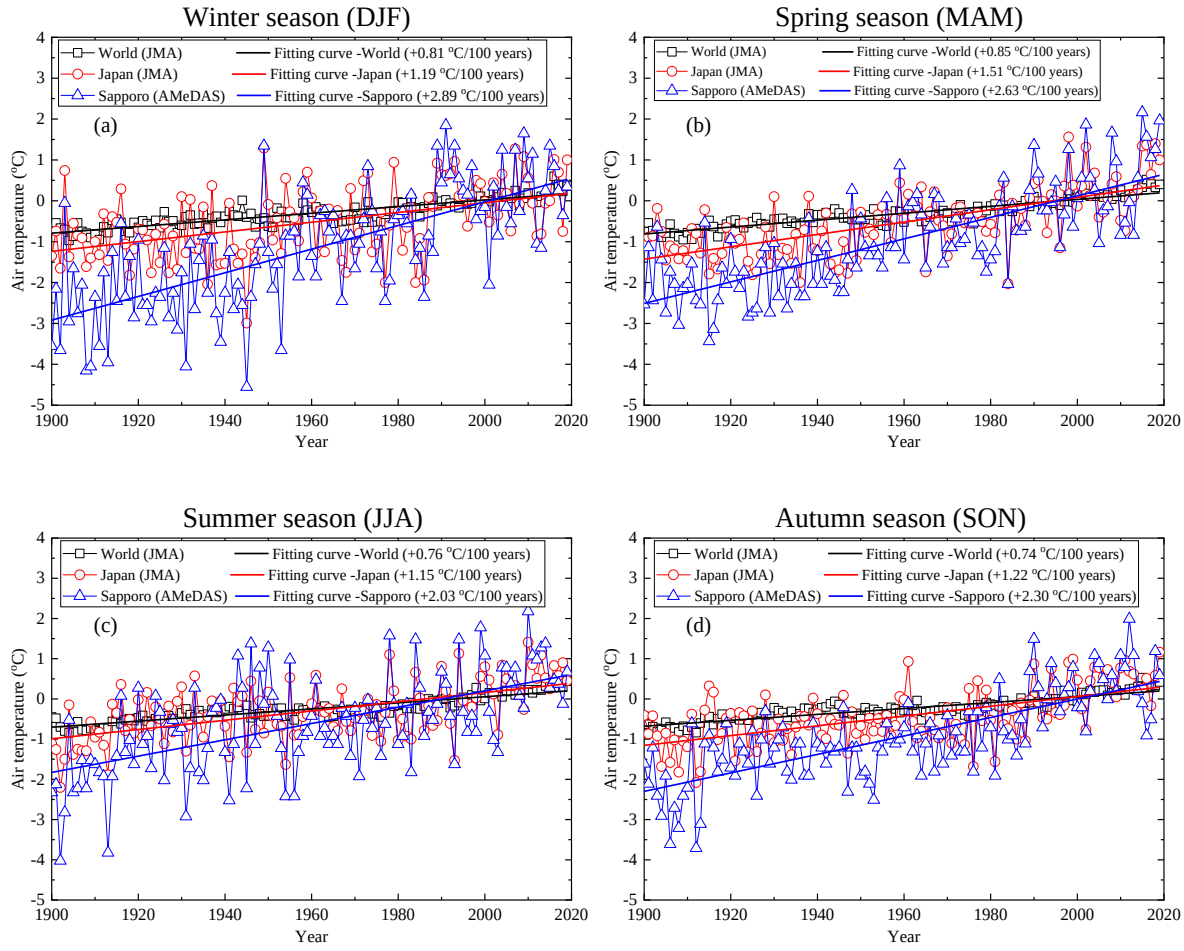

Figure 6.2 Temperature of the world, Japan, and Sapporo change in different seasons.

6.2 Probability Assessment of Slope Instability under Climate Change

According to the regression analysis results of the meteorological monitoring data of the past 120 years, climate change is increasing the air temperature and precipitation in Japan (especially in cold regions like Sapporo). To semi-quantitatively evaluate the impact of uncertainty in climate factors on slope stability and to evaluate the impact of climate change on the occurrence of slope failure and its probability distribution, this section takes an embankment slope at Nakayama Pass (located in Sapporo) in 2013 as a typical case for parametric analysis using the slope stability assessment approach proposed by Siva Subramanian et al. (2017).

6.2.1 Simulation model and boundary conditions

A two-dimensional numerical model is established to simulate the effects of climate change on slope stability the same as the model as shown in Figure 5.9. The numerical simulations were performed with different slope angles (30˚, 35˚, 40˚, and 45˚) and different slope heights (5 m, 10 m, 15 m, and 20 m) to reflect various in situ conditions of natural embankment slopes. During the initial analysis and stability analysis, climate data is applied on the soil surface (ab, bc, cd in Figure 5.9) and set adiabatic boundary conditions at the right side (de in Figure 5.9), the bottom side (ef in Figure 5.9), and lift side (af in Figure 5.9). Due to the right side of the

model is adjacent to the bedrock, no flow boundary is applied on the lift side (af in Figure 5.9) and free drainage boundary is applied on the right side (de in Figure 5.9) and bottom side (ef in Figure 5.9). The climate boundary conditions applied in the model are maximum and minimum air temperature, maximum and minimum relative humidity, wind speed, and accumulative precipitation (rainfall or snowfall) on every time step (one day). The relative humidity, air temperature, and precipitation are computed at the elapsed time of the day with sinusoidal climate distribution. The air temperature is assumed to be at its minimum value at sunrise and at its maximum value at 12:00 pm (noon). The relative humidity is assumed to be at its maximum at sunrise and its minimum at 12:00 pm. Both the air temperature and relative humidity are distributed sinusoidally between their minimum and maximum times. The amount of precipitation is the daily total amount.

Figure 6.3 shows the original climate data at Nakayama Pass during 2012-2013, which were obtained from the Automatic Meteorological Data Acquisition System (AMeDAS). According to the regression analysis results of the meteorological monitoring data of Sapporo in the past 120 years, the assumption for precipitation is 1.2 times increased and for air temperature is 2 ºC increased in the future. Therefore, 4 kinds of assumed climate boundary conditions (case 1, case 2, case 3, and case 4 as listed in Table 6.1) were applied to 16 kinds of numerical models (4 slope heights × 4 slope angles).

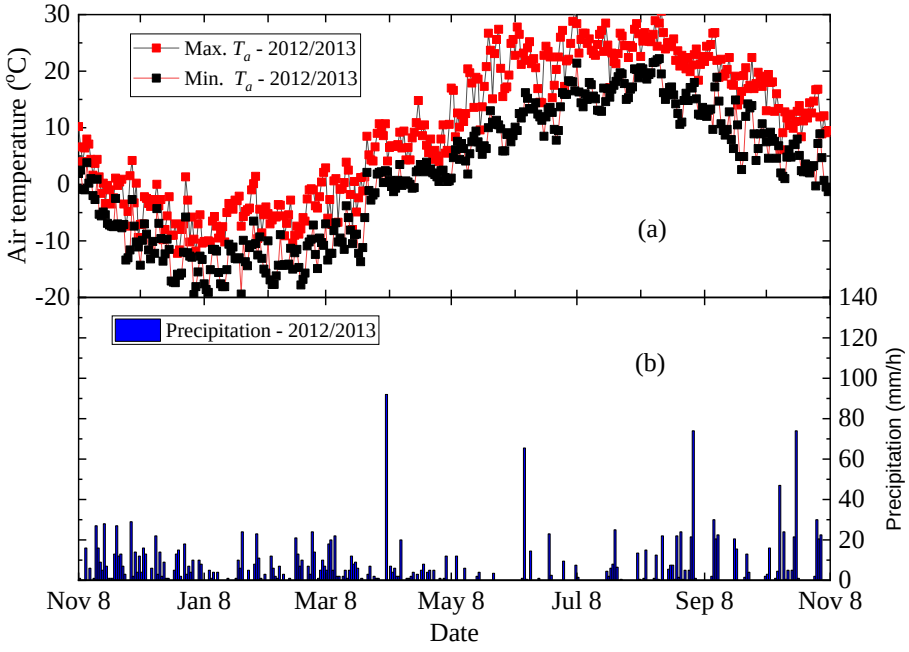

Figure 6.3 Original climate data at Nakayama Pass during 2012-2013.

A total of 64 numerical models were simulated for Nakayama Pass. The soil material properties used for the numerical simulation of the embankment slope model are given in Table 6.2. The parameters, i.e., dry density (ρ_s), porosity (φ), saturated hydraulic conductivity (k_s), effective cohesion (c'), and effective internal friction angle (ϕ') were obtained from laboratory element tests (Hokkaido Regional Development Bureau, 2013; Siva Subramanian et al. 2017). Based on the method given by Fredlund et al. (2002), the SWCC of the embankment

filling material were estimated from the grain size distribution curve. The parameters for which no laboratory measurements are available, i.e., thermal conductivity (λ), volumetric heat capacity (ζ), and residual volumetric water content (θ_r), were estimated based on the grain size curve of soil (SoilVision, 2018).

Table 6.1 Study cases of boundary conditions.

Case name	Precipitation condition	Temperature condition
Case 1	Original climate data (AMeDAS)	Original climate data (AMeDAS)
Case 2	Original climate data (AMeDAS)	T_a + 2°C
Case 3	Precip. × 1.2	Original climate data (AMeDAS)
Case 4	Precip. × 1.2	T_a + 2°C

Table 6.2 Soil properties used for the simulation.

Parameters	Value
Dry density (ρ_s)	1684 kg/m^3
Effective cohesion (c')	0 kPa
Effective internal friction angle (ϕ')	37°
Porosity (φ)	0.472
Saturated hydraulic conductivity (k_s)	5.62 ×10^{-7} m/s
Volumetric water content of the soil at 0°C (θ_{wf})	0.19 m^3/m^3
Saturated volumetric water content (θ_s)	0.472 m^3/m^3
Residual volumetric water content (θ_r)	0.12 m^3/m^3
Unfrozen thermal conductivity (λ_u)	127.04 kJ/(Day·m·°C)
Frozen thermal conductivity (λ_f)	132.24 kJ/(Day·m·°C)
Unfrozen volumetric heat capacity (ζ_u)	2237 kJ/(m^3·°C)
Frozen volumetric heat capacity (ζ_f)	1624 kJ/(m^3·°C)

6.2.2 Simulation results

The calculated snow depth, daily snowmelt, daily infiltration, and daily rainfall under the four climate conditions are shown in Figure 6.4. Figure 6.4(a) displays the calculated and measured snow depth. The results suggest that the calculated snow depth under case 1 is consistent with the measurement data, meaning that the simulation results are reliable. From Figure 6.4(a), it is identifiable that when the air temperature increased by 2 ^{o}C, the time when the snow disappeared was advanced from June 1st (case 1) to May 23rd (case 2), and the maximum snow depth was decreased from 2.79 m (case 1) to 2.66 m (case 2). When the precipitation increased by 1.2 times, the maximum snow depth was increased from 2.79 m (case 1) to 3.42 m (case 3). From Figure 6.4(b) and Figure 6.4(c), it can be seen that the increase in the air temperature plays a key role in the snowmelt and infiltration during the Spring season and the end of the Autumn season. The main reason is that on one hand air temperature controls snowmelt during those periods and the snowmelt water is the main water supply of the infiltration.

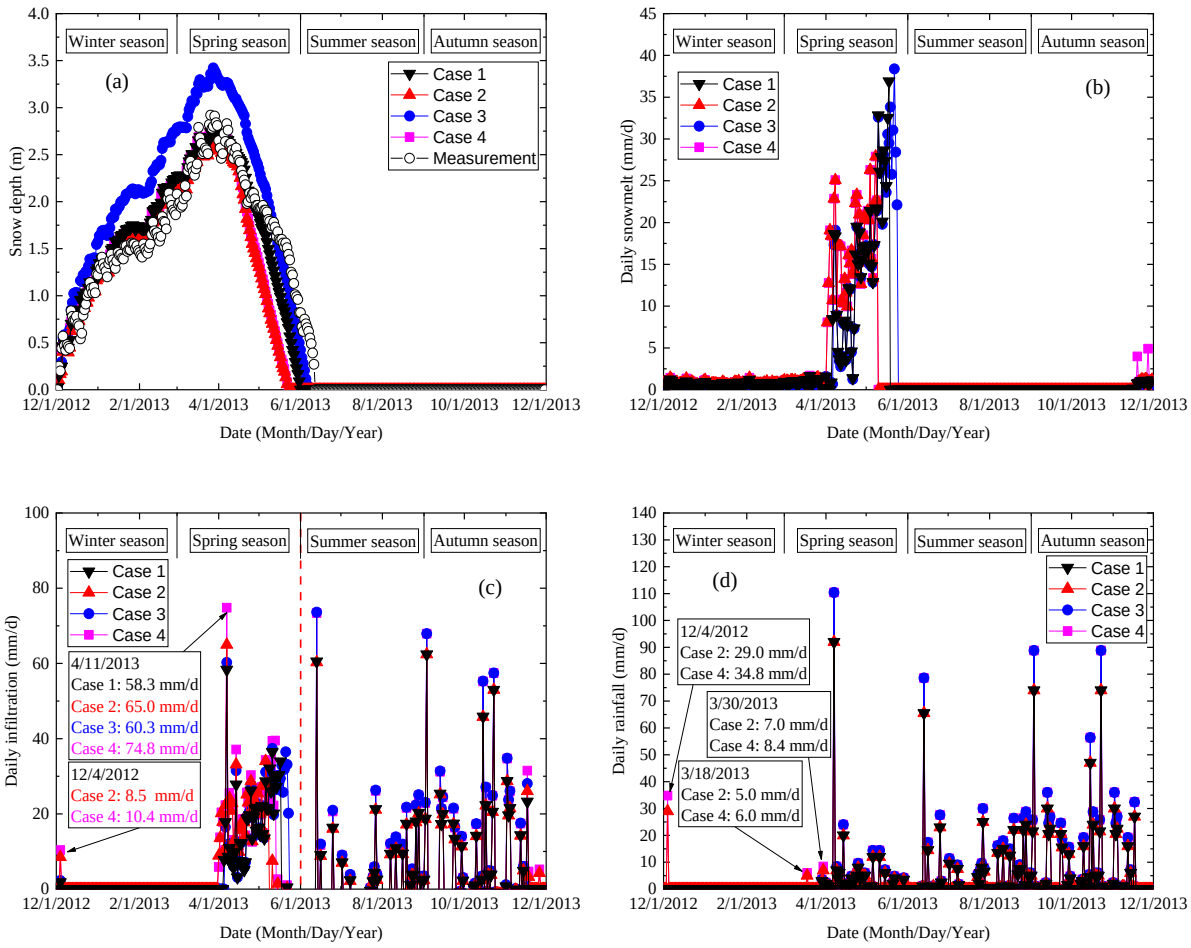

Figure 6.4 Simulation results (a) snow depth vs. time; (b) daily snowmelt vs. time; (c) daily infiltration vs. time and (d) daily rainfall vs. time.

On the other hand, when the air temperature increased by 2 °C, during the Spring season and the end of Autumn season, in the days that the air temperature below the threshold temperature (0 oC) before has becomes above the threshold temperature, which causes some snowfall is converted into the form of rainfall as shown in Figure 6.4(d). At the same time, more snow on the ground surface melt into water and decreases the snow depth.

To evaluate the effects of climate change on the occurrence of slope failure and its probability distribution based on historical statistics and parametric analysis of slope failures, a year is divided into two different intervals according to the different causes of slope failures: Winter-Spring period (the main cause of slope failure is snowmelt water) and Summer-Autumn period (the main cause of slope failure is heavy rainfall). The probability distribution is described by probability density function, which is a function that describes the probability of the output value of this random variable near a certain value point.

$$f(x) = \frac{1}{\sqrt{\pi/2}\times\sigma} exp\left(-2 \times \frac{(x-\mu)^2}{\sigma^2}\right) \tag{6.1}$$

where, *f(x)* is the normal density at *x*, σ and μ are fitting parameters. The changes in μ will not change the shape of the curve. It only causes the curve to translate along the x-axis. The changes of σ only change the shape of the curve as shown in Figure 6.5.

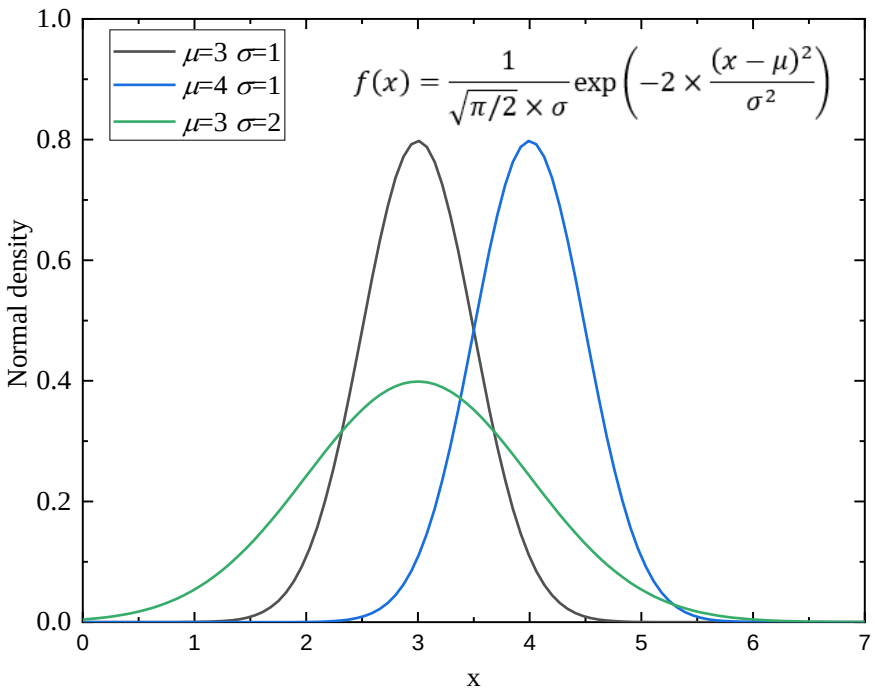

Figure 6.5 Schematic diagram of the probability density function.

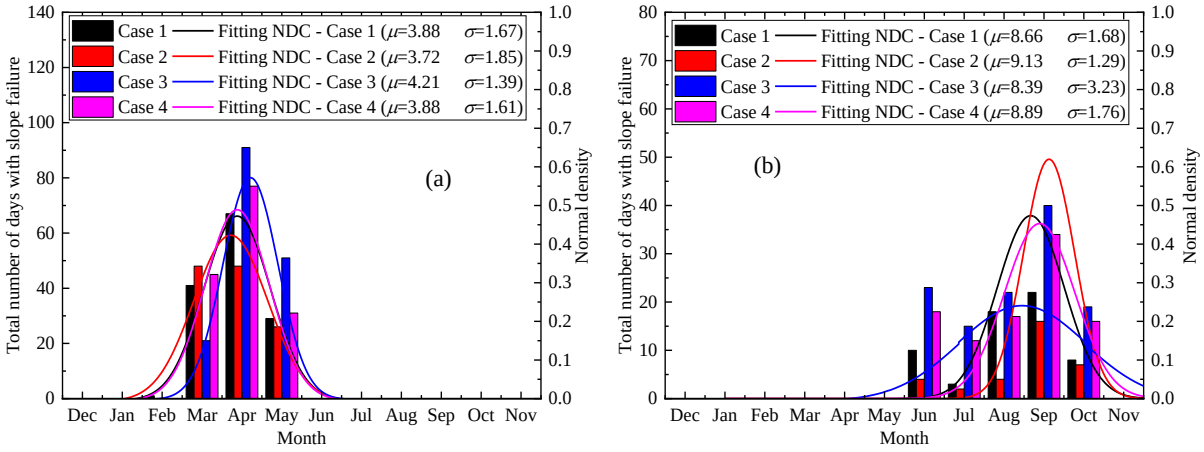

Figure 6.6 Total number of days with slope failure and the fitting normal density curve (NDC) of 64 numerical models (a) during the Winter-Spring period; (b) during the Summer-Autumn period.

Figure 6.6(a) and Figure 6.6(b) show the total number of days with slope failure and the fitting normal density curve (NDC) of 64 numerical models during the Winter-Spring period and during the Summer-Autumn period, respectively. From Figure 6.6, it can be recognized that when air temperature increases 2 ^{o}C (case 2) compared with the original climate conditions (case 1), during the Winter-Spring period, the value of μ will decrease and that of σ will increase. The NDC becomes chunky and moves to March. It means that the increased air temperature causes more slope failures to occur earlier and broadens the time domain of slope failures in the Spring season. During the Summer-Autumn period, it is the exact opposite that the increased air temperature causes an increase in μ and a decrease in σ. The NDC becomes thin and tall and moves to October. It means that the increased air temperature causes more slope failures to occur later and narrows the time domain of slope failures in the Autumn season. When precipitation increases 1.2 times (case 3) compared with the original climate conditions (case 1), during the Winter-Spring period, the value of μ will increase and that of σ will decrease. The NDC becomes thin and tall and moves to May. It means that the increased precipitation causes more slope failures to occur later and narrows the time domain of slope failures in the Spring season. During the Summer-Autumn period, it is the exact opposite that the increased precipitation causes a decrease in μ and an increase in σ. The NDC becomes chunky and moves to June and July. It means that the increased precipitation causes more slope failures to occur earlier and broadens the time domain of slope failures in the Summer season. When considering changes in temperature and rainfall together, it can be seen that both μ and σ decreases during the Winter-Spring period and increases during the Summer-Autumn period. This is consistent with the trend of slope failures in Japan investigated by the MLIT from 2008 to 2017 as shown in Figure 6.7. It indicates that the occurrence of slope failures will be more concentrated in April during the Winter-Spring period, while during the Summer-Autumn period, the time domain of its occurrence will become wider.

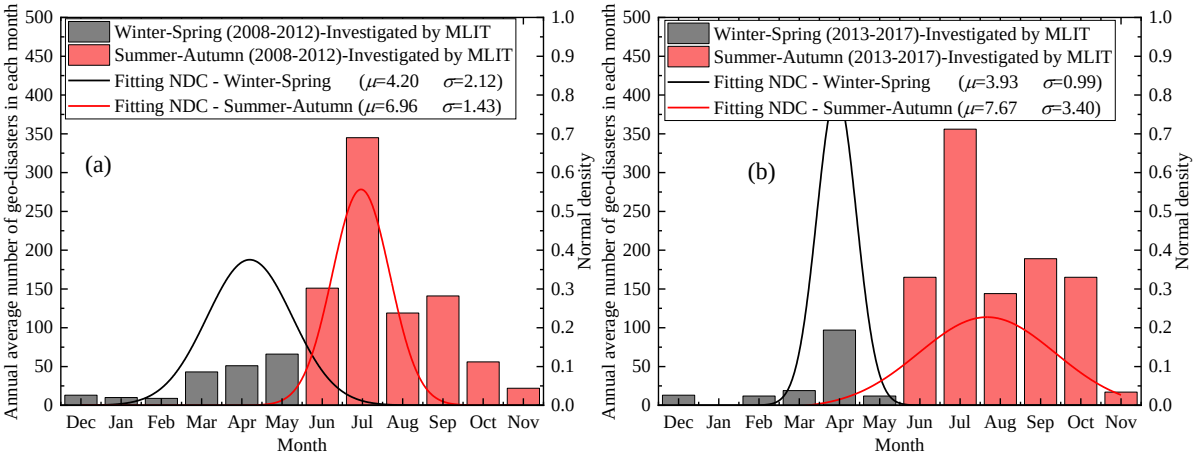

Figure 6.7 Annual average number of geo-disasters in each month and the fitting normal density curve (NDC) of investigate results (a) during 2008-2012 and (b) during 2013-2017.

6.3 Climate Prediction Based on Dynamical Downscaling Techniques and Assessment of Highway Slope Instability

The Nakayama Pass is a high incidence area of slope failures during the snowmelt period. To further analyze the impact of future climate change on slope stability, climate prediction based on dynamical downscaling techniques and assessment of highway slope instability were performed at Nakayama Pass, Hokkaido, Japan.

6.3.1 Climate prediction based on dynamical downscaling techniques

The meteorological monitoring data at Nakayama Pass in the past (2012-2013) was obtained from the Automatic Meteorological Data Acquisition System (AMeDAS). The future climate data (2090-2091) at Nakayama Pass is estimated by using the hybrid-downscaling method proposed by (Yamada et al., 2014). Figure 6.8 shows the past and future climate data. It can be seen that the average maximum air temperature increases 0.6 ^{o}C, and the average minimum air temperature increases by 3.29 ^{o}C in 2090. Therefore, the average air temperature increases by about 1.945 ^{o}C in the next 80 years at Nakayama Pass, which is consistent with an increase of 2.46 ^{o}C per 100 years in Sapporo obtained from the regression analysis of the meteorological monitoring data of the past 120 years as shown in Figure 6.1(a). Besides, the annual cumulative precipitation increases from 1882 mm (2012-2013) to 2131 mm (2090-2091). The magnitude of the precipitation increases by about 0.13, which is slightly larger than an increase of 0.094 per 100 years of the magnitude of the precipitation in Sapporo shown in Figure 6.1(c). Figure 6.9 shows the comparison of past climate data and future climate data. From Figure 6.9, it can be seen that temperature and rainfall are increasing in the future, especially in the Winter season.

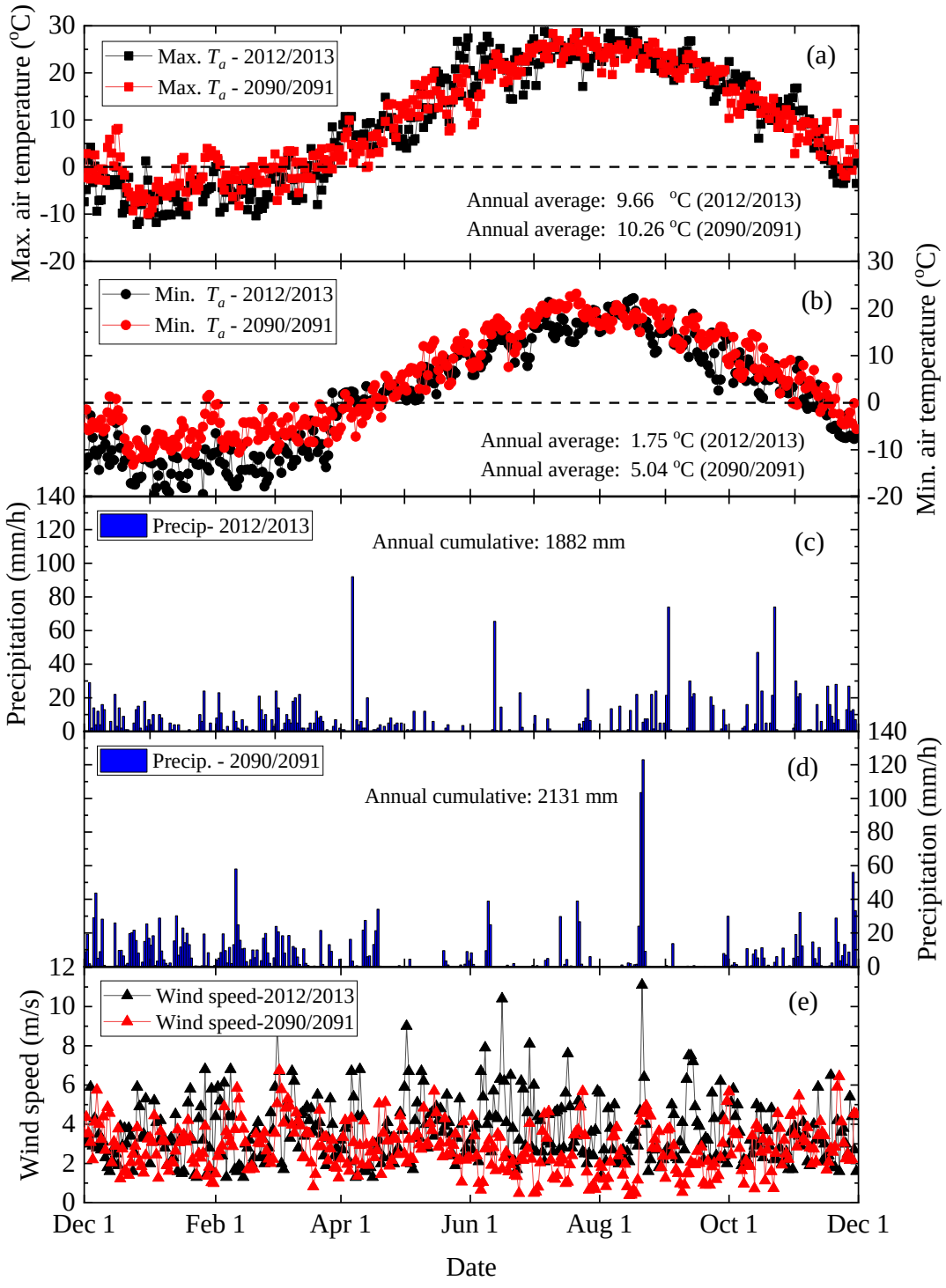

Figure 6.8 Climate in the past and future at Nakayama Pass: (a) maximum air temperature; (b) minimum air temperature; (c) Precipitation during 2012-2013; (d) Precipitation during 2090-2091; (e) wind speed.

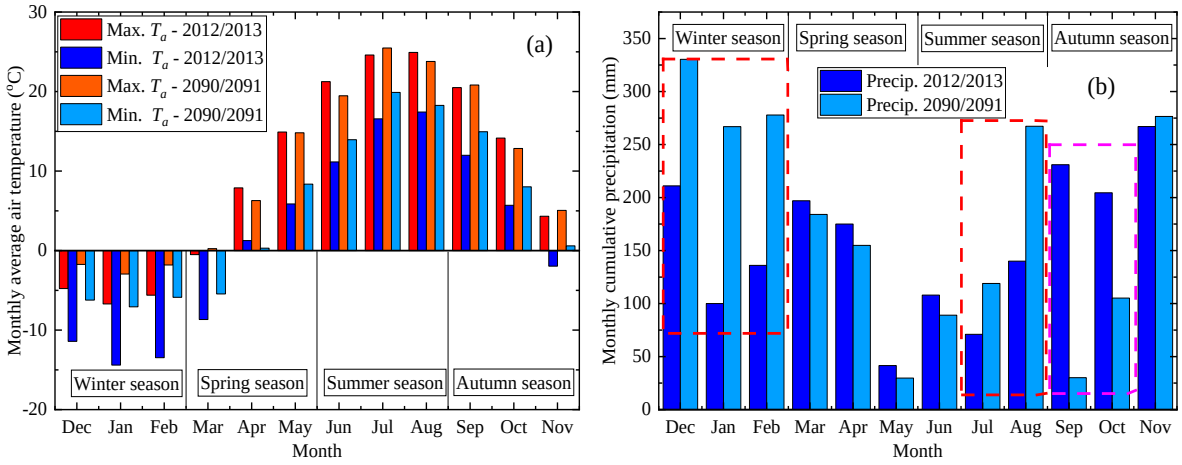

Figure 6.9 Comparison of past climate data and future climate data.

6.3.2 Assessment of highway slope instability

The parametric analysis of slope failures at Nakayama Pass was performed by imputing meteorological monitoring data obtained from AMeDAS and meteorological simulation data obtained from GCMs. The two-dimensional numerical model with boundary conditions for highway slope at Nakayama Pass is designed using the geological cross-sectional data. The slope stratigraphy consists of three layers of soil/rock, namely embankment filling, talus slope materials, and the bedrock (Andesite). The two-dimensional numerical model with the slope stratigraphy and surveyed groundwater table is given in Figure 6.10.

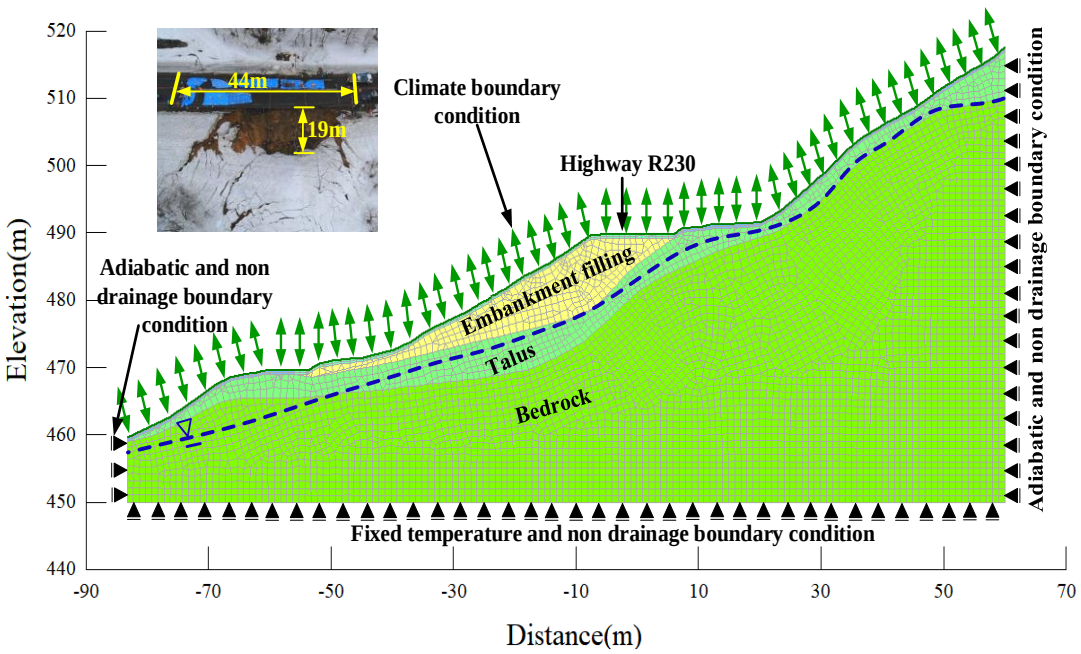

Figure 6.10 Two-dimensional numerical model with boundary conditions for highway slope at Nakayama Pass.

Five kinds of boundary conditions for parametric studies are listed in Table 6.3. The soil properties used for the numerical simulation of the highway slope model are given in Table 6.4. For the embankment filling and talus material, the unsaturated shear strength data is not available so that the available undrained shear strength is considered for the embankment filling, and saturated shear strength is estimated for the talus slope material. The bedrock is modeled as an impenetrable material.

Table 6.3 Boundary conditions for parametric studies.

Boundary name	Air temp. (2012/2013)	Precip. (2012/2013)	Wind speed (2012/2013)	Air temp. (2090/2091)	Precip. (2090/2091)	Wind speed (2090/2091)
B1	O	O	O	×	×	×
B2	×	O	O	O	×	×
B3	O	×	O	×	O	×
B4	O	O	×	×	×	O
B5	×	×	×	O	O	O

Table 6.4 Soil properties used for the simulation.

Parameters	Embankment filling	Talus materials
Dry density *(ρ_s)*	1400 kg/m^3	1200 kg/m^3
Effective cohesion *(c')*	9.75 kPa	52 kPa
Effective internal friction angle (ϕ')	35°	11.36°
Porosity (φ)	0.47	0.53
Saturated hydraulic conductivity (k_s)	5.62 ×10^{-7} m/s	1 ×10^{-4} m/s
Volumetric water content of soil at 0°C (θwf)	0.15 m^3/m^3	0.10 m^3/m^3
Unfrozen thermal conductivity *(λ_u)*	127.04 kJ/(Day·m·°C)	103.7 kJ/(Day·m·°C)
Frozen thermal conductivity *(λ_f)*	132.24 kJ/(Day·m·°C)	135.7 kJ/(Day·m·°C)

Unfrozen volumetric heat capacity (ζ_u)	2237 kJ/(m^3·°C)	2398 kJ/(m^3·°C)
Frozen volumetric heat capacity (ζ_f)	1624 kJ/(m^3·°C)	1392 kJ/(m^3·°C)

6.4 Results and Discussions

To study the main climate factors affecting the slope stability in the future, the variation in the factor of safety (FOS), ground surface temperature, vol. (volumetric) water content and infiltration are given in Figure 6.11. From Figure 6.11(a), it could be seen that there is a longer unstable state of the highway slope at Nakayama Pass under B3 (53 days) and B5 (64 days) boundary conditions compared with the B1 (22 days) boundary conditions. It means that climate change (especially the increase in precipitation) in the future will enhance the instability of the slopes and lead to more slope failures occur. From Figure 6.11(b), it is recognized that the cumulative infiltration between March 1st and July 1st (surrounded by the red dash box) is 1142.1 mm, 1283.7 mm, and 1173.3 mm under B1, B2, and B4 condition, respectively. The difference in infiltration is almost negligible. However, the cumulative infiltration between March 1st and July 1st is 1930.4 mm and 2055.2 mm under b3 and B5 condition with an increase of approximately 69% and 80%, respectively. During this period, the ground surface is unfrozen as shown in Figure 6.11(c). Therefore, the infiltration causes the increase of the vol. water content as shown in Figure 6.11(d). The increase of the vol. water content causes the decrease of suction in the unsaturated soil and the increase of the positive pore water pressure in the saturated soil, which eventually causes the occurrence of the slope failure. Accordingly, it can be obtained that climate change (especially the increase in precipitation) in the future will increase the infiltration and cause more slope failures during the Spring season.

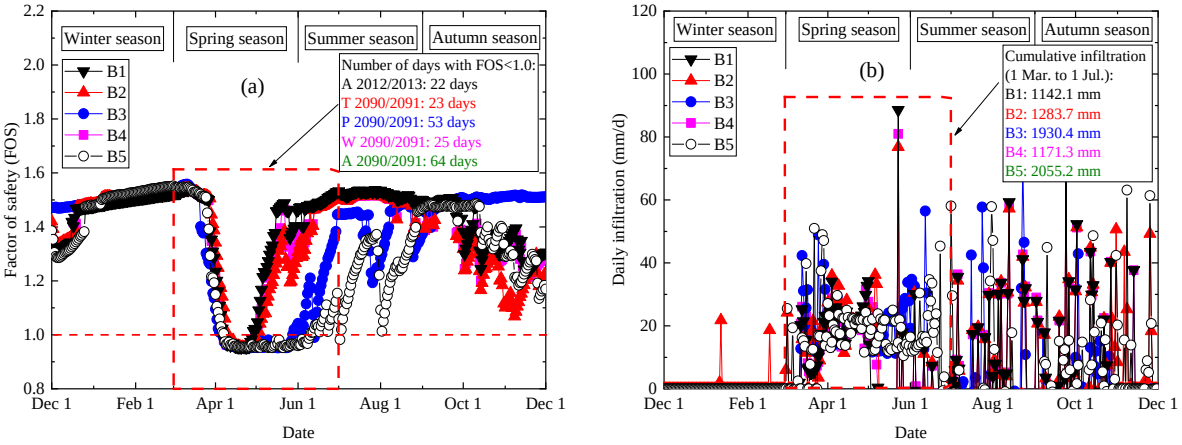

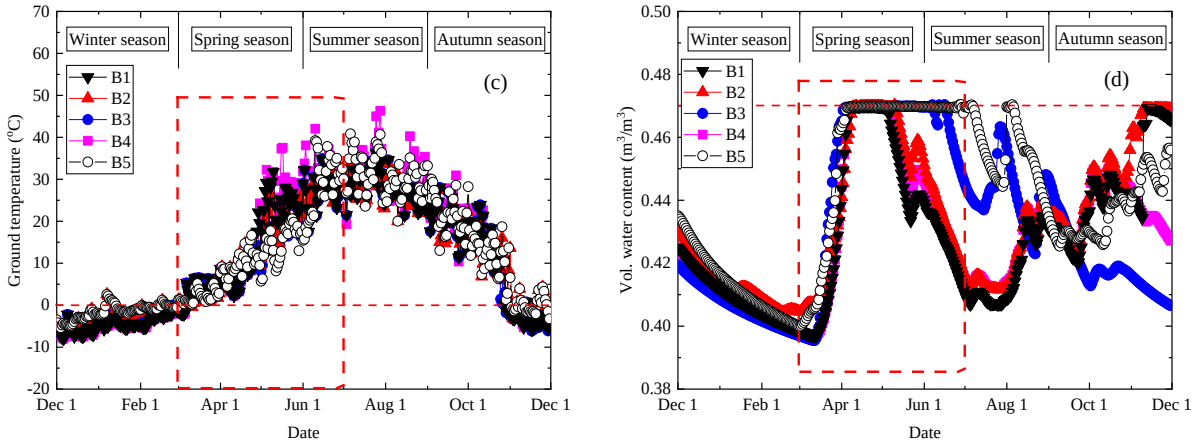

Figure 6.11 Simulation results of (a) FOS vs. time; (b) Daily infiltration vs. time; (c) Ground surface temperature vs. time and (d) vol. water content vs. time.

6.5 Summary of This Chapter

This chapter proposes an effective approach to evaluate the effects of climate change on slope stability. Firstly, to semi-quantitatively evaluate the effects of climate changes on the uncertainty of climate factors, this chapter analyzes the trend of the two main climate factors (air temperature and precipitation) based on the regression analysis of the meteorological monitoring data of the past 120 years in different scales (e.g. world, Japan, and Sapporo). Next, to discuss the effects of climate changes on the occurrence of slope failure and its probability distribution, the parametric analysis of an assumed 2-dimensional homogeneous slope model with considering freeze-thaw action was performed. Finally, climate prediction and assessment of instability of an actual highway embankment slope were done based on dynamical downscaling techniques and the slope stability assessment approach. The meteorological simulation data is obtained by downscaling the outputs of 3 different regional atmospheric models (RAMs) with lateral boundary conditions from 3 different general circulation models (GCMs). The results indicate that affected by global warming, the air temperature rise in some cold regions (such as Sapporo, Japan) is more serious. Changes in air temperature and precipitation will affect the shape of the normal density curve (NDC) of the slope failures. The climate changes (especially the increase in precipitation) in the future will increase the infiltration during the Spring season. It will lengthen the time that the highway slope is in an unstable state, thereby enhancing the instability of the slopes and lead to more slope failures occur in the future.

The research findings in this chapter propose an effective method to semi-quantitatively evaluate the effects of uncertainty of climate factors on slope stability, the effects of climate change on the occurrence of slope failure, and the probability distribution of the slope failures by using parametric analysis of slope failures. It can be used in the assessment of slope stability and implementation of the structural measures at the actual design and maintenance works in the future.

7 CONCLUSIONS AND RECOMMENDATIONS

The conclusions and recommendations of this study are summarized in four parts. The first part is from Chapter 3 explaining the main conclusions of the local shear strength (LSS) method and the FEM-MPM hybrid coupled model based on the LSS method for the numerical simulation on the local-scale. The second part is from Chapter 4 detailly explaining the main finding of the study on heavy rainfall-induced instabilities of multi slopes by simulating a hybrid coupled model of surface flow, subsurface flow, and soil mechanics on the catchment-scale. The third part is from Chapter 5 detailly explaining the main finding of the study on prediction and early warning of rainfall and snowmelt induced soil slope failures by a new determination method for setting an early warning criterion on the regional-scale. The fourth part is from Chapter 6 detailly explaining the main finding of the study on the evaluation of the effects of climate change on slope stability on the regional-scale.

7.1 Conclusions and Recommendations

The findings from Chapter 3 can be outlined as follows:

1. This chapter proposes an LSS method for determining the variable LSS corresponding to the variable MS for each soil material point within a catchment-scale unsaturated slope. The LSS method built a relationship between the variable LSS with the variable MS of each soil material point during rainfall infiltration by shifting the M-C failure envelope.

2. A FEM-MPM hybrid coupled model is proposed based on the LSS method to solve landslide-related large-deformation problems subjected to rainfall infiltration in unsaturated slopes. The results of landslide analysis suggest that the ultimate slope failure shape simulated by FEM-MPM hybrid coupled model is quite similar to the slip surface simulated by the LEM and SSRT. The proposed FEM-MPM hybrid coupled model is proved to be effective for simulating the landslide-related large-deformation problems that involve variable pore water pressures and has the potential to understand the initial position and the morphological evolution in the process of the rainfall-induced landslide in the unsaturated soil slopes.

The findings from Chapter 4 can be outlined as follows:

1. The driving force term and friction term are the main contribution terms in the equations of motion in the shallow water equations, while the total contribution of the inertia term, advection term, and velocity term is less than 1% together. Therefore, the diffusion wave approximation that simplifies the equations of motion by considering only the driving force term and friction term is applicable to the practical runoff analysis.

2. The hybrid coupled model of surface flow, subsurface flow, and soil mechanics proposed in this chapter can reflect the two-stage process of rainwater infiltration, i.e. rainfall infiltration in the early stage of rainfall event

and runoff infiltration in the later stage of the rainfall event, and it is also applicable to simulate runoff, infiltration, seepage, and multi slopes instabilities on a catchment-scale range.

3. The LFS approach is more efficient to predict the rainfall-induced slope failures of the target region by simultaneously simulating catchment-scale range multi slopes instabilities, which has significant advantages as compared with other methods to analyze the stability of a single slope. Furthermore, the stability map of multi slopes conduces to determine the dangerous spots in the target region.

The findings from Chapter 5 can be outlined as follows:

1. When using meteorological monitoring data and modeled snow density to incorporate the hourly snowmelt water into the Japanese early warning system, the calculation of hourly snowmelt has high accuracy if separately estimating the snow density during the midwinter (1st December-1st March) and early spring (1st March-30th April) period. For this reason, in this chapter, a combination model for estimating the snow density more accurately in seasonally cold regions was proposed by adopting the SY08 model in the midwinter period and E86 model in the early spring period.

2. The Hokkaido government does not set the CLs in many mountain areas, and the Japanese early warning system does not consider the long-term snowmelt water infiltration. Therefore, based on the results of case studies and parametric analyses for slope stability assessment, new early warning criteria for rainfall and/or snowmelt induced slope failures in Hokkaido, Japan were proposed in this chapter individually for each combination of three different patterns of slope failures under two typical types of precipitation conditions in mountain areas.

3. This chapter proposed a new determination method for setting an early warning criterion of rainfall and/or snowmelt induced slope failures by considering the local existing early warning criteria, in case of the same precipitation (rainfall and snowmelt) types and local ground condition of the slope. Since the existing early warning criteria near the target area already have taken the influences of the variation in the local geology and geography into account, the new determination method for early warning criterion can be applied to the arbitrary area in seasonally cold regions without directly considering the local soil properties, in the actual design and maintenance works.

The findings from Chapter 6 can be outlined as follows:

1. According to the regression analysis results of the meteorological monitoring data of the past 120 years, affected by global warming, the temperature rises in some cold regions (such as Sapporo, Japan) is more serious. Meanwhile, the precipitation is also increasing, and Winter is getting shorter in these cold regions.

2. Climate change has the most obvious effect on the air temperature in the Winter season (DJF) and Spring season (MAM) compared with the Autumn season (SON) and finally Summer season (JJA). During the Spring

season (MAM) and the end of the Autumn season (SON), the increase in the air temperature plays a key role in the snowmelt and infiltration.

3. The increased air temperature causes more slope failures to occur earlier and broadens the time domain of slope failures in the Spring season, while it causes more slope failures to occur later and narrows the time domain of slope failures in the Autumn season. In contrast, the increased precipitation causes more slope failures to occur later and narrows the time domain of slope failures in the Spring season, while it causes more slope failures to occur earlier and broadens the time domain of slope failures in the Summer season.

4. Climate change (especially the increase in precipitation) in the future will increase the infiltration during the Spring season. It will lengthen the time that the highway slope is in an unstable state, thereby enhancing the instability of the slopes and lead to more slope failures occur in the future.

7.2 Future Assignments

The findings of Chapter 3 indicate that the proposed LSS method and FEM-MPM hybrid coupled model is of great significance to evaluate the landslide movement distance and reasonably recommend the installation of barrier structures in the actual design and maintenance works. However, the internal moisture changes and the dynamic support provided by the runoff during the movement of the landslide are not considered in this study. These factors are considered as the assignments in the next step of this study.

The findings of Chapter 4 indicate that the catchment-scale range multi-slope instabilities assessment approach proposed in this study provides an effective way for simulating heavy rainfall-induced runoff and multi-slope instabilities in the target region, and it has significant implications for precisely determining the dangerous spots (instead of areas) in a catchment-scale range and accurately releasing warning information to the dangerous spots. However, due to the limitation of the LFS approach, the exact timing of the slope occurrence is difficult to determine. Therefore, further and more theoretical or numerical studies are recommended to improve the LFS approach and incorporate the runoff into the existing Japanese early warning system.

The findings of Chapter 5 propose an effective method for determining the early warning criterion of rainfall and/or snowmelt induced slope failures in seasonally cold regions. It can be used in both a wide range assessment of slope stability and an implementation of the structural measures for three different patterns of slope failures during heavy rainfall and snow-melting seasons, at the actual design and maintenance works. However, as the global climate changes due to global warming, the amount of snowmelt will be more difficult to estimate during the snowmelt period in the future. Factors such as the rise in groundwater level caused by glacial melting and the thawing of permafrost in seasonally cold regions pose challenges for the prediction of slope failures in these areas. Therefore, indirectly reflecting these factors by fitting the relevant parameters to the in-situ soil moisture measurement data will be the tentative scheme of the next study.

The findings of Chapter 6 propose an effective method to semi-quantitatively evaluate the effects of uncertainty of climate factors on slope stability, the effects of climate change on the occurrence of slope failure, and the probability distribution of the slope failures by using parametric analysis of slope failures. It can be used in the assessment of slope stability and implementation of the structural measures at the actual design and maintenance works in the future. However, more study cases need to be studied and more factors need to be considered in future studies.

LIST OF REFERENCES

Abdul, A.S., Gillham, R.W., 1984. Laboratory studies of the effects of the capillary fringe on streamflow generation. Water Resources Research. 20 (6), 691-698.

Abe, O., Higashiura, M., Numano, N., Sato, A., 1989. Profiles of Snow cover at Shinjo City for 15 Years (1973/74-1987/88 winter seasons). Research Report of National Research Center for Disaster Prevention. 44, 123-136 (in Japanese).

Abe, O., Shimizu, M., 2004. Equivalent snow density to estimate snow load in extremely heavy snow areas. Journal of the Japanese Society of Snow and Ice. 66 (1), 11-16 (in Japanese).

Abe, K., Soga, K., Bandara, S., 2013. Material point Method for coupled hydromechanical problems. Journal of Geotechnical and Geoenvironmental Engineering. 140(3), 04013033.

Acharya, G., Cochrane, T.A., Davies, T., Bowman, E., 2009. The influence of shallow landslides on sediment supply: a flume-based investigation using sandy soil. Engineering Geology. 109(3-4): 161-169.

Aleotti, P., 2004. A warning system for rainfall-induced shallow failures. Engineering Geology. 73(3-4), 247-265.

Andersland, O.B., Ladanyi, B., 2003. Frozen ground engineering. John Wiley & Sons. 1-4.

Anderson, E.A., 1976. A point energy and mass balance model of a snow cover. NOAA Tech. Rep. NWS 19, Office of Hydrology, National Weather Service, Silver Spring.

Anderson, E.A., 2006. Snow Accumulation and Ablation Model–SNOW-17.

Arakawa, H., 2012. Data Report of Snow Survey in Hokkaido, 2011-2012 Winter. Annual Report on Snow and Ice Studies in Hokkaido. 31, S1-S14 (in Japanese).

Bandara, S, Soga, K., 2015. Coupling of soil deformation and pore fluid flow using Material Point Method. Computers and Geotechnics. 63, 199-214.

Baum, R.L., Godt, J.W., 2010. Early warning of rainfall-induced shallow landslides and debris flows in the USA. Landslides. 7(3), 259-272.

Bishop, A.W., 1955. The use of slip circle in the stability analysis of slopes. Géotechnique. 5(1), 7-17.

Bishop, A.W., 1959. The principle of effective stress, Teknisk Ukeblad, Norwegian Geotechnical Institute. 106(39), 859-863.

Blais, E.L., McGinn, R.A., 2011. Critical erosion velocity for natural shale gravels: an empirical study. Prairie Perspectives: Geographical Essays. 14, 51-59.

Bogardi, J., 1978. Sediment Transport in Alluvial Streams (No. 04; TC175. 2, B6.). Budapest: Akademiai Kiado, 826 p.

Bui, H.H., Sako, K., Satomi, T., Fukagawa, R., 2008a. Numerical simulation of slope failure for mitigation of rainfall induced slope disaster of an important cultural heritage. Proc. of Urban Cultural Heritage Disaster Mitigation. 2, 111-118.

Bui, H.H., Fukagawa, R., Sako, K., Ohno, S., 2008b. Lagrangian meshfree particles method (SPH) for large

deformation and failure flows of geomaterial using elastic-plastic soil constitutive model. International journal for numerical and analytical methods in geomechanics. 32(12), 1537-1570.

Caine, N., 1980. The Rainfall Intensity: Duration Control of Shallow Landslides and Debris Flows. Geografiska Annaler. Series A, Physical Geography. 62, 23-27.

Chan, H.-C., Chen, P.-A., Lee, J.-T., 2018. Rainfall-induced landslide susceptibility using a rainfall-runoff model and logistic regression, Water. 10, 1354.

Chen, C.W., Saito, H., Oguchi, T., 2017. Analyzing rainfall-induced mass movements in Taiwan using the soil water index. Landslides. 14, 1031-1041.

Chiang, S.H., Chang, K.T., 2011. The potential impact of climate change on typhoon-triggered landslides in Taiwan, 2010–2099. Geomorphology 133(3-4), 143-151.

Chiu, Y.-Y., Chen, H.-E., Yeh, K.-C., 2019. Investigation of the Influence of Rainfall Runoff on Shallow Landslides in Unsaturated Soil Using a Mathematical Model, Water. 11, 1178.

Chowdhury, R., Flentje, P., 2002. Uncertainties in rainfall-induced landslide hazard. Quarterly Journal of Engineering Geology and Hydrogeology. 35(1), 61-70.

Ciabatta, L., Camici, S., Brocca, L., Ponziani, F., Stelluti, M., Berni, N., Moramarco, T., 2016. Assessing the impact of climate-change scenarios on landslide occurrence in Umbria Region, Italy. Journal of Hydrology 541, 285-295.

Coe, J.A., Godt, J.W., 2012. Review of approaches for assessing the impact of climate change on landslide hazards, 371-377.

COMSOL Multiphysics. version 5.4, COMSOL Inc., Sweden, 2018.

Crozier, M.J., 2010. Deciphering the effect of climate change on landslide activity: A review. Geomorphology 124(3-4), 260-267.

Cundall, P.A., Strack, O.D.L., 1979. A discrete numerical model for granular assemblies. Géotechnique. 29(1), 47-65.

Cuomo, S., Della Sala, M., 2013. Rainfall-induced infiltration, runoff and failure in steep unsaturated shallow soil deposits. Engineering Geology. 162, 118-127.

Dahal, R.K., Hasegawa, S., Yamanaka, M., Nonomura, A., 2008. Typhoon Rainfall and Landsliding in the Pacific Ocean Side of Japan, Proceedings of the Eighteenth (2008) International Offshore and Polar Engineering Conference Vancouver, BC, Canada, 6-11.

Dhakal, A.S., Sidle, R.C., 2004. Distributed simulations of landslides for different rainfall conditions. Hydrological Processes 18(4), 757-776.

Di Giammarco, P., Todini, E., Lamberti, P., 1996. A conservative finite element approach to overland flow: the control volume finite element formulation. Journal of Hydrology. 175, 267-291.

Dijkstra, T.A., Dixon, N., 2010. Climate change and slope stability in the UK: challenges and approaches. Quarterly Journal of Engineering Geology and Hydrogeology 43(4), 371-385.

Endo, A., 1986. A question of snow density and maximum snow depth. Journal of Japan Association for Snow Engineering. 1986(2), 23-30 (in Japanese).

Farshidfar, N., Nayeri, A., 2015. Slope Stability Analysis by Shear Strength Reduction Method. Journal of Civil Engineering and Urbanism. 5(1), 35-37.

Fern, E.J., 2019. Modelling tunnel-induced deformations with the material point method. Computers and Geotechnics. 111, 202-208.

Fernández-Pato, J., Caviedes-Voullième, D., Garcia-Navarro, P., 2016. Rainfall/runoff simulation with 2D full shallow water equations: Sensitivity analysis and calibration of infiltration parameters. Journal of Hydrology. 536, 496-513.

Fredlund, D.G., 1979. Appropriate concepts and technology for unsaturated soils, Second Canadian Geotechnical Colloquium, Canadian Geotechnical Journal. 16(1), 121-139.

Fredlund, M.D., Wilson, G.W., Fredlund, D.G., 2002. Use of the grain-size distribution for estimation of the soil-water characteristic curve. Can. Geotech. J. 39(5), 1103-1117.

Fredlund, D.G., Rahardjo, H., Fredlund, M.D., 2012. Unsaturated Soil Mechanics in Engineering Practice. John Wiley & Sons, Inc., Hoboken, NJ.

Frigerio, S., Schenato, L., Bossi, G., Cavalli, M., Mantovani, M., Marcato, G., Pasuto, A., 2014. A web-based platform for automatic and continuous landslide monitoring: The Rotolon (Eastern Italian Alps) case study. Computers & Geosciences. 63, 96-105.

Fujisawa, K., Marcato, G., Nomura, Y., Pasuto, A., 2010. Management of a typhoon-induced landslide in Otomura (Japan). Geomorphology. 124(3-4), 150-156.

Fukutsu, K., Kawamura, S., 2016. Field monitoring of road embankments in snowy cold regions and its evaluation. 56th Annual meeting of Hokkaido Branch Japanese Geotechnical Society. 319-328 (in Japanese).

Furuichi, T., Osanai, N., Hayashi, S., Izumi, N., Kyuka, T., Shiono, Y., Miyazaki, T., Hayakawa, T., Nagano, N., Matsuoka, N., 2018. Disastrous sediment discharge due to typhoon-induced heavy rainfall over fossil periglacial catchments in western Tokachi, Hokkaido, northern Japan. Landslides. 15, 1645-1655.

Gariano, S.L., Guzzetti, F., 2016. Landslides in a changing climate. Earth-Science Reviews 162, 227-252.

GEO-SLOPE International. GeoStudio, Calgary, Alberta, Canada, 2007.

GETFLOWS. Integrated Water Cycle Simulation System. Geosphere Environmental Technology Corp., Japan, 2014.

Glade, T., Crozier, M.J., Smith, P., 2000. Applying probability determination to refine landslide-triggering rainfall thresholds using an empirical “Antecedent Daily Rainfall Model”. Pure Appl. Geophys. 157, 1059-1079.

Glade, T., Nadim, F. 2014. Early warning systems for natural hazards and risks. Natural Hazards. 70, 1669-1671.

Godt, J.W., Baum, R.L., Chleborad, A.F., 2006. Rainfall characteristics for shallow landsliding in Seattle, Washington, USA. Earth Surface Processes and Landforms. 31(1), 97-110.

Gomi, T., Sidle, R.C., Miyata, S., Kosugi, K., Onda, Y., 2008. Dynamic runoff connectivity of overland flow on steep forested hillslopes: Scale effects and runoff transfer. Water Resources Research. 44, W08411.

Gonzalo, M., Mark, W., Frederick, B.P., Kenneth, E.S., Yakov, P., 2017. Scale effects on runoff and soil erosion in rangelands: Observations and estimations with predictors of different availability. CATENA. 151, 161-173.

Green, W. H., Ampt, G.A., 1911. Studies on Soil Physics, Part 1, the Flow of Air and Water through Soils. Journal of Agricultural Science. 4(1), 1-24.

Griffiths, D.V., Huang, J., Fento, G.A., 2010. Comparison of slope reliability methods of analysis. GeoFlorida 2010: Advances in Analysis, Modeling & Design. 1952-1961.

Guzzetti, F., Peruccacci, S., Rossi, M., Stark, C.P., 2007. Rainfall thresholds for the initiation of landslides in central and southern Europe. Meteorology and Atmospheric Physics. 98, 239-267.

He, M., Hogue, T.S., Franz, K.J., Margulis, S.A., Vrugt, J.A., 2011. Characterizing parameter sensitivity and uncertainty for a snow model across hydroclimatic regimes. Adv. Water Resour. 34, 114-127.

Hokkaido Regional Development Bureau., 2013. Report on slope disaster, recovery and survey design. Route No 230 Sapporo general national highway. Sapporo Development and Construction Department, Sapporo (In Japanese).

Hong, Y., Adler, R.F., 2007. Towards an early-warning system for global landslides triggered by rainfall and earthquake. International Journal of Remote Sensing. 28(16), 3713-3719.

Hong, N., Hama, T., Kitajima, T., Aqili, S.W., Huang, X., Wei, Q., Kawagoshi, Y., 2015. Simulation of Groundwater Levels Using Tank Model with Consideration of Mixed Hydrological Structure in Kumamoto City. Journal of Water and Environment Technology. 13(4), 313-324.

Horton, R.E., 1933. The role of infiltration in the hydrological cycle. Eos Trans. AGU. 14, 446-460.

Ikebuchi, S., Takebayashi, S., Tomomura, M., 1986. Snow accumulation, melting and runoff in the warm climate of Japan. Modeling Snowmelt-Induced Processes (Proceedings of the Budapest Symposium, July 1986). IAHS Publ. 155, 175-192.

International River Interface Cooperative (iRIC). version 2.0, iRIC, Japan, 2015.

Intrieri, E., Gigli, G., Mugnai, F., Fanti, R., Casagli, N., 2012. Design and implementation of a landslide early warning system. Engineering Geology. 147, 124-136.

Ishikawa, T., Miura, S., 2011. Influence of freeze-thaw action on deformation-strength characteristics and particle crushability of volcanic coarse-grained soils. Soils and Foundations. 51(5), 785-799.

Ishikawa, T., Tokoro, T., Miura, S., 2015. Geohazard at volcanic soil slope in cold regions and its influencing factors. Japanese Geotech. Soc. Spec. Publ. 1, 1-20.

Ishikawa, T. Tokoro, T., Miura, S., 2016. Influence of freeze-thaw action on hydraulic behavior of unsaturated

volcanic coarse-grained soils. Soils and Foundations. 56(5), 790-804.

Itasca, Fast Lagrangian Analysis of Continua in 3 Dimensions (FLAC3D), USA, 2012.

Iverson, R.M, Reid, M.E., 1992. Gravity-driven groundwater flow and slope failure potential 1. Elastic effective-stress model, Water Resources Research. 28(3): 925-938.

Iwakura, T., Takayoshi, K., Otani, H., Tanimoto, K., Tokioka, S., Watanabe, T., 2010. Study of warning and evacuation standard-setting approach to the sediment-related disasters that occur in the snowmelt season. 59th Annual Meeting of the Society of Erosion Control Research. Paper 229. (In Japanese).

Japan Meteorological Agency (JMA). 2019. Talas Soil Water Index (in Japanese). <http://www.jma.go.jp/jma/en/News/Talas_soil_water_index.html> (Date accessed: March 16th, 2019).

Jiang, N., Pan, W., Luo, B., Yan, L., Xiang, S., 2014. Simultaneous unidirectional and bidirectional chaos-based optical communication using hybrid coupling semiconductor lasers. Science China Information Sciences, 57(1), 1-11.

Jing, X., Chen, Y., Pan, C., Yin, T., Wang, W., Fan, X., 2019. Erosion Failure of a Soil Slope by Heavy Rain: Laboratory Investigation and Modified GA Model of Soil Slope Failure. Int J Environ Res Public Health. 16(6), 1075.

Kawamura, S., Miura, S., 2018. Mechanical behavior of decomposed granite soils in Hokkaido and its evaluation. Japanese Geotechnical Journal. 13(2), 159-170. (in Japanese)

Kazama, S., Izumi, H., Sarukkalige, P.R., Nasu, T., Sawamoto, M., 2008. Estimating snow distribution over a large area and its application for water resources. Hydrol. Process. 22, 2315-2324.

Kean, J.W., McCoy, S.W., Tucker, G.E., Staley, D.M., Coe, J.A., 2013. Runoff-generated debris flows: Observations and modeling of surge initiation, magnitude, and frequency. J. Geophys. Res. Earth Surf. 118, 2190-2207.

Kitamura, A., Kurikami, H., Sakuma, K., Malins, A., Okumura, M., Machida, M., Mori, K., Tada, K., Tawara, Y., Kobayashi, T., Yoshida, T., Tosaka, H., 2016. Redistribution and export of contaminated sediment within eastern Fukushima Prefecture due to typhoon flooding. Earth Surf. Process. Landforms. 41, 1708-1726.

Kobayashi, S., Kon, H., Kohata, Y., Tajika, J., Tanaka, H., Mikita, M., 2014. Rainfall types, geomorphological and soil physical characteristics of slope disasters in Oshima, Hidaka and Rumoi districts, in Hokkaido. 54th Annual meeting of Hokkaido Branch Japanese Geotechnical Society. 54, 143-148.

Kojima, K., 1967. Densification of seasonal snow cover. Proceedings of Physics of Snow and Ice. 1(2), 929-951.

Kollet, S.J., Maxwell, R.M., 2006. Integrated surface–groundwater flow modeling: A free-surface overland flow boundary condition in a parallel groundwater flow model. Advances in Water Resources. 29(7), 945-958.

Kurahashi, T., Yajima, Y., Tsunoda, F., 2017. Investigation and Evaluation Methods of Road Slope Stability

due to Snowmelt. 1-6 (in Japanese).

Kurahashi, T., Ishimaru, S., Ito, Y., 2018. Geological disasters in the last 10 years in Hokkaido. Monthly Report of Civil Engineering Research Institute for Cold Region. No. 784, 57-66 (in Japanese).

Kuramoto, K., Tetsuga, H., Higashi, N., Arakawa, M., Nakayama, H., Furukawa, K., 2001. A study on a method for determining non-linear critical line of slope failures during heavy rainfall based on RBF network. Proceedings of Japan Society of Civil Engineers. 50(672), 117-132 (in Japanese).

Lee, D-H., Lai, M-H., Wu, J-H., Chi, Y-Y., Ko, W-T., Lee, B-L., 2013. Slope management criteria for Alishan Highway based on database of heavy rainfall-induced slope failures. Engineering Geology. 162, 97-107.

Li, S., Zhang, M., Pei, W., Lai, Y., 2018. Experimental and numerical simulations on heat-water-mechanics interaction mechanism in a freezing soil. Applied Thermal Engineering 132, 209-220.

Li, X., Yan, Q., Zhao, S., Luo, Y., Wu, Y., Wang, D., 2020. Investigation of influence of baffles on landslide debris mobility by 3D material point method. Landslides. 1-15.

Liu, C., Sun, Q., Jin, F., Zhou, G.G.D., 2017. A fully coupled hydro-mechanical material point method for saturated dense granular materials. Powder technology. 314: 110-120.

Liu, X., Wang, Y., Li, D.Q., 2019. Investigation of slope failure mode evolution during large deformation in spatially variable soils by random limit equilibrium and material point methods. Computers and Geotechnics. 111, 301-312.

Lu, N., Şener-Kaya, B., Wayllace, A., Godt, J.W., 2012. Analysis of rainfall-induced slope instability using a field of local factor of safety. Water Resources Research. 48, W09524.

Malow F.A., Shimada S., Hazart A., 2017. Event-based Rainfall-runoff Simulations using GETFLOWS for Kourtimalei Catchment in Djibouti. International Journal of Environmental and Rural Development. 8 (1), 169-175.

McCreight, J.L., Small, E.E., 2014. Modeling bulk density and snow water equivalent using daily snow depth observations. The Cryosphere. 8, 521-536.

Meloysund, V., Leira, B., Hoiseth, K.V., Liso, K.R., 2007. Predicting snow density using meteorological data. Meteorological Applications. 14(4), 413-423.

Miyazaki, T., Nakatsugawa, M., Usutani, T., 2017. Risk Evaluation of Landslide Disaster Occurrence Using Quantification of Soil Moisture Considering Snowmelt. J. Japan Soc. Hydrol. and Water Resour. 30(2), 89-101.

Mizukami, N., Perica, S., 2008. Spatiotemporal Characteristics of Snowpack Density in the Mountainous Regions of the Western United States, Journal of Hydrometeorology. 9, 1416-1426.

Morgenstern, N.R., Price V.E., 1965. The analysis of the stability of general slip surfaces. Géotechnique. 15(1), 79-93.

Mori, K., Tada, K., Tawara, Y., Ohno, K., Asami, M., Kosaka, K., Tosaka, H., 2015. Integrated watershed modeling for simulation of spatiotemporal redistribution of post-fallout radionuclides: Application in

radiocesium fate and transport processes derived from the Fukushima accidents. Environmental Modelling & Software. 72, 126-146.

Motoya, K., Kawashima, K., Matsumoto, T., Iyobe, T., 2017. Analysis of average snowpack densities around Akita pref., estimated from the routinely observed snow depth data and the snow water estimation model. Snow and Life in Tohoku Region. 32, 9-14 (in Japanese).

Murillo, J., García-Navarro, P., Burguete, J., Brufau, P., 2007. The influence of source terms on stability, accuracy and conservation in two-dimensional shallow flow simulation using triangular finite volumes. Int. J. Numer. Methods Fluids. 54, 543-590.

Nakatsugawa, M., Usutani, T., Miyazaki, T., 2015. Risk assessment of sediment disaster based on watershed-wide hydrologic processes. E-proceeding of the 36th IAHR World Congress. 1-9.

Okada, K., 2001. Soil Water Index. Meteorological Society of Japan. 48(5), 59-66 (in Japanese).

Ortuño, M., Guinau, M., Calvet, J., Furdada, G., Bordonau, J., Ruiz, A., Camafort, M., 2017. Potential of airborne LiDAR data analysis to detect subtle landforms of slope failure: Portainé, Central Pyrenees. Geomorphology 295, 364-382.

Osanai, N., Shimizu, T., Kuramoto, K., Kojima, S., Noro, T., 2010. Japanese early-warning for debris flows and slope failures using rainfall indices with Radial Basis Function Network. Landslides. 7, 325-338.

Pan, C., Ma, L., Wainwright, J., Shangguan, Z., 2016. Overland flow resistances on varying slope gradients and partitioning on grassed slopes under simulated rainfall. Water Resources Research. 52, 2490-2512.

Pasculli, A., Calista, M., Sciarra, N., 2018. Variability of local stress states resulting from the application of Monte Carlo and finite difference methods to the stability study of a selected slope. Engineering Geology. 245, 370-389.

Piciullo, L., 2016. Performance analysis of landslide early warning systems at regional scale. Ph.D. Thesis, UNISA, Salerno, Italy, 186 pp.

Rahardjo, H., Lee, T.T., Leong, E.C., Rezaur, R.B., 2005. Response of a residual soil slope to rainfall. Canadian Geotechnical Journal. 42(2), 340-351.

Rahardjo, H., Ong, T.H., Rezaur, R.B., Leong, E.C., 2007. Factors Controlling Instability of Homogeneous Soil Slopes under Rainfall. Journal of Geotechnical and Geoenvironmental Engineering. 1532-1543.

Regmi, R.K., Nakagawa, H., Kawaike, K., Baba, Y., Zhang, H., 2011. Experimental and Numerical Study of Rainfall Induced Slope Failure. Annuals of Disas. Prev. Res. Inst., Kyoto Univ., 54 B, 549-563.

Rengers, F.K., McGuire, L.A., Kean, J.W., Staley, D.M., Hobley, D.E.J., 2016. Model simulations of flood and debris flow timing in steep catchments after wildfire. Water Resources Research. 52(8), 6041-6061.

Richards, L.A., 1931. Capillary conduction of liquids through porous mediums. Physics. 1(5), 318-333.

Saito, H., Nakayama, D., Matsuyama, H., 2010. Two Types of Rainfall Conditions Associated with Shallow Landslide Initiation. SOLA. 6, 57-60.

Sato, A., Hayashi, T., Hayashi, H., Yamaki, M., 2017. On the geotechnical properties of decomposed granite

soil in Hokkaido. 57th Annual meeting of Hokkaido Branch Japanese Geotechnical Society. 145-148 (in Japanese).

Sciarra, N., Calista, M., Miccadei, E., Pasculli, A., Piacentini, T., Sciarra, M., 2017. Morphometric analysis, multitemporal geomorphological investigation and numerical modelling of the Montebello sul Sangro Large Landslide (Abruzzo-Central Italy). Italian Journal of Engineering Geology and Environment. 1(1), 117-133.

Shi, G.H. Discontinuous Deformation Analysis A New Numerical Model for the Static and Dynamics of Block Systems. PhD Dissertation, Dept. of Civil Engineering, 1989.

Shinme, R., Yamashita, S., 2008. Hydrologic measurement using snow cover weight meter in winter. Proceedings of Hydraulic Engineering. 52. 493-498.

Shirakawa, T., Ogura, M., Ozeki, T., Takahashi, S., 2014. Report of snow survey in the central and east region of Hokkaido, 2014. Annual Report on Snow and Ice Studies in Hokkaido. 33, 19-22 (in Japanese).

Shirakawa, T., 2016. Characteristics of spatial distribution of snow water equivalent based on the recent snow surveys, central and eastern Hokkaido. Annual Report on Snow and Ice Studies in Hokkaido. 35, 39-42 (in Japanese).

Shirakawa, T., 2017. Report of snow survey of 32 sites in the central and eastern region of Hokkaido, 2017. Annual Report on Snow and Ice Studies in Hokkaido. 36, 117-120 (in Japanese).

Shou, K.J., Yang, C.M., 2015. Predictive analysis of landslide susceptibility under climate change conditions-A study on the Chingshui River Watershed of Taiwan. Engineering Geology 192, 46-62.

Siva Subramanian, S., Ishikawa, T., Tokoro, T., 2017. Stability assessment approach for soil slopes in seasonal cold regions. Eng. Geol. 221, 154-169.

Siva Subramanian, S., Ishikawa, T., Tokoro, T., 2018. An early warning criterion for the prediction of snowmelt induced soil slope failures in seasonal cold regions. Soils and Foundations. 58(3), 582-601.

Soga, K., Alonso, E., Yerro, A., Kumar, K., Bandara, S., 2016. Trends in large-deformation analysis of landslide mass movements with particular emphasis on the material point method. Géotechnique. 66 (3), 248-273.

SoilVision, Version, 4.23. SoilVision Systems Ltd. Saskatoon, Saskatchewan, Canada, 2018.

Stefano, L.G. Fausto, G., 2016. Landslides in a changing climate. Earth-Science Reviews. 162, 227-252.

Sturm, M., Taras, B., Liston, G.E., Derksen, C., Jonas, T., Lea, J., 2010. Estimating snow water equivalent using snow depth data and climate classes. Journal of Hydrometeorology. 11, 1380-1394.

Sugawara, M., Ozaki, E., Watanabe, I., Katsuyama, Y., 1974. Tank model and its application to Bird Creek, Wollombi Brook, Bikin River, Kitsu River, Sanaga River, and Nam Mune. Research Note of the National Research Center for Disaster Prevention 11, Tsukuba, Japan, 1-64.

Sulsky, D., Chen, Z., Schreyer, H.L., 1994. A particle method for history-dependent materials. Computer methods in applied mechanics and engineering. 118(1-2), 179-196.

Sun, Y., Yang, J., Song, E., 2015. Runout analysis of landslides using material point method. Iop Conference Series: Earth and Environmental Science. IOP Publishing. 26(1), 012014.

Tan, J., Song, H., Zhang, H., Zhu, Q., Xing, Y., and Zhang, J., 2018. Numerical Investigation on Infiltration and Runoff in Unsaturated Soils with Unsteady Rainfall Intensity. Water 10(7), 914.

Tian, D., Liu, D., 2011. A new integrated surface and subsurface flows model and its verification. Applied Mathematical Modelling. 35(7), 3574-3586.

Ting, J.M., Martin, R.T., Ladd, C.C., 1983. Mechanisms of strength for frozen sand. ASCE J. Geotech. Eng. 109 (10), 1286-1302.

Tomomura, M., Fukushima, Y., Suzuki, M., Kubota, J., Ohta, T., 1982. Distribution of water equivalent of snow cover by altitude in the northwestern mountains of Lake Biwa. Bulletin of The Kyoto University Forests. 54, 106-120 (in Japanese).

van Asch, T.W.J., Yu, B., Hu, W., 2018. The Development of a 1-D Integrated Hydro-Mechanical Model Based on Flume Tests to Unravel Different Hydrological Triggering Processes of Debris Flows. Water, 10(7), 950.

van Genuchten, M.Th., 1980. A closed-form equation for predicting the hydraulic conductivity of unsaturated soils. Soil Science Society of America Journal. 44(5), 892-898.

Wang, B., Vardon, P.J., Hicks, M.A., Chen, Z., 2016. Development of an implicit material point method for geotechnical applications. Computers and Geotechnics. 71, 159-167.

Wang, G., Sassa, K., 2003. Pore-pressure generation and movement of rainfall-induced landslides: effects of grain size and fine-particle content. Engineering Geology. 69(1-2), 109-125.

Wei, Z., Shang, Y., Zhao, Y., Pan, P., Jiang, Y., 2017. Rainfall threshold for initiation of channelized debris flows in a small catchment based on in-site measurement. Engineering Geology. 217, 23-34.

Weill, S., Mouche, E., Patin, J., 2009. A generalized Richards equation for surface/subsurface flow modelling. Journal of Hydrology. 366, 9-20.

Woo, S.I., Rodrigo, S., 2018. Simulation of penetration of a foundation element in Tresca soil using the generalized interpolation material point method (GIMP). Computers and Geotechnics. 94, 106-117.

Wu, S., Chen, L., Wang, N., Yu, M., Assouline, S., 2018. Modeling rainfall-runoff and soil erosion processes on hillslopes with complex rill network planform. Water Resources Research. 54, 10,117-10,133.

Yajima, Y., Kurahashi, T., 2015. The factor of road slope disasters in Hokkaido during snowmelt period. Proceedings of Research Meeting of Japan Society of Engineering Geology. 2015, 67-68 (in Japanese).

Yamada, T.J., Farukh, M.A., Fukushima, T., Inatsu, M., Sato, T., Pokhrel, Y.N., Oki, T., 2014. Extreme precipitation intensity in future climates associated with the Clausius-Clapeyron-like relationship. Hydrological Research Letters 8(4),108-113.

Yang, Y.S., Yeh, H.F., 2019. Evaluate the Probability of Failure in Rainfall-Induced Landslides Using a Fuzzy Point Estimate Method. Geofluids 2019, 1-15.

Yin Y.P., Wang H.D., Gao Y.L., Li X.C., 2010. Real-time monitoring and early warning of landslides at relocated Wushan Town, the Three Gorges Reservoir, China. Landslides. 7, 339-349.

Yugui, Y., Feng, G., Yuanming, L., Hongmei, C., 2016. Experimental and theoretical investigations on the mechanical behavior of frozen silt. Cold Regions Science and Technology 130, 59-65.

Zeng, Y.H., Guymer, I., Spence, K.J., Huai, W.X., 2010. Application of analytical solutions in trapezoidal compound channel flow. River Research and Applications. 28 (1), 53-61.

Zhang, J., Huang, H. W., Zhang, L. M., Zhu, H. H., Shi, B., 2014. Probabilistic prediction of rainfall-induced slope failure using a mechanics-based model. Engineering Geology. 168, 129-140.

Zhang, R., Sun, Y., Song, E. 2019. Simulation of dynamic compaction and analysis of its efficiency with the material point method. Computers and Geotechnics. 116, 103218.

Zhao, J., Shan, T., 2013. Coupled CFD–DEM simulation of fluid–particle interaction in geomechanics. Powder technology. 239, 248-258.

Zhao, S., Zhao, J., 2019. A poly-superellipsoid-based approach on particle morphology for DEM modeling of granular media. International Journal for Numerical and Analytical Methods in Geomechanics. 43(13), 2147-2169.

Zhu, Y.L., Ishikawa, T., 2018. Effects of Climate Change on Slope Failure in Snowy Cold Regions. Proceedings of the 61st Symposium of Japanese Geotechnical Society. No. 6-5.1-6.

Zhu, Y.L., Ishikawa, T., Subramanian, S.S., Luo, B., 2020. Simultaneous analysis of slope instabilities on a small catchment-scale using coupled surface and subsurface flows. Engineering Geology, 105750.

LIST OF NOTATIONS

Description	Symbol
Advection term in the *x* direction	D_x
Advection term in the *y* direction	D_y
Amount of hourly snowmelt water	SM
Angle of internal friction associated with the net normal stress state variable	ϕ^b
Area of the basin	A
Average air temperature	T_a
Average suction head at the wetting front	Ψ
Coefficients of permeability from the bottom hole of each tank	β_1, β_2, and β_3
Critical erosional velocity	V_c
Cumulative infiltration	F
Day of year	DOY
Degree-hour factor	K
Degree of saturation of the water phase	S_w
Densification parameters for depth	k_1
Densification parameters for DOY	k_2
Density of liquid water	ρ_w
Density of q phase	ρ_q
Difference between θ_s and θ_i	$\Delta\theta$
Dimensionless eddy viscosity	λ
Dry density	ρ_s
Eddy viscosity coefficient	v_t
Effective cohesion	c'
Effective degree of saturation	S_e
Effective internal friction angle	ϕ'
Effective normal stress on failure plane	σ'
Effective stress parameter	χ
Elevation	z

Flow velocity	V
Fluid mass flux of q phase	M_q
Fluid phase	q
Fluid saturation of q phase	S_q
Friction slope in the x direction	S_{fx}
Friction slope in the y direction	S_{fy}
Frictional velocity	U^*
Frozen thermal conductivity of saturated soil	λ_f
Frozen volumetric heat capacity	ζ_f
Gradient of water surface	S
Gravitational acceleration	g
height of each outlet	L_{11}, L_{12}, L_2, and L_3
Height of grid	H_g
Hourly change of snow water equivalent	ΔSWE
Infiltration capacity	f_p
Infiltration/exfiltration rate	I
Infiltration rate from the upper tank to the lower tank	I_1, I_2, and I_3
Initial snow density	ρ_0
Initial volumetric water content	θ_i
Intercept of the extended M-C failure envelope with the shear stress axis at a specific matric suction	c_f'
Local factor of safety	F_{LFS}
Manning's roughness coefficient	n_m
Mass density	$\rho(\theta)$
Matric suction	σ^s
Maximum snow density	ρ_{max}
Maximum principal stress for the unsaturated soil	σ_1'
Maximum principal stress for the saturated soil	σ_1
Median diameter of the sediment material	D_{50}
Minimum principal stress for the unsaturated soil	σ_3'

Minimum principal stress for the saturated soil	σ_3
Normal density	$f(x)$
Outflow coefficient for each outlet	α_{11}, α_{12}, α_2, and α_3
Outflow rate of each outlet	q_{11}, q_{12}, q_2, and q_3
Poisson's ratio	v
Porosity	φ
Pore air pressure	u_a
Pore water pressure	u_w
Potential of q phase	Ψ_q
Precipitation	P
Pressure head	H_p
Rainfall intensity	R
Relative hydraulic conductivity	k_r
Relative hydraulic conductivity of q phase	$k_{r,q}$
Residual degree of saturation	S_r
Residual volumetric water content	θ_r
Saturated hydraulic conductivity	k_s
Saturated volumetric water content	θ_s
Shear strength	τ_f
Sink and source of water	Q_w
Snow correction factor	SCF
Snow density	ρ_n
Snow depth	h_s
Snowfall	SF
Snow fraction	f_s
Snow water equivalent	SWE
Soil Water Index	SWI
Specific moisture capacity	C_m
Specific storage coefficient	S_c
Stress tensor	$\boldsymbol{\sigma}$

Time	t
Total of outflow rate of the basin	Q
Unfrozen thermal conductivity of saturated soil	λ_u
Unfrozen volumetric heat capacity	ζ_u
van Genuchten parameter	α
van Genuchten parameter	m
van Genuchten parameter	n
Vector of acceleration	$\boldsymbol{a}$
Vector of body forces	$\boldsymbol{b}$
Vector of velocity	$\boldsymbol{v}$
Volumetric flux of the fluid production and extinction of q phase	Q_q
Volumetric flux of sink and source of q phase	q_q
Volumetric water content	θ
Water depth	h
Water storage depth in each layer	H_1, H_2, and H_3
Water surface elevation	H
Water velocity in the x direction	u
Water velocity in the y direction	v
Wind velocity	v_w
Young's modulus	E